Modeling, simulation, and optimization of miniature tribo-electret kinetic energy harvesters

Hanlu Zhang

université PARIS-SACLAY

NN T:2019SACLC100

CentraleSupélec

Modeling, simulation, and optimization of miniature tribo-electret kinetic energy harvesters

Thèse de doctorat de l'Université Paris-Saclay
préparée à CentraleSupélec

École doctorale n°579 Sciences mécaniques et énergétiques, matériaux et géosciences (SMEMAG)
Spécialité de doctorat: Science des Matériaux

Thèse présentée et soutenue à Gif-sur-Yvette, le 20 décembre 2019, par

Hanlu Zhang

Composition du Jury:

Olivier DOARÉ Professeur, ENSTA-Paristech	Président
Alain SYLVESTRE Professeur, G2ELAB, Université Grenoble Alpes	Rapporteur
Philippe BASSET Professeur, Université Paris Est / ESIEE Paris	Rapporteur
Yamin LEPRINCE-WANG Professeur, Université Paris-Est Marne-la-Vallée	Examinateur
Delong HE Ingénieur de Recherche, MSSMAT, CentraleSupélec	Co-encadrant
Jinbo BAI Directeur de Recherche, MSSMAT, CentraleSupélec	Directeur de thèse
Noëlle GOGNEAU Chargée de Recherche, C2N, Université Paris-Saclay	Invitée
Philippe MOLINIÉ Professeur, GeePs, CentraleSupélec	Invité, Co-encadrant

Thèse de doctorat

This page is intentionally left blank.

Modeling, simulation, and optimization of miniature tribo-electret kinetic energy harvesters

by

Hanlu Zhang

Laboratoire de Méchanique des Sols, Structures et Matériaux

A dissertation submitted in partial satisfaction of the requirements for the degree Doctor of Philosophy in Materials Science

in CentraleSupélec, Université Paris-Saclay

2019

This page is intentionally left blank.

ÉCOLE DOCTORALE
Sciences mécaniques et énergétiques, matériaux et géosciences (SMEMAG)

Titre : Modélisation, simulation et optimisation de récupérateurs d'énergie cinétique miniatures avec triboélectrets

Mots clés : Récupérateurs d'énergie cinétique, Tribo-électrets, Modélisation, Simulation, Optimisation, Modification du potentiel de surface

Résumé : La récupération d'énergie ambiante représente une solution durable et complémentaire, par rapport aux batteries, en termes d'alimenter certains produits électroniques grand public, des réseaux de capteurs distribués sans fil, des dispositifs portables ou implantables, des systèmes "Internet of Things" avec beaucoup de nœuds, etc.. Les mouvements humains et les vibrations mécaniques sont des sources d'énergie les plus disponibles à cet effet. Les dispositifs collectant de l'énergie cinétique à petite échelle sont appelés récupérateurs d'énergie cinétique (RECs). Les RECs avec électrets (E-RECs) sont RECs électrostatiques qui utilisent des électrets (diélectriques avec charges quasi permanentes) comme source de tension de polarisation, et qui peuvent générer de l'électricité grâce à l'effet d'induction électrostatique lorsque la capacitance des E-RECs varie du fait des mouvements/vibrations. L'objectif de cette thèse est d'étudier les caractéristiques de sortie transitoires des E-RECs à la fois par des simulations théoriques et par des mesures expérimentales, et d'optimiser l'efficacité et la puissance de sortie des E-RECs par charge triboélectrique ainsi que d'autres méthodes adaptées à leurs caractéristiques de sortie, qui sont essentielles pour améliorer la performance des E-RECs.

Tout d'abord, les caractéristiques de sortie à amplitude variable d'un E-REC en mode contact-séparation (CS) dans des cycles de travail transitoires sont examinées via les résultats de la simulation basés sur un modèle de circuit équivalent détaillé. Ces caractéristiques de sortie à amplitude variable sont attribuées au décalage du cycle de transfert de charge par rapport au cycle de mouvement d'excitation. Les influences de la condition initiale et de la résistance de charge sur la variation des pics de tension de sortie d'un tribo-électret REC (TE-REC) en mode CS réalisé avec un film électret en polytétrafluoroéthylène (PTFE) one été étudiées en détail et vérifiées à la fois par simulations et expériences.

Deuxièmement, une méthode d'optimisation du temps de contact est utilisée pour améliorer la puissance de sortie et l'efficacité du TE-REC en mode CS avec une résistance de charge de 100 MΩ. L'énergie convertie théorique maximale par cycle de travail du TE-REC est analysée. Nous avons aussi étudié les influences de plusieurs facteurs défavorables qui généralement réduiraient la conversion d'énergie par cycle de travail du TE-REC. L'optimisation de l'intervalle d'air maximal et la méthode tribo-charge sont également utilisées pour améliorer la puissance moyenne sortie du TE- REC avec une surface de 4 cm × 4 cm, de ~ 150 μW à ~ 503 μW.

Enfin, une méthode innovante et facile a été développée pour charger le film polymère électret en éthylène propylène fluoré (FEP) par pelage de ruban adhésif, sans utiliser de source de haute tension électrique. La distribution du potentiel de la surface du film de FEP est fortement modifiée après plusieurs pelages au ruban adhésif. Par conséquence, la tension et le courant de sortie des TE-REC fabriqués avec le film FEP traités sont beaucoup améliorés. Pour un TE-REC flexible d'une surface de 64 cm2 soufflé par du vent, une amélioration évidente d'environ 692% de la puissance de sortie, correspondant 2,5 μW à environ 19,8 μW, a été obtenue par cette méthode.

Université Paris-Saclay
Espace Technologique / Immeuble Discovery
Route de l'Orme aux Merisiers RD 128 / 91190 Saint-Aubin, France

Title : Modeling, simulation, and optimization of miniature tribo-electret kinetic energy harvesters

Keywords : Kinetic energy harvesters, Tribo-electrets, Modeling, Simulation, Optimization, Surface potential modification

Abstract : Harvesting energy from the ambient environment is a good sustainable and complementary power supply solution in some consumer electronics, distributed wireless sensor networks, wearable or implantable devices, "Internet of Things" systems with lots of nodes, etc. in comparison with batteries. The ubiquitous kinetic energy in various motions and vibrations is one of the most available energy sources for such a purpose. The electret kinetic energy harvesters (E-KEHs) is one type of electrostatic kinetic energy harvesters using electrets (dielectrics with quasi-permanent charges) as the biasing voltage source, which can generate electricity based on the electrostatic induction effect when the capacitance of the E-KEHs is changed by the motions/vibrations. This thesis aims to investigate the transitory output characteristics of E-KEHs by both theoretical simulations and experimental measurements and to optimize the efficiency and output power of E-KEHs by tribo-charging and other methods adapted to their output characteristics, which are significant to improving the performance of E-KEHs.

Firstly, the amplitude-variable output characteristics of a contact-separation (CS) mode E-KEH in transitory working cycles are investigated via the simulation results based on a detailed equivalent circuit model. These amplitude-variable output characteristics are attributed to the lag of the charge-transfer cycle behind the excitation motion cycle. The influences of both the initial condition and the load resistance on the variation in the output voltage peaks of a tribo-electret KEH (TE-KEH) are studied in detail and verified by both simulated and experimental data of a CS mode TE-KEH made with polytetrafluoroethylene (PTFE) electret film.

Secondly, based on the analysis of the amplitude-variable output characteristics, a contact time optimization method is used to improve the output power and efficiency of the CS mode TE-KEH with a large load resistance of 100 MΩ. The theoretical maximum output energy per working cycle of the TE-KEH is analyzed. Several usually unfavorable factors that would reduce the practical output energy per working cycle of the TE-KEH are discussed. The maximum air gap optimization and the tribo-charging methods are also used together to further improve the average output power of the 4 cm × 4 cm sized TE-KEH from ~150 μW to ~503 μW.

At last, an innovative and facile tape-peeling tribo-charging method is developed to charge the fluorinated ethylene propylene (FEP) polymer film to make electrets without using any high voltage source. The surface potential distribution of the FEP film is apparently changed after several tape-peeling tribo-charging treatments. Consequently, the output voltage and current of TE-KEHs made with the FEP film are greatly improved. For a 64 cm2 sized flexible TE-KEH to harvest kinetic energy from wind, an apparent ~692% improvement in the output power from ~2.5 μW to ~19.8 μW was obtained by the tape-peeling charging method.

Université Paris-Saclay
Espace Technologique / Immeuble Discovery
Route de l'Orme aux Merisiers RD 128 / 91190 Saint-Aubin, France

Acknowledgements

First, I would like to express my sincere gratitude to my supervisor Prof. Jinbo Bai for giving me the opportunity to do this research and for his guidance always with patience and encouragement during my doctoral study. Special gratitude is also given to my co-supervisors Dr. Delong He and Prof. Philippe Molinié. They gave me many inspiring suggestions and help in experimental implementations. Every discussion with them is helpful to me. It would be impossible to finish this thesis without their guidance and supports.

Then I would thank all the jury members of my thesis defense: the chairman Prof. Olivier Doaré, two reporters Prof. Alain Sylvestre and Prof. Philippe Basset, the examiner Prof. Yamin Leprince-Wang, and the invited member Madame Noëlle Gogneau. All their comments and questions especially those in the reports are instructive in improving the quality of this thesis.

I am grateful to the staffs at the laboratories of MSSMat, SPMS, and LGPM. Special gratitude is extended to Mr. Éric Perrin for his help in setting up the linear motor system, to Nicolas Roubier for his help in repairing the measurement programs of electrometers, to Madame Farida Djebarri for her help in purchasing the surface voltmeter and other experimental materials, to Mr. Gilbert Le Gal for fabricating designed mechanical components, to Madame Pascale Gemeiner for her help in Raman measurements, to Mr. Vincent Butin for his help in FT-IR measurements, to Mr. Xavier Bril and Mr. Paul Haghi-Ashtiani for their help in trial experiments of charging electrets by thermo-charging or cold plasma, and to Madame Fleur Litoust and Mr. Daniel Kervern for their kindly help in many aspects during my stay at MSSMat.

I also owe my sincere gratitude to my colleagues and friends in France: Yu Liu, Yiguo Xu, Minhao Yang, Anne Zhang, Shan Feng, Benhui Fan, Chaohe Hu, Li Gong, Na Cui, Jing Zhang, Yuanyuan He, Yuzhu Wang, Guang Zhu, et al. Their help, encouragement, and companionship gave me a precious period full of joy in France.

Meanwhile, I would also like to express my gratitude to China Scholarship Council (CSC) for the financial support to my study in France.

Finally, I would express my gratitude to my family. They always gave me warm encouragement and support, which often cheered me up when I was down.

Table of content

Abbreviations and Symbols

Abbreviations

AC	Alternative Current
Al	Aluminum
AlN	Aluminum Nitride
Au	Gold
BT	Barium Titanate
CDRG	Coulomb-Damped Resonant Generator
CE	Contact Electrification
CFPG	Coulomb-Force Parametric Generator
CMEO	Cycles for Maximized Energy Output
CS	Contact-Separation
Cu	Copper
DC	Direct Current
DE	Dielectric Elastomer
DOF	Degree of Freedom
EG	Electret Generator
E-KEH	Electret Kinetic Energy Harvester
EM	Electromagnetic
ES	Electrostatic
FEP	Fluorinated Ethylene Propylene
FT-IR	Fourier Transform Infrared Spectroscopy
IoT	Internet of Things
KEH	Kinetic Energy Harvester
KERS	Kinetic Energy Recovery System
MEMS	Micro-Electro-Mechanical System
PDMS	Polydimethylsiloxane
PE	Piezoelectric
PENG	Piezoelectric Nanogenerator
PTFE	Polytetrafluoroethylene
PVDF	Polyvinylidene Fluoride
PZT	Lead Zirconated Titanate

RC	Resistor-Capacitor
SEM	Scanning Electron Microscope
TE	Tribo-electret
TEG	Triboelectric Generator
TENG	Triboelectric Nanogenerator
VDRG	Velocity-Damped Resonant Generator
WSN	Wireless Sensor Network
ZnO	Zinc Oxide

Symbols

a	acceleration (m/s^2)
$AvgP$	average output power (W)
C	capacitance (F)
d_0	effective dielectric thickness (m)
d_{of}	effective dielectric thickness of the electret film (m)
$\boldsymbol{d}$	**the piezoelectric strain coefficient tensor (pC/N)**
D	damping coefficient (Ns/m)
$\boldsymbol{D}$	**electric displacement (C/m^2)**
$\boldsymbol{\delta}$	**strain tensor**
E	electromotive force (V)
$\boldsymbol{E}$	**electric field (**V/m**)**
ε_0	vacuum permittivity ($\sim 8.85\times10^{-12}$ F/m)
ε_r	dielectric constant
g	gravitational acceleration (m/s^2)
I	current (A)
φ	magnetic flux (Wb)
k	spring constant (N/m)
m	mass (kg)
σ	effective surface charge density (C/m^2)
$\boldsymbol{\sigma}$	**stress tensor (MPa)**
P	output power (W)
Q	charge (C)
R	resistance (Ω)

S	area (m^2)
t	time (s)
T	period (s)
V	voltage (V)
v	motion velocity (m/s)
W	energy (J)
Ψ	total magnetic flux linkage (Wb)
ζ	damping ratio

This page is intentionally left blank.

Chapter 1 General background and introduction

1.1 Background

Harvesting energy from the ambient environment is a good choice to prolong the life time or even become the power supply in consumer electronics, distributed wireless sensor networks (WSN), wearable or implantable devices, Internet of Things (IoT) systems with lots of nodes, etc. [1-3]. Especially with the development of electronic technology, electronic devices have a general trend of miniaturization with lower power consumption [4], making it possible to build autonomous self-powered systems powered by energy harvesters, reducing the maintenance and environmental problems caused by drained batteries. **Figure 1-1 s**hows the comparison of advantages and disadvantages in using batteries and energy harvesters (EHs) in such systems.

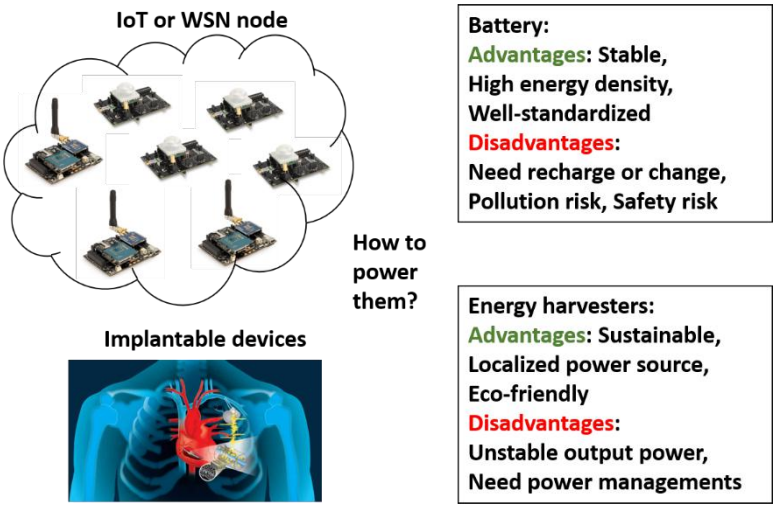

Figure 1-1 Comparison between the battery and energy harvesters in powering IoT or WSN node and implantable devices.

Four main ambient energy sources exist in our environment: radiant energy (light, radio-frequency radiations), mechanical energy (vibrations, movements, and deformations), thermal energy (temperature gradients or variations), and chemical energy (chemistry, biochemistry). Each of them has a different power density range in different environments. The type of energy source to be used should be chosen according to the local environment and the power consumption of the load circuit [5].

Outdoor sunlight is usually considered to be the most powerful ambient energy source as shown in **Table 1-1**.

Table 1-1 Estimated power densities of several energy sources [2, 6].

Energy sources	Estimated Power density (μW/cm^3)	Harvesting method
Solar (outdoors)	150~15000	Photovoltaic
Solar (indoors)	6~100	
Human walking	~330	Kinetic energy harvesters (Electromagnetic, Piezoelectric, Electrostatic)
Vibrations (human motion)	~4	
Vibrations (machine)	~800	
Daily temperature variation	~10	Pyroelectric
10 ℃ temperature gradient	~15	Thermoelectric

However, for some situations without enough light but with abundant mechanical energy sources, kinetic energy harvesters (KEHs) could be suitable for extending the lifetime of power source [2] or building self-powered systems. Different from the kinetic energy recovery system (KERS) which harvests kinetic energy of a vehicle under braking [7], KEHs mainly convert small-scale kinetic energy from motions and vibrations into electricity with the power of microwatt to a milliwatt. And the dimension of KEHs in any direction is usually below 10 cm, that's why they are usually described as "miniature". In this thesis, KEHs are defaulted to be miniature without special statement. Three common types of KEHs, i.e. the electromagnetic, piezoelectric, and electrostatic, will be introduced in section 1.2.

1.2 Different types of kinetic energy harvesters (KEHs)

1.2.1 Electromagnetic KEHs

Electromagnetic (EM) generators are basically used almost in every power station except the photovoltaic ones. They are based on Faraday's law of induction i.e. "*The electromotive force around a closed conductive path equals the negative of the time rate of change of the magnetic flux enclosed by the path*." [8] as expressed by the equation *(1-1)*, where E is the electromotive force, Ψ is the total magnetic flux linkage enclosed by the conductive path, n is the number of turns of the conductive coil that forms the conductive path, φ is the magnetic flux enclosed by the conductive coil, t is time.

$$E = -\frac{d\Psi}{dt} = -n\frac{d\varphi}{dt} \qquad (1\text{-}1)$$

Electromagnetic KEHs (EM-KEHs) are based on the same fundamentals but with smaller scales. They are made with at least one conductive coil which is relatively movable to at least one magnet, with two typical architectures: magnet in line and magnet across coil [9]. The conductive coil usually has multiple turns to get a considerable electromotive force. And the internal resistance of the electromagnetic KEHs is low due to the conductive nature of the coil. Huge EM generators can output remarkable power at the magnitude up to ~1000 MW [10] by using an intense magnetic field and numerous turns of coils. While for miniature EM-KEHs, the magnetic field and turns of coils are usually constrained by the limitations in the volume, cost, weight, etc., and they are often designed to have a high mechanical quality factor to harvest energy from low-amplitude vibrations, but that leads to a narrow bandwidth of EM-KEHs [11].

To widen the bandwidth of EM-KEHs, Sari et al. [12] designed an arrayed EM-KEH with multiple cantilever-structured coils as shown in **Figure 1-2(a)**, each with a different cantilever length to get different resonant frequencies. The overall frequency response of the output power of this arrayed EM-KEH was effectively broadened as shown in **Figure 1-2(b)**. However, due to the small dimensions of each cantilever, the frequency band located at a high-frequency range of about 3400~4600 Hz which is much larger than common vibrations in the ambient environment (mostly lower than 250 Hz) [2]. Halim et al. [13] designed a cylinder non-resonant EM-KEH with two frequency up-converted small generators using spring at the two ends and an inside free-moving ball to harvest energy from low frequency vibrations, as shown in **Figure 1-2(b)**, with a flat peak-to-peak open-circuit voltage around 2.4 V in the excitation frequency range of 14~25 Hz. Besides these two designs, Zhu et al. proposed a method of tuning the electrical resonant frequency of the EM-KEH with loading different capacitors to the EM-KEH, but with narrow effective tuning ranges [11].

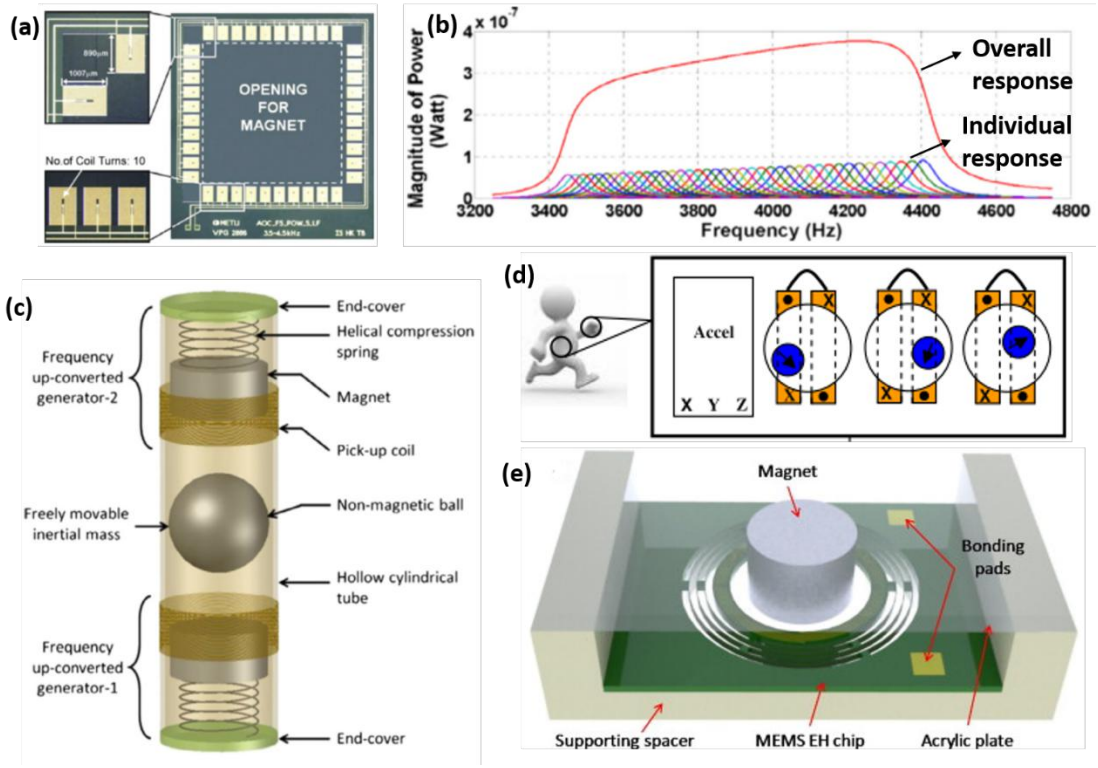

Figure 1-2 Diverse miniature EM-KEHs. (a) An arrayed multiple cantilever EM-KEH with its frequency response shown in (b) [12]. (c) An EM-KEH with the inside free-moving ball for energy harvesting from low-frequency vibrations [13]. (d) A spherical EM-KEH with inside free-rolling magnet ball for harvesting energy from irregular human motions [14]. (e) A resonant EM-KEH with 6 degree-of-freedom for harvesting energy from vibrations of multiple directions [15].

Other special structure designs of EM-KEHs include a spherical structure with an inside free-rolling magnet by Bowers et al. [14], as illustrated in **Figure 1-2(d)**, and using a micro resonant structure with 6 degree-of-freedoms (DOFs) of motions by Liu et al. [15], as shown in **Figure 1-2(e)**, to harvest energy from multi-directional vibrations. It should be noted that the open-circuit voltage and thus the output power of EM-KEHs are usually low due to the constraints in the magnetic field intensity, the turn number of coils, and the working frequency. Moreover, the complicated structure designs and utilization of multiple materials make EM-KEHs not compatible with massive production processes. It is considered that EM generators are irreplaceable in huge power generations, but EM-KEHs are uncompetitive in harvesting small/micro-scale kinetic energy in comparison with other techniques [2].

1.2.2 Piezoelectric KEHs

In crystalline materials with no inversion symmetry, electric potential can be produced under stress, this is called the piezoelectric effect which was first reported by Jacques and Pierre Curie brothers in 1880 [16], and such materials are termed as piezoelectric (PE) materials. The first well-known application of PE materials is on sonar systems where the inverse PE effect (i.e. the generation of stress by applying electric field) of quartz slice was used to produce ultrasounds. PE materials are usually dielectrics with low conductivity, after depositing with conductive electrodes on their polar directions, they can be used to fabricate KEHs to generate electricity from mechanical stress. Two constitutive equations those describe the PE and reverse PE effects are [2]:

$$\boldsymbol{\delta} = \boldsymbol{\sigma}/Y + \boldsymbol{dE} \qquad (1\text{-}2)$$

$$\boldsymbol{D} = \varepsilon\boldsymbol{E} + \boldsymbol{d\sigma} \qquad (1\text{-}3)$$

where $\boldsymbol{\delta}$, $\boldsymbol{\sigma}$, and $\boldsymbol{d}$ are tensors of the strain, the stress, and the PE strain coefficients, respectively; Y is the Young's Modulus of the PE material; $\boldsymbol{E}$ and $\boldsymbol{D}$ are vectors of the electric field and the electrical displacement (charge density), respectively.

Two of the PE strain coefficients, d_{31} and d_{33}, are often used to evaluate the electromechanical coupling intensity of PE materials. Lead zirconated titanate (PZT) and related inorganic materials with the perovskite crystalline structure are typical piezoelectric materials with high d_{33} (400~2500 pC/N) [16, 17], but also with high stiffness [18]. Polyvinylidene fluoride (PVDF) as a piezoelectric polymer has low stiffness but a relative lower d_{33} than piezoelectric ceramics. Nathan S. Shenck and Joseph A. Paradiso [19] designed an energy harvesting shoe using a PZT dimorph under the heel and a flexible PVDF stave under the ball of the foot to scavenge electricity from human walking, as shown in **Figure 1-3(a)**. Liu et al. [20] designed a PZT-based EH with two cantilever structures with different resonant frequencies to broaden the operation frequency range and increases the output voltage and power, as shown in **Figure 1-3(b)**. Wurtzite aluminum nitride (AlN) is another usually used piezoelectric ceramic. Self-powered wireless sensor models based on MEMS AlN piezoelectric EHs had been developed by MicroGen Systems, Inc. [16] as shown in **Figure 1-3(c).**

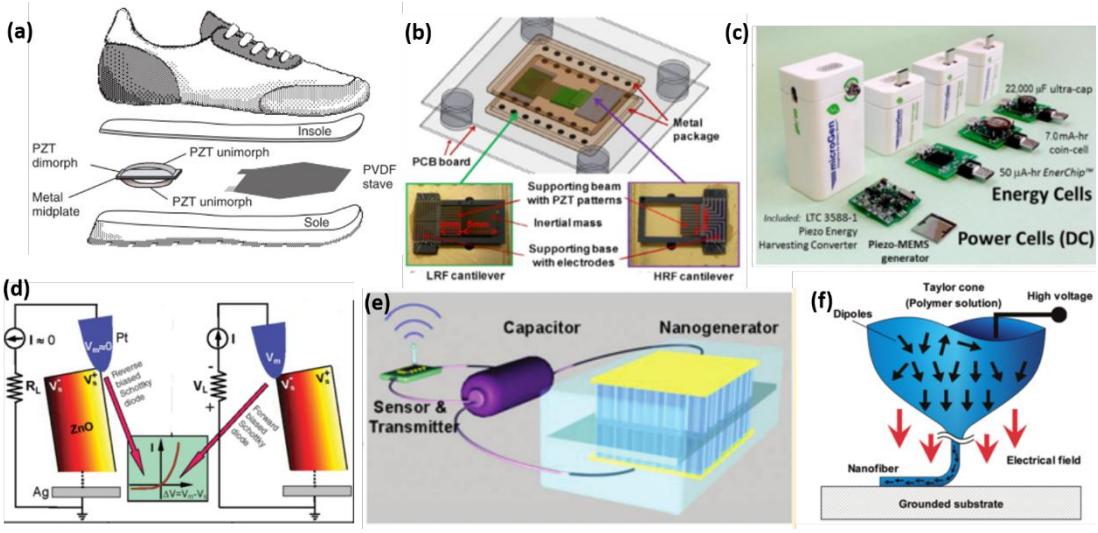

Figure 1-3 Diverse miniature PE-KEHs. (a) A piezoelectric EH mounted in a shoe to harvest energy from human walking [19]. (a) A piezoelectric EH based on two cantilever structures with different resonant frequencies. [20] (c) An AlN-based EH model for self-powered wireless sensors [16]. (d) The piezoelectric effect on a single ZnO nanowire [21]. (e) A self-powered wireless sensor system based on ZnO nanowire arrays [22]. (f) Near-filed electrospinning PVDF nanowires with intrinsic high piezoelectric coefficients [23].

Generally, piezoelectric ceramics and polymers need to be polarized to align their dipole directions in different piezoelectric domains before using. While for a single piezoelectric nanowire, piezoelectricity can present without poling treatment, as illustrated in **Figure 1-3(d)**. Z. L. Wang et al. [21, 24] fabricated piezoelectric nanogenerators (PENGs) based on wurtzite aligned zinc oxide (ZnO) nanowire arrays, they also demonstrated a wireless sensor and transmitter system powered by a ZnO nanowire array PENG [22] as shown in **Figure 1-3(e)**. PVDF nanofibers prepared by a near-field electrospinning method reported by C. Chang et al were also found to have good piezoelectric performance due to the in situ mechanical stretch and electrical poling during the electrospinning process, as shown in **Figure 1-3(f)**.

1.2.3 Electrostatic KEHs

Electrostatic (ES) KEHs mainly refer to KEHs based on variable capacitors which are appropriately pre-charged, and kinetic energy is converted to electricity when the pre-charged capacitors have a decrease in the capacitance C due to the relative movement or deformation of their electrodes or inner dielectrics caused by external motions. There are two basic working modes for ES-KEHs. In the constant charge mode schemed in **Figure 1-4(a)**, the capacitor was firstly charged with a certain amount of charge when C is at the maximum value (C_{max}, **o→a** in the

corresponding QV diagram), then C decreases in the open-circuit condition which means the charge amount keeps constant (**a→b**), followed by the discharge when C get the minimum value (C_{min}, **b→o**) with transferring electricity to load circuit, then C goes back to C_{max} to start the next cycle. And in the constant voltage mode schemed in **Figure 1-4(b)**, the capacitor is firstly pre-charged to a constant voltage value when C is at the maximum value (**o→a**), then discharge occurs with C decreasing and the voltage keeps constant (**a→b**), finally C goes back to the maximum value to start the next cycle.

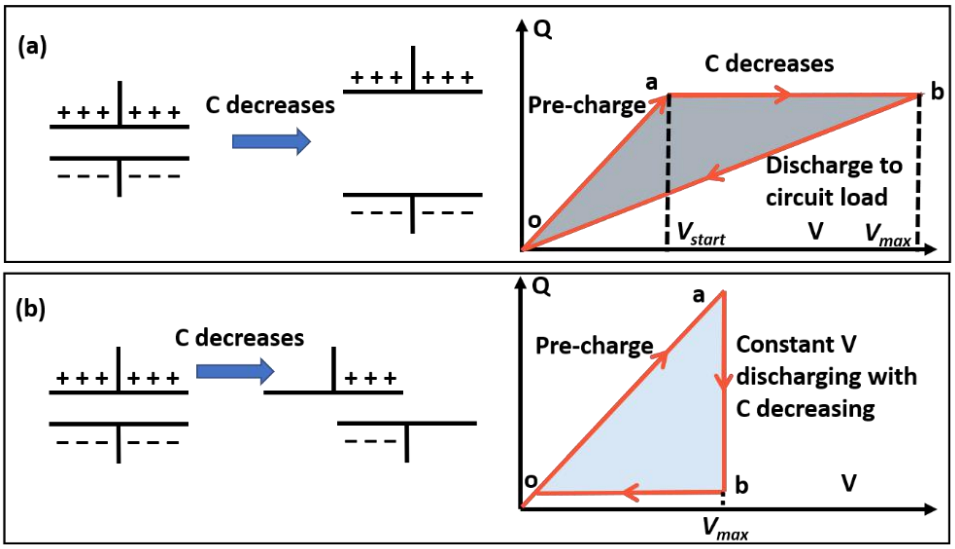

Figure 1-4 Illustrations of (a) the constant charge and (b) the constant voltage working modes of a variable capacitor electrostatic EH with corresponding QV diagrams, reproduced from [25].

For both modes, the ES-KEH output net electric energy that equals the enclosed area of the triangle shape **oab** in one working cycle. For the constant charge mode, it can be calculated by [26]:

$$W_{chrgcons} = \frac{1}{2}(C_{max} - C_{min})V_{start}V_{max} \qquad (1\text{-}4).$$

And for the constant voltage mode, there is [26]:

$$W_{voltcons} = \frac{1}{2}(C_{max} - C_{min})V_{max}^2 \qquad (1\text{-}5).$$

These two modes are two extreme working cycles. In practice, the shape of the QV diagram can be modulated by external conditioning circuits. To implement the constant voltage or charge mode in an ES-KEH, at least two synchronized switches with the switching on-off period same with the variation period of C are necessary

[27]. There are other shapes of the QV cycle of ES-KEHs that can be implemented by simpler conditioning circuits. As illustrated in **Figure 1-5(a)**, besides the triangle QV cycle shapes for the constant-charge (trace OCB) and constant-voltage (trace OAB), other common shapes of QV cycle of ES-KEH includes the rectangle (trace DFBE) which can be realized by a charge pump [28-30] or a Bennet's doubler [30-32] or a Cockcroft–Walton voltage multiplier [33, 34] circuit, and the teardrop shape (dotted line trace) which can be realized by continuous conditioning circuit or ES-KEHs with electret layer [35, 36]. **Figure 1-5(b)** illustrated successive QV cycles from the first triangle shape to a series of trapezoidal shapes, which can be obtained from an ES-KEH with a pre-charged large reservoir capacitor as the voltage source and with an idealized pre-charged charge pump circuit [27].

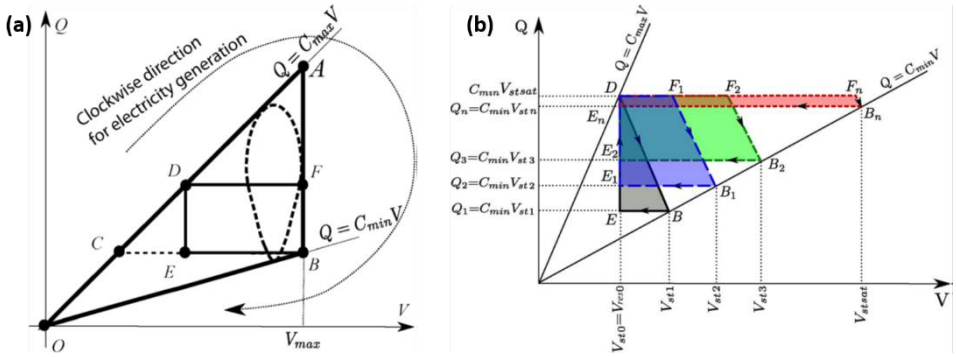

Figure 1-5 (a) Common shapes of the QV cycle of ES-KEHs. (b) Illustration of successive QV cycles from an ES-KEH with an idealized pre-charged charge pump circuit. [27]

During the capacitance variation of the ES-KEHs, kinetic energy is converted to electrostatic energy *via* the Coulomb's force which is more significant than Lorenz's force in micro-scale [25]. In addition, ES-KEHs with variable capacitance structures have good compatibility with MEMS fabrication processes, which is important for batch fabrication with low cost [25, 37]. Therefore, ES-KEHs are more suitable than EM-KEHs to be miniaturized and batch-fabricated to harvest micro-vibration energy. By a simple batch process using only two lithography masks, P. Basset et al. [38] fabricated a micro ES-KEH with an area of about 1 cm^2 as shown in **Figure 1-6(a)**. The micro interdigit variable capacitance structure of another micro ES-KEH with an overall size of 1 cm × 1.5 cm × 200 μm by Bogdan Vysotskyi et al. [39] is presented in **Figure 1-6(a)**.

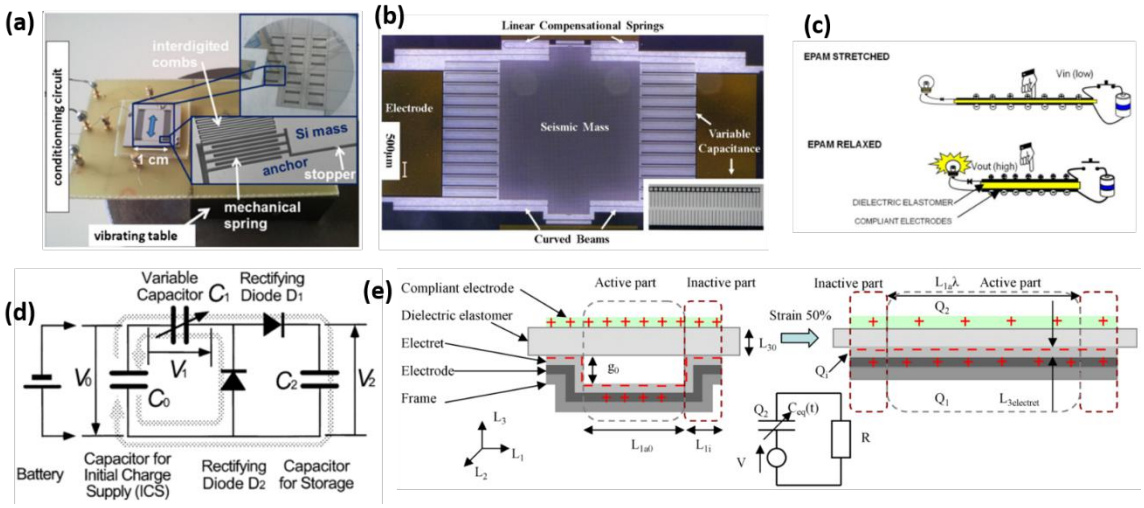

Figure 1-6 (a) A batch-fabricated micro ES-KEH [38]. (b) Photograph of a micro ES-KEH showing the micro comb variable capacitance structure [39]. (c) Scheme of an ES-KEH using dielectric elastomer [40]. (d) A circuit provides an initial charge to the variable capacitor in an ES-KEH [41]. (e) A dielectric elastomer ES-KEH using electret as the biasing voltage source [42].

Besides micro electrostatic KEHs to harvest energy from vibrations, dielectric elastomers (DE) were used to fabricated relative large electrostatic KEHs [40, 43] to harvest energy from pressure-driven deformations as illustrated in **Figure 1-6(c)**. However, for those electrostatic KEHs, at least an external initial charge/voltage supply is required to charge the variable capacitor before harvesting energy, as illustrated in **Figure 1-6(d)**, and a switching or continuous conditioning circuit [27] is usually necessary to control the charge-discharge cycles. Therefore, T. Vu-Cong, T, C. Jean-Mistral, and A. Sylvestre [42, 44, 45] used electrets (quasi-permanently charged dielectrics) to substitute the external charge/voltage source, which greatly simplifies the structure and power management circuits of DE-KEHs. Other electrostatic KEHs using electrets will be further introduced in Chapter 2, section 2.4.

1.2.4 Comparisons among different types of KEHs

Among these three common types of KEHs, S.J. Roundy [2] estimated that the PE-KEHs have the highest practical maximum power density of ~ 17.7 mJ/cm^3, the EM-KEHs and ES-KEHs have the same practical maximum power density of ~4 mJ/cm^3. In practice, there are also other factors (e.g. the dimension, the working frequency, the load circuit) those need to be considered to decide which type of KEHs is more appropriate for specific applications. Several advantages and disadvantages of these three types of KEHs are listed in **Table 1-2.**

Table 1- 2 Comparison of advantages and disadvantages of the three types of KEHs.

Type	Advantages	Disadvantages
Electromagnetic	High efficiency; Large Reliability; Low mechanical damping; Small Resistive impedance	Low output voltage for miniature devices; Heavy magnets; Difficult to batch-fabricate miniature devices
Piezoelectric	High energy density; Moderate output voltage; Easy to scale down by using nanomaterials	Low efficiency; Pulsed output; High capacitive impedance; Need relatively large forces to deform piezoelectric materials;
Electrostatic	High efficiency and open-circuit voltage for miniature devices; Low weight; Compatible with microfabrication	Need pre-charge or biasing voltage; High capacitive impedance; Low output current; Risks of electrostatic adherence and discharge

1.3 Motivations and the outline of this thesis

ES-KEHs using electrets, especially the tribo-charging electrets (tribo-electrets), are the research objects of this thesis. The motivations include understanding the basic working principle of electret-KEHs (E-KEHs) by analytical modeling and numerical simulations, optimizing the output power of tribo-electret KEHs (TE-KEHs) based on the simulation results and experiments, and developing a facile and effective tribo-charging method to charge the electrets.

The general outline of this thesis is as follows. In **Chapter 1**, the general background and brief introductions and comparisons of three common types of KEHs have been presented. In **Chapter 2**, physical fundamentals and charging methods for electrets are briefly introduced, and an introduction to the basic principle, early researches, structure designs, and the physical models of E-KEHs is given. In **Chapter 3**, the analytical solution of a detailed equivalent circuit model for contact-separation (CS) mode E-KEHs is given, then the amplitude-variable output characteristics of a CS mode E-KEH during transitory working cycles with different load resistances and initial conditions are studied, the reason for these characteristics are analyzed based on both simulation and experimental results. In **Chapter 4**, several optimization methods are used to improve the output power of a CS mode TE-KEH,

the maximum theoretical output energy or the TE-KEH is deduced, and several usually unfavorable factors that would reduce the effective output energy per working cycle of TE-KEHs are discussed. In **Chapter 5**, a novel tape-peeling tribo-charging method is used to charge FEP electret films, the output voltage and current of TE-KEHs based on the FEP films are apparently improved by the tribo-charging method, and the prototype of a flexible FEP-film based TE-KEH is demonstrated to harvest energy from wind and gentle human motions. In **Chapter 6**, remarks on simulations and power managements of E-KEHs are given, and perspectives on future work related to this thesis are presented.

This page is intentionally left blank.

Chapter 2 Introduction to electrets and electret kinetic energy harvesters

2.1 Overview

In this chapter, firstly a brief introduction to the physical fundamentals and charging methods for electrets is given in section 2.2, then a more detailed introduction to electric kinetic energy harvesters (E-KEHs) from the basic principle and research history to the different structure designs, driving modes, and theoretical models is presented in section 2.3~2.5.

2.2 Electrets

2.2.1 Physical fundamentals

It is believed that Michael Faraday was the first to outline the basic principles of electrets in 1839 [46], Oliver Heaviside created the word “electret” in 1892 [47], and the systematic research into electrets began in 1919 when a Japanese physicist, Mototaro Eguchi, fabricated an electret by cooling and solidifying molten mixture of Carnauba wax and resin with a little beeswax while applying an electric field of about 10 $kV \cdot cm^{-1}$ to the mixture [48, 49]. In the book *Electret* published in 1987 [46], G. M. Sessler gave a general physical definition of electret as: “An electret is a piece of dielectric material exhibiting a quasi-permanent electrical charge. The term "quasi-permanent" means that the time constants characteristic for the decay of the charge are much longer than the time periods over which studies are performed with the electret.”. The motioned “electrical charge” could be “real” excess mono-charges on the surface or in the bulk of materials, or polarizations (frozen-in aligned dipoles for polar, or space charges for both polar and non-polar dielectrics) in the bulk, or a composition of them [46, 50], as illustrated in **Figure 2- 1**.

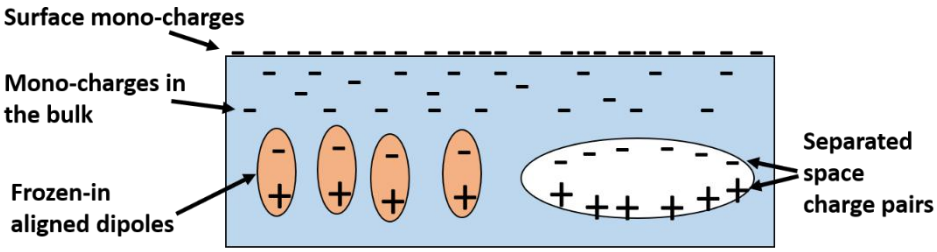

Figure 2- 1 Different types of electrical charges in electrets.

The charge decay time constant in electret materials is usually expected to be as large as possible. The concerned "time periods" for studies in electrets are usually counted in hours, days, months, and even years [50]. Dielectric materials with excellent insulating properties are usually good candidates to make electrets since their extremely low conductivities could lead to a quite large charge decay time constant. For instance, it was estimated that a corona-charged polytetrafluoroethylene (PTFE), which is one of the best insulating polymers with low conductivity of ~10^{-22} $\Omega^{-1}cm^{-1}$ [46], could have of charge stability with a lifetime of a few hundred years in a dry environment [51].

The key issue in studying electret materials is to know how the charge distribution in an electret influence the electric field around it. A general theoretical analysis based on Gauss's law and the Kirchhoff's voltage law was also given by G. M. Sessler [46] as shown in **Figure 2- 2**.

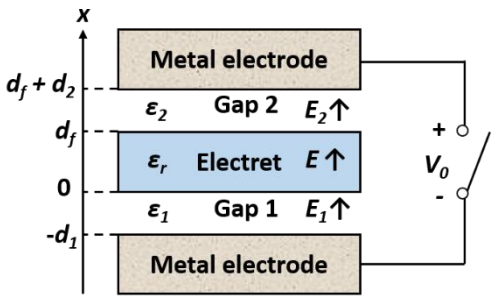

Figure 2- 2 The cross-section view of the general arrangement of a piece of electret with two dielectric gaps and two nearby metal electrodes analyzed by G. M. Sessler [46].

A piece of flat electret sheet in the middle with dielectric constant of ε_r and thickness of d_f was to be concerned in the model, with assuming that the dielectrics in the Gap 1 with dielectric constant of ε_1, thickness of d_1, and in the Gap 2 with permittivity of ε_2, thickness of d_2, cannot be charged, and all lateral dimensions were much greater than the thickness dimension. V_0 is the applied or generated voltage

across the two electrodes as illustrated in **Figure 2-2** when the switch is open-circuited. With such an arrangement, two significant inferences from Sessler's analysis will be introduced as follows.

The first one is that any charge distribution in the electret can be regarded as the electret has "projected" or "effective" surface charge distributions when investigating the induced external electric field around it. Assuming an arbitrary volume charge density $\rho(x)$ located at the vertical coordinate x with setting the bottom of the electret as the coordinate 0 as shown in **Figure 2-2**, then the corresponding equivalent effect charge density at the bottom and top surfaces of the electret can be calculated by:

$$\sigma_1 = \frac{1}{d_f}\int_0^{d_f} (d_f - x)\rho(x)dx \qquad (2\text{-}1)$$

$$\sigma_2 = \frac{1}{d_f}\int_0^{d_f} x\rho(x)dx \qquad (2\text{-}2)$$

where σ_1 and σ_2 are the effective surface charge density at the bottom and top surfaces of the electret surfaces respectively. The volume charge density $\rho(x)$ includes the "real" mono-charge density and gradient of the dipole polarization or microscopic charge displacement in the electrets [46]. All the planar charge density in this thesis refers to the effective surface charge density without a specific declaration.

The second one is that the electric field strength in the two gaps and in the electret can be calculated by:

$$\boldsymbol{E}_1 = -\frac{1}{d_0}\left(\frac{V_0}{\varepsilon_1} + \frac{d_f\sigma_1}{\varepsilon_0\varepsilon_1\varepsilon_r} + \frac{d_2(\sigma_1+\sigma_2)}{\varepsilon_0\varepsilon_1\varepsilon_2}\right) \qquad (2\text{-}3)$$

$$\boldsymbol{E}_2 = \frac{1}{d_0}\left(\frac{d_f\sigma_2}{\varepsilon_0\varepsilon_2\varepsilon_r} - \frac{V_0}{\varepsilon_2} - \frac{d_1(\sigma_1+\sigma_2)}{\varepsilon_0\varepsilon_1\varepsilon_2}\right) \qquad (2\text{-}4)$$

$$\boldsymbol{E}(x') = \frac{1}{d_0}\left(\frac{d_1(\sigma_1+\sigma_2)}{\varepsilon_0\varepsilon_1\varepsilon_r} - \frac{V_0}{\varepsilon_r} - \frac{d_2\sigma_2}{\varepsilon_0\varepsilon_2\varepsilon_r} - \frac{d_0^2}{\varepsilon_0\varepsilon_r}\left(\sigma_1 - \int_0^{x'}\rho(x)dx\right)\right) \qquad (2\text{-}5)$$

where ε_0 is the permittivity in the vacuum, $0<x'<d_f$, $\boldsymbol{E}_1$, $\boldsymbol{E}_2$, and $\boldsymbol{E}(x')$, are the electric field strength in the Gap 1, Gap 2, and in the electret at the vertical coordinate x' respectively, and d_0 can be termed as the total effective dielectric thickness defined by:

$$d_0 = \frac{d_1}{\varepsilon_1} + \frac{d_f}{\varepsilon_r} + \frac{d_2}{\varepsilon_2} \qquad (2\text{-}6).$$

The first inference simplifies the issues concerning the charge distributions in electrets, and the second inference is helpful for calculating the concerned electric field strengths from a given charge distribution. Note that these equations were

obtained with assumptions that the lateral dimensions of the electret and electrodes are the same and much larger than the thickness dimensions, and only the electret in the middle was charged.

2.2.2 Charging methods

The charging method used by Mototaro Eguchi [48] to make the first electret is now called as the thermal charging method. There are several different charging methods to make electrets as listed in **Table 2- 1**.

Table 2- 1 Different charging methods for making electrets [46, 52].

Charging methods	Brief procedure
Thermal charging	Heating and cooling in a constant electric field
Tribo-charging	Contact or friction on metallic or dielectric objects
Corona-charging	Corona discharge + electric field + possibly heating
Electron or ion injections	Injecting monoenergetic charged particle beams
Liquid contact charging	Applying an electric field via solid-liquid interfaces
Photo-charging	Photoelectric effect + applying an electric field
Radiation charging	High-energy radiation + applying an electric field

As can be noticed, most of the charging methods need an applied electric field. In this thesis, the tribo-charging method will be used to make the so-called "tribo-electret" without using any specific applied electric field. The tribo-charging method is based on the triboelectrification (TE) i.e. the charging of two objects due to the physical contact with each other [46, 53]. TE is a ubiquitous process that exists everywhere, anywhere, and at any time [53]. Especially, if the TE happens between two objects made with different materials, it is also called as the contact electrification (CE) [46]. It is believed that the electrostatic force caused by the CE-induced charges on dielectrics was discovered by a Greek philosopher Thales as early as 600 B.C. when he found that ambers after rubbed with clothes, could attract light objects such as bits of chaff [54]. Other familiar phenomena caused by CE include lightning during thunderstorms, sudden sparks of human bodies.

Though the phenomena caused by CE are so universal, the scientific understanding of the mechanism of CE remains inconclusive, it is likely that different mechanisms may be involved depending on the specific materials and environmental conditions [53, 55]. Z. L. Wang and A. C. Wang [53] reviewed recent researches on the CE mechanisms and proposed that the electron transfer due to the overlapping

electron cloud under mechanical force/pressure is the dominant mechanism for initiating CE between solids, liquids, and gases, as illustrated in **Figure 2-3**.

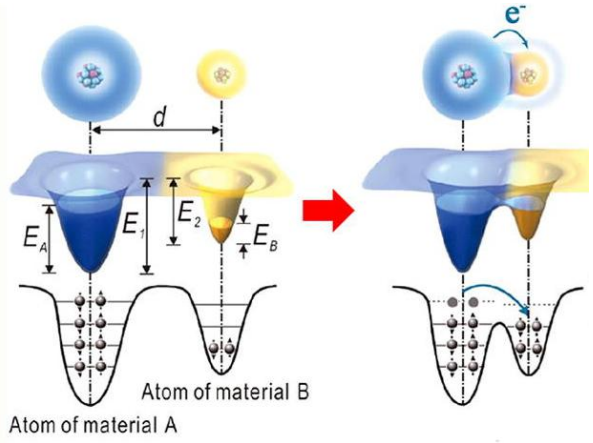

Figure 2-3 An electron-cloud-potential-well model proposed for explaining the contact electrification [53].

Zou et al. [56] quantified the tendency of several polymers to gain or lose electrons during the CE process with the liquid mercury and listed them in the triboelectric series which is instructive to choose materials for making tribo-electrets.

2.3 Basic principle and early researches of electret kinetic energy harvesters (E-KEHs)

2.3.1 Basic principle

Electret kinetic energy harvester (E-KEH) is one type of electrostatic energy harvester, consisting of at least one insulating electret and at least two conductive electrodes (electrical ground can be one of them). E-KEHs work based on the charge redistribution between the two electrodes through circuit load, under the electrostatic induction effect derived from the Coulomb's force.

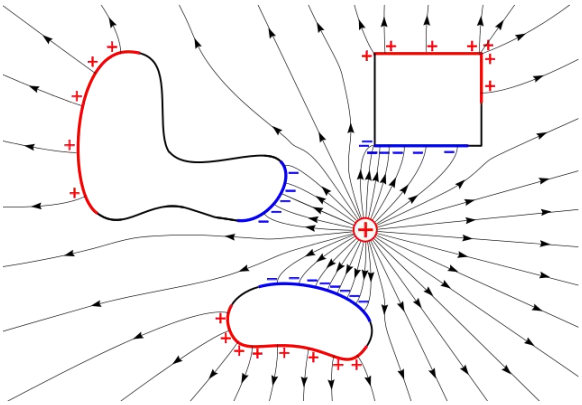

Figure 2-4 Schematic of the electrostatic induction effect on isolated conductive objects [57].

Generally speaking, the electrostatic induction effect means the charge redistribution driven by the Coulomb's force in an isolated conductive object under an electrostatic field to get the electrostatic equilibrium state in the conductive object itself as illustrated in **Figure 2-4**, while for an E-KEH, the electrostatic field is provided by an electret, the charge redistribution happens between at least two conductive electrodes connected through a load circuit, and the electrostatic equilibrium state is time-varying due to the relative movement among different components of the E-KEH under the force from an external kinetic energy source, as illustrated in **Figure 2-5**.

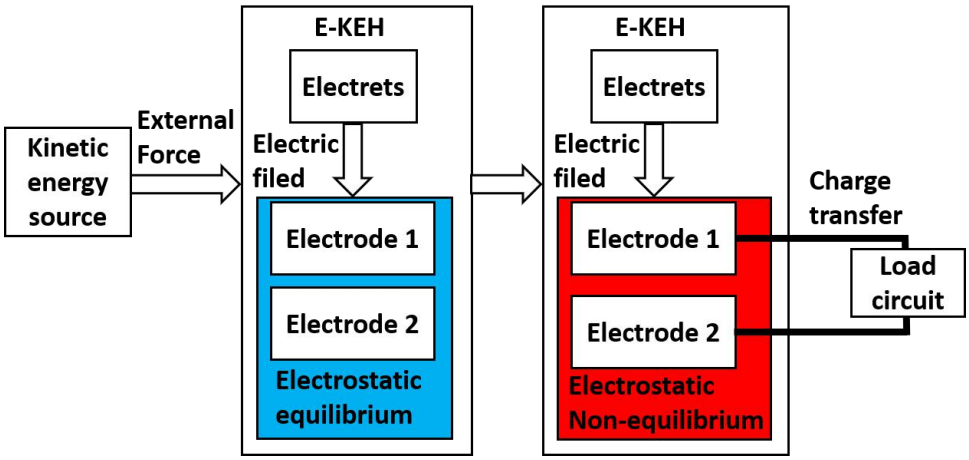

Figure 2-5 Schematic diagram for the basic working principle of an E-KEH.

2.3.2 Early researches

2.3.2.1 Electret transducers with variable capacitances

The basic working principle of E-KEHs was first applied to electret transducers that convert vibrations/forces into electric signals with the information of the

vibrations/forces for sensing. They usually have small dimensions, and the micro-scale relative displacements, with low-level output electric signals that need preamplifier for further signal processing. Therefore, electret transducers were usually not regarded as energy harvesters despite that they do convert kinetic energy into electricity.

It is believed that the research on electret transducers can be dated back to as early as 1929 when studies on electret microphones were going on in the United States [58]. Wax-electrets was used in electret microphones at first with drawbacks such as sensitivity fluctuations and the requirement for complex preamplifier design, then several thermoplastic electret plates and ceramic electret were suggested and attempted to be applied in electret microphones but not practically commercialized [58]. Until metalized thin electret foil made with Mylar [59, 60] and Teflon [61] were introduced into electret microphones in 1962 and 1965 by G. M. Sessler and J. E. West at Bell Laboratories, which greatly improved the performance and practicality of electret microphones, then commercialized electret foil microphones were manufactured numerously.

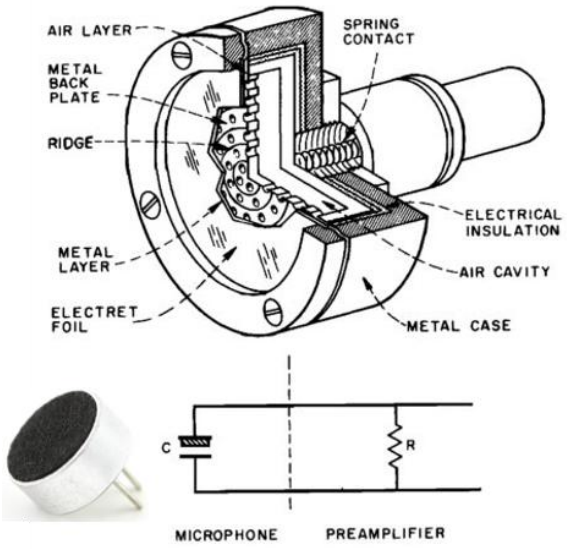

Figure 2-6 Cutaway drawing of a typical foil-electret microphone (top), the photograph of a commercial foil-electret microphone (bottom left), and corresponding schematic circuit diagram (bottom right) [58].

The structure of a typical electret foil microphone is shown in **Figure 2-6**. In an electret microphone, a piece of one side metalized electret foil with net homo-charges can be regarded as a constant voltage source, the sound wave vibrates a conductive backplate placed in face with the non-metalized side of the electret foil, changing the

capacitance between the backplate and the metalized side of the electret, generating output electrical signals in the external circuit connected with the backplate and the metalized side of the electret.

Besides the electret microphone, in 1976, an U.S. Patent invented by Raymond B. Basham was published, in which the possibility of utilizing Teflon electret film in a flexible force transducer to monitor the respiration of a patient was presented as shown in **Figure 2-7**. Flexible steel sheets were used as electrodes. The normal breathing motion of the patient procures a varying force against the electrodes, changing the distance and consequently the capacitance between the electrode and the electret film, generating output current to the signal processing circuit.

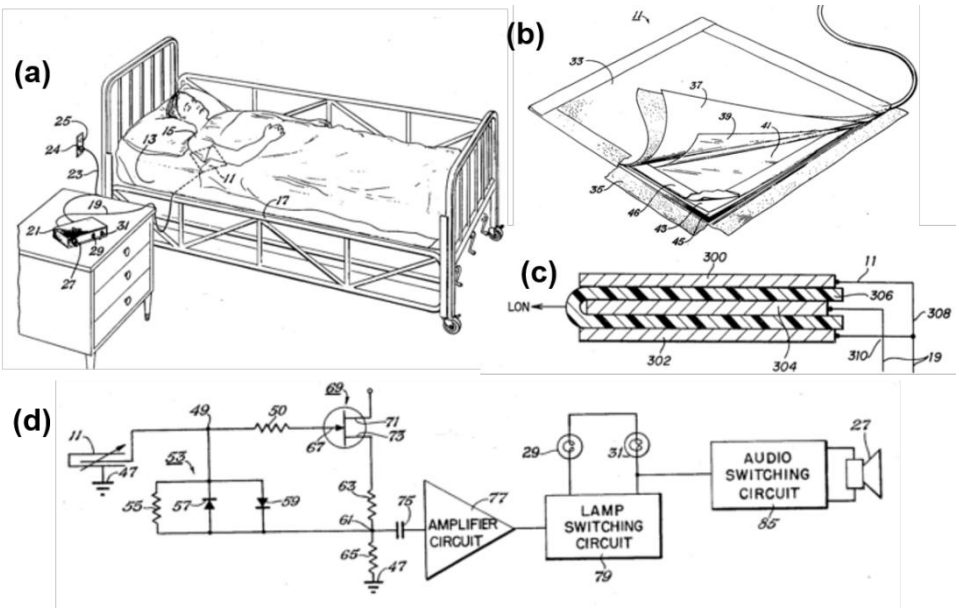

Figure 2-7 (a) A perspective view of the respiration monitoring apparatus positioned relative to a patient in bed with a force transducer. (b) A perspective view of the force transducer. (c) A cross-section view of an alternate embodiment of an electret force transducer. (d) An electrical schematic diagram showing a circuit with an amplifier unit for the force transducer to energize both a visual and an audible alarm to indicate cessation of respiration of the patient. Reproduced from the referenced patent [62].

Most of the later developed E-KEHs also use the variable capacitance strategy like electret transducers to generate electricity, but with more powerful kinetic energy sources, larger dimensions, and structures that can provide larger capacitance variations to get relative higher electric output.

2.3.2.2 Electret generators without variable capacitance

In addition to electret transducers using the variable capacitance strategy, in 1978, Oleg D. Jefimenko and David K. Walker [63] proposed a rotating electret generator (EG) consists of two oppositely polarized half-disks electret placed between two pairs of conducting half-disks as shown in **Figure 2-8**. In this EG, the charge-transfer between the two pairs of conducting half-disks was caused by the variation of the induced charge displacement on the two pairs of electrodes during the rotation of the two oppositely charged electrets disks, not by the variation of the capacitance. As marked by the red dashed oval in **Figure 2-8(b)**, the left conducting half-disk on one side of the EG was electrically connected with the right conducting half-disk on the other side to form an electrode, and other two conducting half-disks were electrically connected to form the other electrode of the EG.

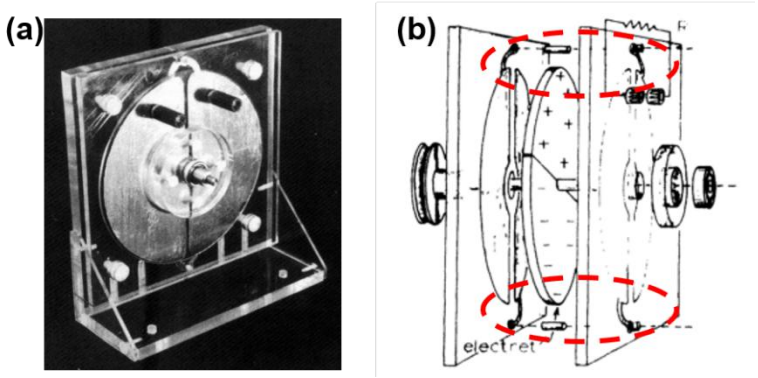

Figure 2-8 (a) The photograph and (b) the exploded view of the electret generator with two oppositely charged electret plates and the half-disk structure proposed by Oleg D. Jefimenko and David K. Walker [63].

Due to its relatively large dimension (disk diameter ~152.4 mm), this EG can output power of ~0.025 W at the rotation speed of 6000 r/min and with a load resistance of 10 MΩ, and it was regarded as the first practical E-KEH by later researchers [64, 65]. In the article [63], Oleg D. Jefimenko and David K. Walker also gave theoretical calculations on the output of the EG and pointed out its characteristics of high internal impedance and facility to provide a high voltage. Later in 1981~1986, Yasufusa Tada in Japan refined and extended the theoretical model of this type of EG using segmented electrets with opposite polarizations/charges [66].

In 1992, Yasufusa Tada published an article in which he reported an EG using Teflon FEP film electret with stable homo-charges [64], and the variable capacitance strategy was employed by varying the overlap area between the stator electrode and

the rotating electret film during rotations. After that, there emerged many studies on E-KEH using the variable capacitance strategy, which will be reviewed in the following section 2.4.

2.4 Different structures of E-KEHs with variable capacitances

2.4.1 A general introduction to E-KEHs with the parallel-plate configuration

The most common and simple structure of a capacitor is the parallel-plate configuration, which consists of dielectric materials sandwiched between two parallel-plate electrodes. For an ideal parallel plate capacitor, the capacitance ignoring the edge effect can be calculated by:

$$C = \frac{S\varepsilon_0}{d_0} \qquad (2\text{-}7),$$

where C is the capacitance, S is the electrode area, and d_0 is the effective dielectric thickness between the two electrodes, as defined by the equation *(2-6)* but with possible different layers of dielectrics.

For E-KEHs with variable capacitances, the parallel-plate configuration is also often used, with at least one layer of electrets and usually with an air gap as dielectric layers as illustrated in **Figure 2-9**.

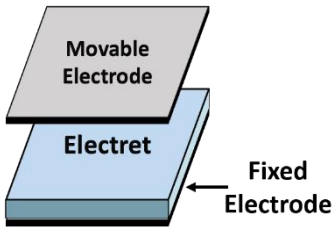

Figure 2-9 Illustration of the parallel-plate configuration of an E-KEH.

From equations *(2-6)* and *(2-7)*, variable overlap area, variable electrode distance, and variable dielectric constant are three basic approaches to construct parallel-plate E-KEHs with variable capacitances. Some structure designs corresponding to these three approaches are shown in **Figure 2-10**.

For the variable overlap area design, usually, one electrode of the E-KEH is fixed with the electret component, and the other electrode can do relative rotation, as shown in **Figure 2-10(a)**, or can have relative lateral displacements, as shown in

Figure 2-10(b). Otherwise, the two electrodes can be both fixed with the electret component, and a third conductive electrode (metal rotor) can do relative movement to change the overlap area of the third electrode with one fixed electrode in comparison with the other one, as shown in top of **Figure 2-10(c)**, or the two electrodes are fixed but the electret component is movable to change the overlap area of the electret with one fixed electrode in comparison with the other one, as shown in bottom of **Figure 2-10(c)**.

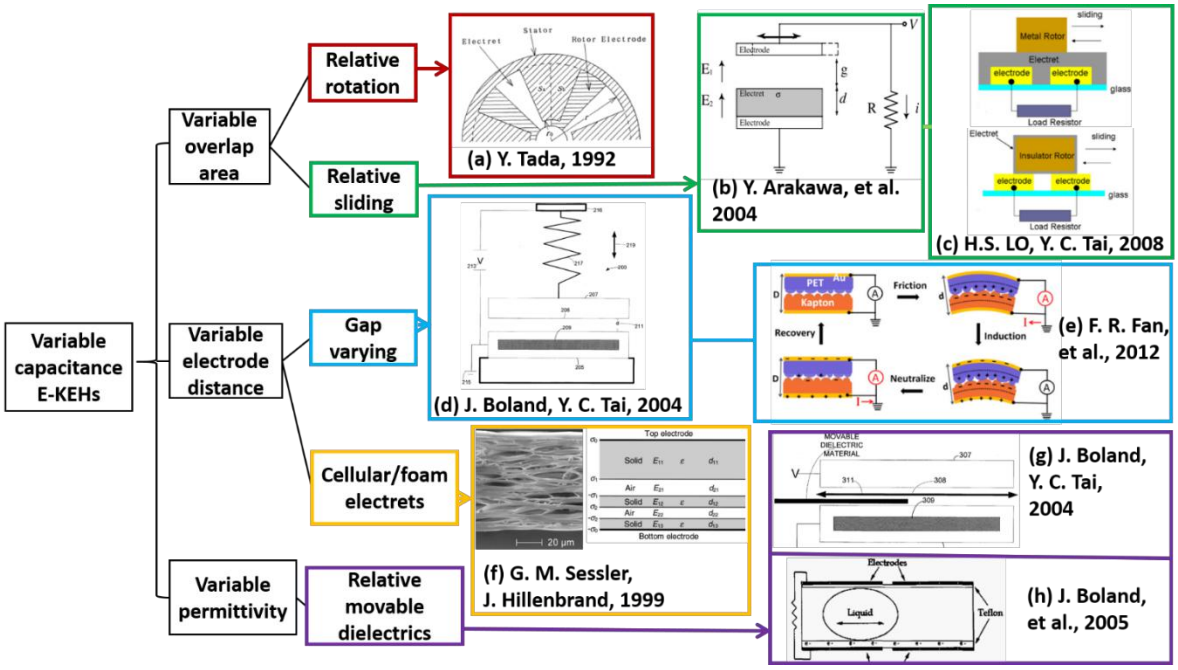

Figure 2-10 Different types of variable capacitance E-KEHs with representative material and structure designs. (a) Relative rotation design from [64]. (b) Relative sliding design from [67]. (c) Relative sliding design from [68]. (d) Gap-varying design from [69]. (e) Gap-varying design from [70]. (f) Cellular electret design from [71]. (g) The design with movable solid dielectrics from [69]. (h) The design with movable liquid dielectrics from [72].

For the variable electrode distance design, usually at least one electrode is fixed on one side of the electret component, and the air gap between the relatively movable electrode and the fixed electrode can be changed by external motions. The gap could vary in a large range as shown in **Figure 2-10(d)**, but also could vary in the scale of micrometers by the deformation of flexible electret films as shown in **Figure 2-10(e)**. Another type of variable electrode distance design is to use cellular/foam/porous electret films that can be easily deformed, with electrodes deposited on both sides as

shown in **Figure 2-10(f)**. A brief introduction to cellular electret films will be particularly presented in section 2.4.2.

For the variable permittivity design, besides the electret component, there is another dielectric material that is movable between the gap of the electret and electrodes. When the movable dielectric material is driven by external motions to move, the total or partial capacitance of the E-KEH is changed. The movable dielectric material could be solid as shown in **Figure 2-10(g),** or liquid as shown in **Figure 2-10(h)**. Like the design in **Figure 2-10(c)**, the variable permittivity design could also have both fixed electrodes. Since the electrodes of E-KEH need to output electricity to external circuit load, these designs with fixed both electrodes can greatly simplify the electric connection to external circuit load and reduce the damage risks to the electrodes and electric connectors, which is significant for developing E-KEHs with long life-times.

It is noteworthy that only several representative structure designs are presented in **Figure 2-10**, and they are based on the simple parallel plate capacitor configuration. In fact, any two separated objects with any geometric shape would have a mutual capacitance between them, and their relative movement would, of course, change the capacitance value. Furthermore, even only one object can form a capacitance if regarding the environment around that object as a virtual electric ground [73]. The basic definition of capacitance is the ratio of the change in the electric charge (Q) of a system to the corresponding change in its electric potential (V), as expressed by:

$$C = \frac{Q}{V} \qquad (2\text{-}8).$$

The capacitance can be even considered as a geometrical parameter [74]. Therefore, besides the structure designs in **Figure 2-10**, there are diverse other structures of E-KEH, some of them will be introduced in section 2.4.3.

2.4.2 Cellular/foam/porous piezo-electrets/ferro-electrets

In the cellular electret design represented by the research shown in **Figure 2-10(f)**, when the cellular electret film is pressed or released, the distance between the two electrodes on the top and bottom sides of the electret film changes, it can also be regarded as the effective permittivity of the electret film changes, since it contains the

solid matrix (usually polymers) and the gas (usually air) in inner cavities as two different dielectrics, and when the film is deformed, the volume ratio of these two dielectrics will be changed. These cellular electret films can be charged with excess homo positive or negative charges, but are often charged with space charges (macroscopic dipole moments) on the top and bottom sides of inside cavities as illustrated in **Figure 2-11(a)**.

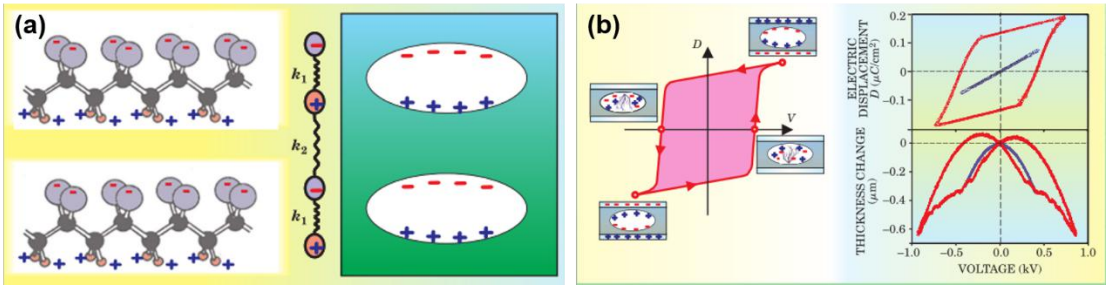

Figure 2-11 Illustrations of (a) the analogy between the microscopic dipole moment in ferroelectrics (left) and the macroscopic dipole moment (right) in ferro-electrets, and (b) the ferroelectric-like characteristics of ferro-electrets obtained via the micro-plasma discharge inside the cavities, from [75].

When a cellular electret film charged with space charges is pressed or released, it performs like a piezoelectric material since the total macroscopic diploe moments of the electret film is changed with the deformation of the film caused by the press or elastic force, so it is called as piezo-electret [76-79]. Since the elastic modulus of the cellular electret films are usually much lower than piezoelectric ceramics, and the effective dipole moment density can be much higher than that in conventional piezoelectric materials, the apparent electromechanical d_{33} coefficient of piezo-electret can be much higher than conventional piezoelectric ceramics. For instance, a tremendous d_{33} of 3350 pC/N was obtained in a composite cellular piezo-electret film using PTFE and PDMS [80], which is much higher than one of the best piezoelectric ceramics PZT with d_{33} of ~250 to 700 pC/N. The high d_{33} makes cellular electrets competitive in energy harvesting. Moreover, cellular electret films can also show ferroelectric characteristics via the micro-plasma discharge inside their cavities as shown in **Figure 2-11(b)**, so they were also termed as ferro-electrets [75]. A recent review on cellular polymer ferro-electret and their piezoelectric properties was given by A. Mohebbi [81] for those who are interested.

2.4.3 Triboelectric nanogenerator (TENG) or tribo-electret kinetic energy harvester (TE-KEH) with diverse structure designs

In the article corresponding to **Figure 2-10(e)**, authors didn't particularly pre-charge the dielectric polymer films but took advantage of the triboelectrification effect to introduce electrostatic charges on these films, making them become tribo-electret. E-KEHs using tribo-electret were called as triboelectric generators (TEGs) [70], and later termed as triboelectric nanogenerators (TENGs) to distinguish them from traditional high voltage sources using the triboelectrification effect (such as the Wimshurst machine and the Van de Graaff generator [82, 83]). In this thesis, E-KEHs using tribo-electrets will be termed as TE-KEHs to better express their basic principle and functionality. In recent years, a large and drastically increasing number of researches on TE-KEHs were conducted [84], especially by the team of Z. L. Wang who proposed the conception of TE-KEHs [83], and pre-charged electrets were also used in several of these researches on TE-KEHs [85-90] to get higher output power.

Like other E-KEHs, not only the gap-varying structure in **Figure 2-10(e)** but also other types of structure designs were used in TE-KEHs for different working modes as illustrated in **Figure 2-12**. Among these diverse designs, the free-standing relative sliding modes in **Figure 2-12(c)** and **(i)**, and the free-standing gap-varying modes in **Figure 2-12(e)** have fixed both electrodes, and the electret is free-standing and movable.

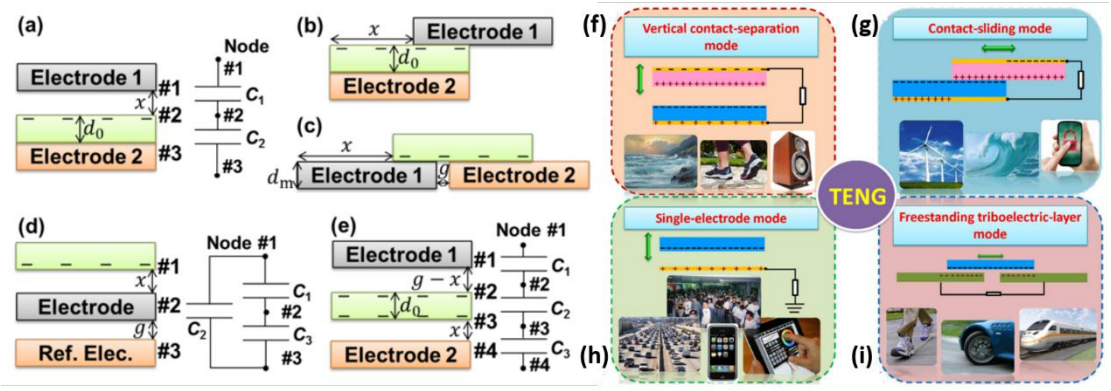

Figure 2-12 Basic structure designs and working modes of TE-KEHs. On the left: illustrations of TE-KEHs with (a) the gap-varying, (b) the relative sliding, (c) the freestanding relative sliding, (d) the single-electrode gap-varying, and (e) the freestanding gap-varying designs, with virtual capacitances illustrated, from [91]. On the right, illustrations of TE-KEHs working under the (f) vertical contact-separation mode, (g) in-plane sliding mode, (h) single-electrode mode, and (i)

free-standing sliding electret mode, with the external electric load and potential application scenes illustrated, from [92].

In some TE-KEHs, the electrical ground was used as one electrode, the load circuit was connected between one electrode of the TE-KEH and the electrical ground as illustrated in **Figure 2-12(h)** and **Figure 2-13(a)**, they were regarded as single-electrode TE-KEHs [93, 94]. The electrets in TE-KEHs not only could be planar [95] [88, 93] but also could be flexible [70, 96-99], stretchable [100], and shape-adaptive [101, 102] as shown in **Figure 2-13(b)** and **(c)**, or fiber-shaped that can be woven into cloth to harvest human body motion energy [103] as shown in **Figure 2-13(d)**. The general shape of TE-KEHs could also be curved [104, 105] or arch-shaped [106] as shown in **Figure 2-13(e)**, cylindrical [107] as shown in **Figure 2-13(f)**, tubular [108-110] as shown in **Figure 2-13(g)**, polyhedral [89] or spherical [111, 112] as shown in **Figure 2-13(h)**. Moreover, to get more power from environmental kinetic energy sources, the integration of multiple TE-KEHs is important, which could be distributed [112-116] as shown in **Figure 2-13(i)**, or stacked in multi-layer [117-119] as shown in **Figure 2-13(j)**.

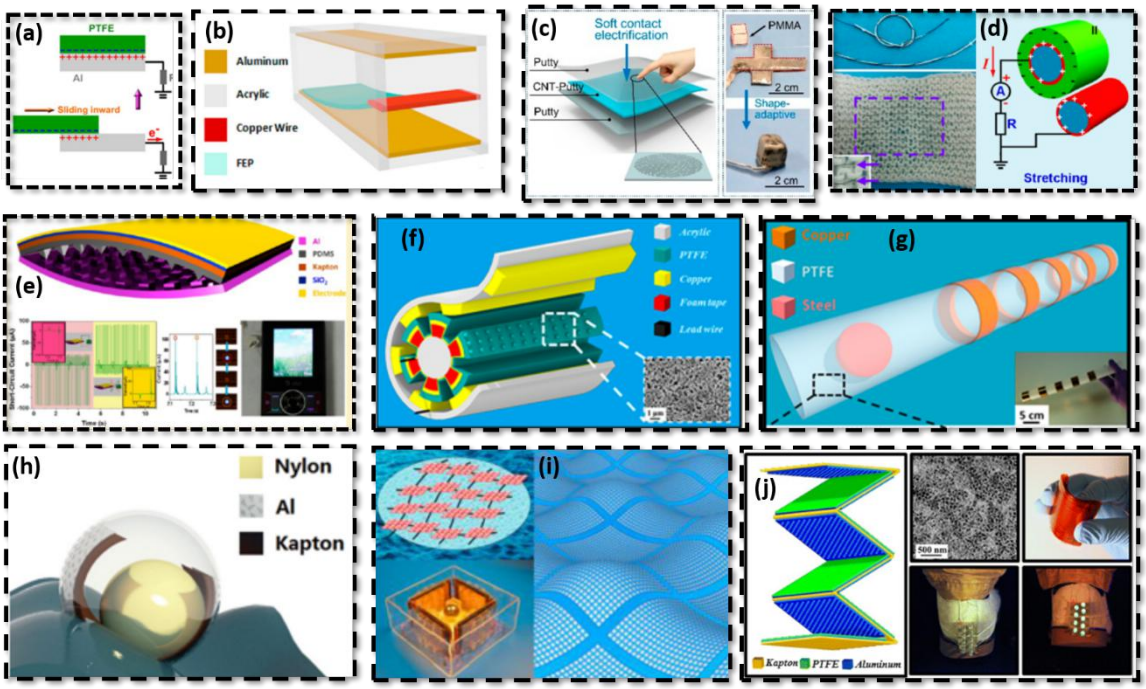

Figure 2-13 Diverse structure and integration designs of TE-KEHs. (a) Sliding mode single-electrode structure [93]. (b) With flexible electret film for harvesting wind energy by fluttering [98]. (c) With shape-adaptive electret film [101]. (d) With electret fibers that can be woven [103]. (e) Arch-shaped TE-EKH [106]. (f) Cylindrical TE-EKH [107]. (g) Tubular TE-KEH [110]. (h) Spherical TE-KEH

[111]. (i) Distributed network integration of multiple TE-KEHs [113]. (j) Stacked integration of multiple TE-KEHs [119].

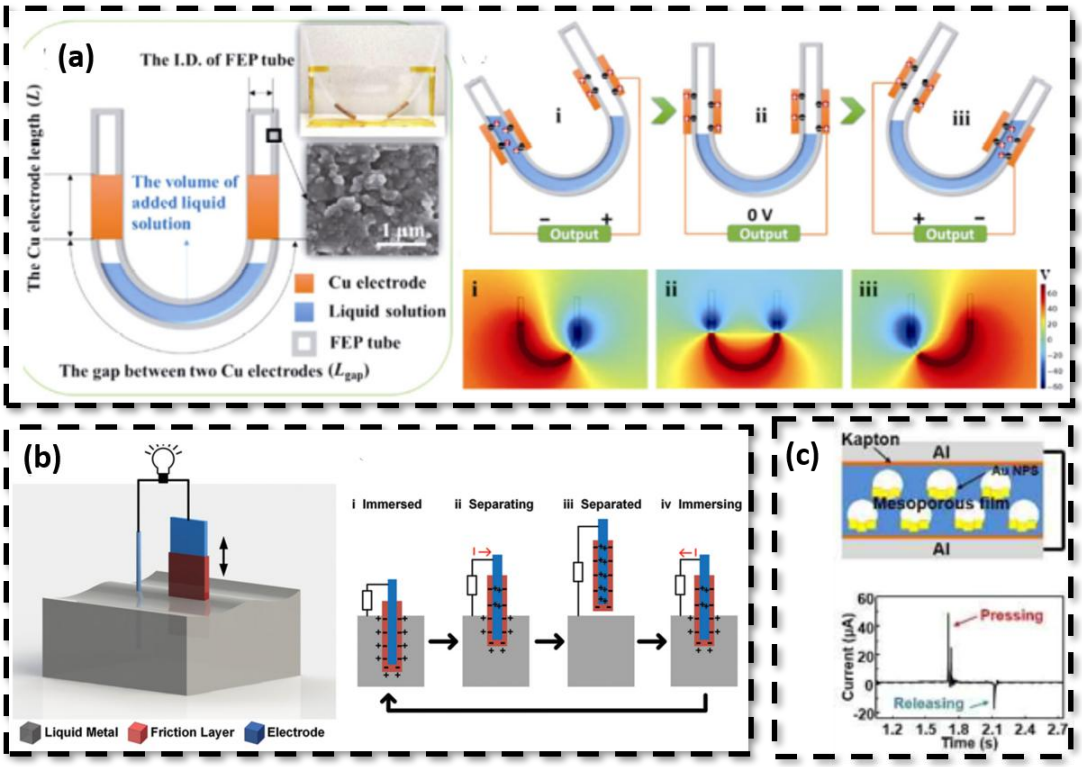

Figure 2-14 (a) A U-tube shaped TE-KEH filled with liquid dielectrics [109]. (b) A TE-KEH with liquid metal as an electrode [120]. (c) A TE-KEH using the electret of mesoporous PDMS film impregnated with gold nanoparticles [121].

The movable liquid dielectric strategy was also used in TE-KEH [109] as shown in **Figure 2-14(a).** In some other articles, liquid metals were used as the electrode that can have relative movements with the electrets in TE-KEHs, as illustrated in **Figure 2-14(b)**, to get a larger transferred tribo-charge amount [91, 120] for better performance of TE-KEHs. Besides, constructing meso/micro/nano-structures on the surface of electret or electrode materials [82, 102, 107, 119, 122-125] as illustrated in **Figure 2-13(e)**, **(f)**, **and (j)**, or cellular/porous structures [86, 121, 126, 127] inside electret materials as illustrated in **Figure 2-14(c)**, are other two often-used strategies to improve the output power of TE-KEHs. A book [4] and several reviews [83, 92, 99, 114, 128, 129] on TE-KEHs were published for those who are interested.

2.4.4 Direct motion-driven mode and undirect vibration-driven mode

With different structures, E-KEHs can be driven by external kinetic sources by basically two different modes, one is the direct motion-driven mode which means the motion of the movable component of the E-KEH is directly determined by the motion

of the external kinetic source, while the other one is the undirect vibration-driven mode which means the motion of the movable component of the E-KEHs is determined by both the motion of the external kinetic source and the mechanical properties of the E-KEH itself.

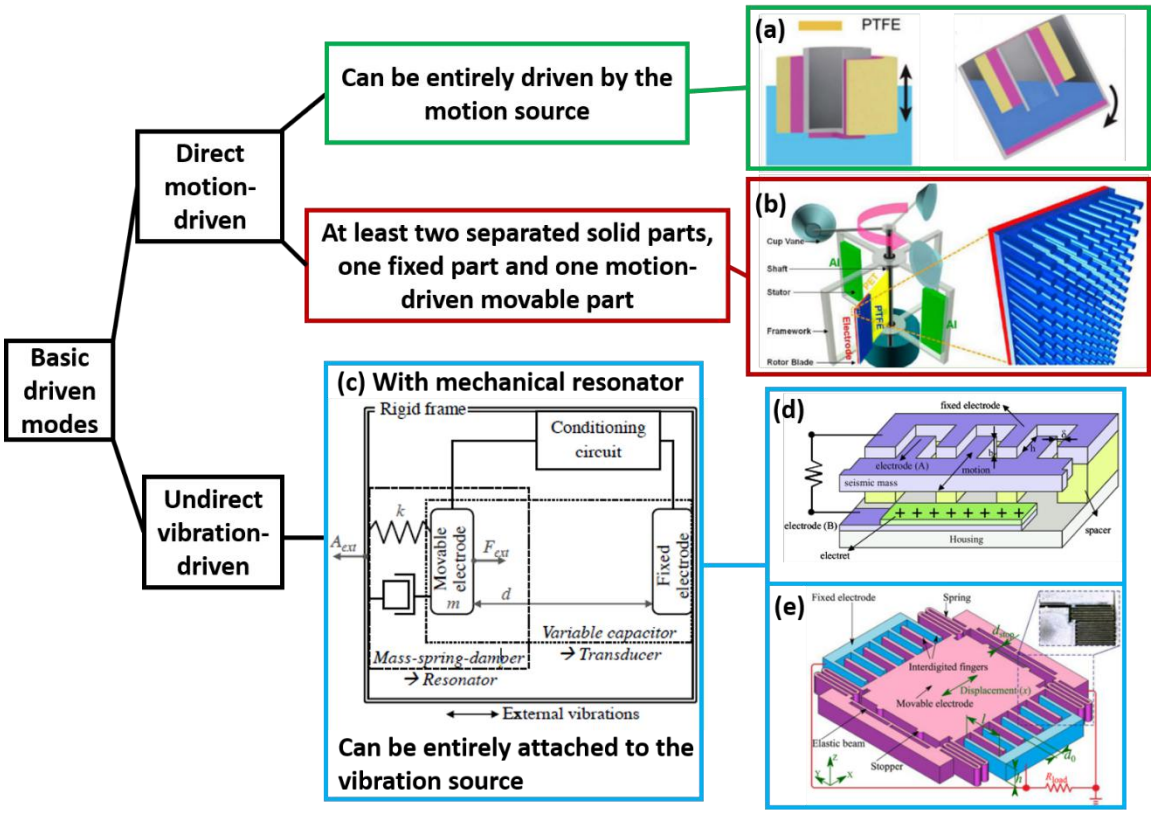

Figure 2-15 Different driven modes of E-KEHs. (a) An E-KEH with the entire structure driven by water wave motion [115]. (b) A wind-driven E-KEH with a rotating part and a stator part [130]. (c) The scheme of a KEH with a mechanical resonator structure for transferring energy from the vibration source to the electromechanical transducer [74]. (d) A micro vibration-driven E-KEH with the mechanical resonator structure, using the variable overlap area and electrode distance combined design [131]. (e) A micro vibration-driven E-KEH with the mechanical resonator structure, using the gap-varying design [132].

For the direct motion-driven mode, the external excitation force to directly drive the movable component of the E-KEH is much larger than the transduction electrostatic force, and the effect of the transduction force on the motion of the kinetic energy source is negligible. For instance, in a water wave-driven buoy-like E-KEH [115] shown in **Figure 2-15(a)**, external water can be part of the E-KEH as movable dielectrics (on the left), or a direct motion source to shake the E-KEH and lead to the waggle of the inner liquid dielectrics, and the electrostatic force is considered to have no effect on the water flow. This buoy-like E-KEH can be entirely placed on the sea

to harvest kinetic energy from waves. While for most of the direct motion-driven E-KEHs, there are at least two solid components with one fixed and the other one movable. For instance, in a wind-driven rotary E-KEH [130] shown in **Figure 2-15(b)**, there are aluminum sheets as stator electrodes and one side metalized PTFE electret film on a rotary shaft driven by the wind as the rotor blade. A small part of the kinetic energy from wind can be converted to electricity via the wind-driven relative movement between the stator and the rotor of the E-KEH.

For vibration-driven E-KEHs that usually contain a mechanical resonator structure modeled by a spring-mass-damper system as shown in **Figure 2-15(c)**, the external excitation force act on the variable capacitor through the resonator structure, and the transduction force is considered to act as a damper in the resonator model. Vibration-driven E-KEHs can be entirely attached to the vibration source, and the relative movement between different parts of the electromechanical transduction unit was provided by the resonator structure excited by the vibration source. The variable capacitance design in vibration-driven E-KEHs can be a combined design of variable overlap area and variable electrode distance as shown in **Figure 2-15(d)**, can also be a gap-varying design as shown in **Figure 2-15(e)**.

The direct motion-driven mode is usually applied to E-KEHs with relatively large dimensions (from a few to tens of centimeters) for harvesting kinetic energy from low-frequency (often less 10 Hz) motions [133-135]. While the undirect vibration-driven mode is usually applied to tiny/micro E-KEHs (dimensions from a few millimeters to a few centimeters), for harvesting kinetic energy from vibrations with low to high frequency (several Hz to 1~2 kHz) [131, 136, 137] dependent on the nature frequency of the E-KEH (usually smaller E-KEHs have higher nature frequency).

2.5 Different analysis models for E-KEHs with variable capacitances

2.5.1 The compact equivalent electrical model for direct motion-driven E-KEHs

For direct motion-driven E-KEHs, there is no need to solve the equation of motion of the movable component of the E-KEHs if the motion of the external kinetic source is given. Though there are so many different structure designs for E-KEHs as

introduced in section 2.4, the parallel-plate configuration is often used to simplify the modeling of KEHs.

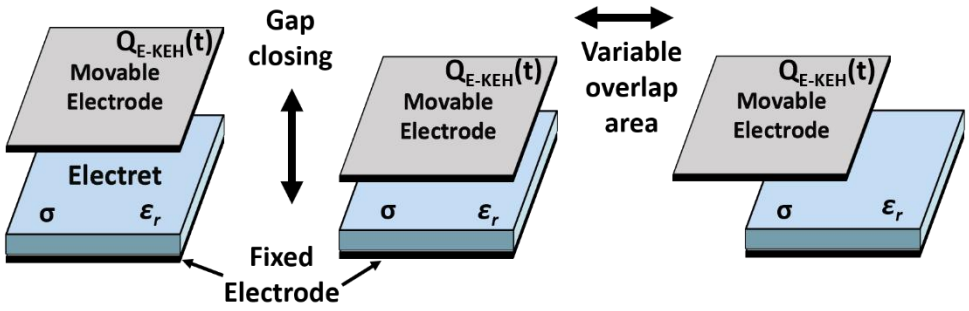

Figure 2- 16 Parallel-plate configurations of E-KEHs.

For a direct motion-driven E-KEH based on the parallel-plate configuration as illustrated in **Figure 2- 16**, one electrode keeps fixed with the electret layer, and the movable electrode is driven by a given external motion, the time-varying total capacitance ($C_{E\text{-}KEH}$) of the E-KEH without considering the fringe effect can be calculated as:

$$C_{E-KEH}(t) = \frac{S(t)\varepsilon_0}{d_0(t)} \qquad (2\text{-}8)$$

where $S(t)$ is the time-varying overlap area of the two electrodes, and d_0 is the effective dielectric thickness of the E-KEH. Assuming the electret layer is a rigid body, and the dielectric in the gap between the electret layer and the movable electrode is air, there is:

$$d_0(t) = \frac{d_f}{\varepsilon_r} + z(t) = d_{0f} + z(t) \qquad (2\text{-}9)$$

where d_f, ε_r, and d_{0f} are the thickness, dielectric constant, and effective dielectric constant of the electret layer respectively, and $z(t)$ is the time-varying air gap between the electret layer and the movable electrode.

Assuming the electret layer has a homogeneous effective surface charge density of σ, the total net charge of the E-KEH including charges on both electrodes and the electret is 0 (hypothesis of neutrality [74]), then the E-KEH can be regarded as a variable capacitance connected in series with a constant voltage source, as illustrated in **Figure 2- 17**. The C_{par} is the possible parasitic capacitance in the circuit, and $Q_{E\text{-}KEH}(t)$ is the charge amount on the movable electrode. The constant voltage source V_{ele} is the surface potential of the electret film defined as:

$$V_{ele} = \frac{\sigma d_f}{\varepsilon_0 \varepsilon_r} = \frac{\sigma d_{0f}}{\varepsilon_0} \quad (2\text{-}10),$$

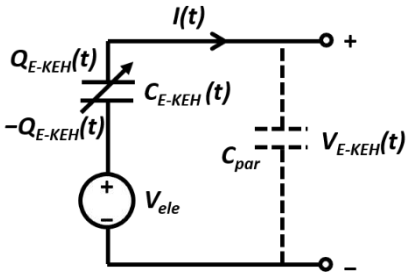

Figure 2- 17 The compact equivalent electrical model of an E-KEH with a time-varying total capacitance.

Where the movable electrode is regarded as a positive electrode. If C_{par} is ignorable, according to the Kirchhoff's voltage law, the output voltage of the *E-KEH* can be calculated as:

$$V_{E-KEH}(t) = V_{ele} + \frac{Q_{E-KEH}(t)}{C_{E-KEH}(t)} \quad (2\text{-}11).$$

According to the charge conservation, the output current can be calculated as:

$$I(t) = -\frac{dQ_{E-KEH}(t)}{dt} \quad (2\text{-}12).$$

The positive direction of the current is marked in **Figure 2- 17.**

If the external circuit load is a resistor *R*, according to Ohm's law, there is:

$$V_{E-KEH}(t) = I(t)R \quad (2\text{-}13).$$

Combining (2-9) ~ (2-11), there is:

$$V_{ele} + \frac{Q_{E-KEH}(t)}{C_{E-KEH}(t)} + R\frac{dQ_{E-KEH}(t)}{dt} = 0 \quad (2\text{-}14).$$

If the value of V_{ele} and the analytical form of $C_{E\text{-}KEH}(t)$ are known, and the initial condition $Q_{E\text{-}KEH}(0)$ is given, then the first-order linear differential equation (2-14) about the time-varying $Q_{E\text{-}KEH}(t)$ can be analytically solved as:

$$Q_{E-KEH}(t) = e^{-\frac{\int_0^t \frac{1}{C_{E\text{-}KEH}(u)}\,du}{R}} \left(Q_{E-KEH}(0) - \frac{V_{ele}\int_0^t e^{\frac{\int_0^w \frac{1}{C_{E\text{-}KEH}(u)}\,du}{R}}\,dw}{R} \right) \quad (2\text{-}15)$$

where *u* and *w* are intermediate variables for the integration. Then the $I(t)$ and $V_{E\text{-}KEH}(t)$ can be obtained from the equations *(2-12)*, *(2-13)*, and *(2-15)*.

Note that this compact equivalent circuit model is only useful when the $C_{E\text{-}KEH}$ is time-varying with a known analytical form. For some E-KEHs with time-varying partial capacitances but with a constant $C_{E\text{-}KEH}$, such as the freestanding structure designs illustrated in **Figure 2- 12(c), (e),** and **(i)**, this model is not applicable. A detailed equivalent electrical model [74, 138] that contains each partial capacitance would be helpful to theoretically analyze the output of the E-KEHs with time-varying partial capacitances but constant $C_{E\text{-}KEH}$.

2.5.2 The electromechanical model for undirect vibration-driven E-KEHs

For micro KEHs to be used in microelectromechanical systems (MEMS), the entire encapsulation is important for the ease of use. One significant encapsulation strategy for KEHs is incorporated with a resonator (passive oscillator [139]) structure. One function of the resonator structure is to amplify the relative displacement among different parts of the transduction unit in a KEH from vibration sources with a small amplitude by the phenomenon of resonance [65]. Other possible functions of the resonator structure are to modulate the natural resonance frequency (ω_n), bandwidth, and quality factor of the E-KEH for better mechanic-electric coupling [139]. Moreover, KEHs with a resonator structure only need to be mechanically anchored to one point and thus can simply be fixed to any moving body to generate electricity [140].

2.5.2.1 A general 1 degree-of-freedom linear damping model for vibration mechanic analysis

C. B. Williams and R. B. Yates analyzed a micro vibration-electric generator with a resonator structure using a spring-mass-damper model, for all types of mechanic-to-electric energy harvesters with an emphasis on an electromagnetic micro-generator [140, 141]. They regarded the three possible mechanic-electric transduction mechanisms (electromagnetic, piezoelectric, and electrostatic) just as three approaches to providing the damping force (the Ampere's force for the electromagnetic, the Coulomb's force for the piezoelectric and electrostatic) that fulfills the mechanic-to-electric conversion. And they analyzed the motion equation of the generator with regarding the transduction damping force as a linear (also termed

as viscous) damping force, which means the damping force is linearly proportional to the movement velocity with a proportionality coefficient.

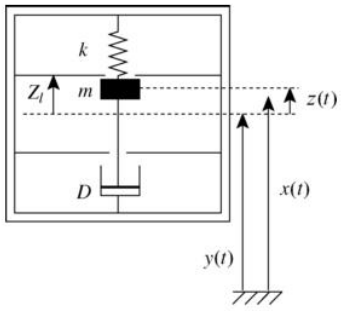

Figure 2-18 Schematic diagram of the micro-electric generator with a seismic mass, from [142].

A more detailed derivation of the spring-mass-damper model with linear damping was given by S.J. Roundy [2] and Paul D. Mitcheson et al. [142] using the Laplace transform. The schematic of this general mechanical model is shown in **Figure 2-18.** In the diagram **Figure 2-18**, *m* is the mass of seismic/proof/inertial mass block that could have relative movements with the frame of the generator, *D* is the damping coefficient of the transduction process which is dependent not only on the generator itself but also on the load circuit, *k* is the equivalent spring constant of the vibration structure in the generator, *y(t)* is the displacement of the generator frame caused by external vibrations, *x(t)* is the displacement of the inertial mass, *z(t)* is the relative mass-to-frame displacement that equals $x(t) - y(t)$. There is $z=0$ if there is no external excitation and the mass is at its equilibrium position.

In this model, only the one-dimensional motion of the mass needs to be analyzed if the motion from an external vibration source is given, which makes it become a 1 degree-of-freedom (DOF) vibration problem. And since the transduction damping force is always considered as a linear damping force whatever type the real force is, the model is called a general 1 DOF linear damping model in this thesis.

The differential equations of motion and power transfer of this model according to Newton's second law were listed as follows [140, 141]:

$$m\ddot{z}(t) + D\dot{z}(t) + kz(t) = -m\ddot{y}(t) \qquad (2\text{-}14)$$

$$p(t) = -m\ddot{y}(t)[\dot{y}(t) + \dot{z}(t)] \qquad (2\text{-}15),$$

where *p(t)* is the instantaneous mechanical power transfer in the mass block. If ignoring all the energy loss from parasitic damping caused by an undesired effect

such as the air drag and hysteresis loss in the suspension, during steady-state periodic energy conversion working cycles, all the energy transferred to the mass should be converted to electric energy [139]. The steady-state generated electrical power when the generator frame was excited by a harmonic vibration source, $y(t)=Y_0\cos(\omega t)$, was therefore calculated as [140-142]:

$$P = \frac{m\zeta Y_0^2(\frac{\omega}{\omega_n})^3\omega^3}{[1-(\frac{\omega}{\omega_n})^2]^2+[2\zeta\frac{\omega}{\omega_n}]^2} = \frac{\zeta\omega_c{}^3 m Y_0^2\omega^3}{[1-(\omega_c)^2]^2+[2\zeta\omega_c]^2} \qquad (2\text{-}16),$$

where $\omega_c = \omega/\omega_n$, Y_0 is the vibration amplitude of the external vibration source, and ζ is the transducer damping ratio of the mechanic-to-electric transduction which is a dimensionless parameter defined as:

$$\zeta = \frac{D}{2\sqrt{mk}} = \frac{D}{2m\omega_n} \qquad (2\text{-}17).$$

It should be noted that the equation *(2-16)* was obtained with ignoring parasitic damping, and other practical limitations such as the limitation on the maximum vibration amplitude (Z_l) of the inertial mass.

The ζ can be optimized to get the maximum generated power. Without considering the Z_l, by finding the extreme point from the equation *(2-16)*, there are [142]:

$$\zeta_{opt} = \frac{|\omega_c{}^2-1|}{2\omega_c} \qquad (2\text{-}18)$$

$$P_{max} = \frac{\omega_c{}^2 Y_0^2\omega^3 m}{4|\omega_c{}^2-1|} \qquad (2\text{-}19),$$

where ζ_{opt} is the stationary point on $dP/d\zeta$, and P_{max} is the corresponding maximum generated power.

The amplitude of the mass-to-frame vibration is related to ζ by [142]:

$$Z_0 = \frac{Y_0\omega_c{}^2}{\sqrt{(1-\omega_c{}^2)^2+(2\zeta\omega_c)^2}} \qquad (2\text{-}20).$$

If ζ_{opt} calculated by the equation *(2-18)* leads to $Z_0 > Z_l$, which means that the optimized ζ_{opt} can't be obtained by the generator due to the constraint in its geometric limitation, the ζ should be tuned to as close to ζ_{opt} as possible to get the maximum achievable generated power, there are [142]:

$$\zeta_{optCZ} = \frac{1}{2\omega_c}\sqrt{{\omega_c}^4(\frac{Y_0}{Z_l})^2 - (1-{\omega_c}^2)^2} \qquad (2\text{-}20)$$

$$P_{maxCZ} = \frac{Y_0^2\omega^3 m}{\omega_c}(\frac{Z_l}{Y_0})^2\zeta_{optCZ} = Y_0^2\omega^3 m\frac{1}{2{\omega_c}^2}(\frac{Z_l}{Y_0})^2\sqrt{{\omega_c}^4(\frac{Y_0}{Z_l})^2 - (1-{\omega_c}^2)^2} \qquad (2\text{-}21)$$

, where ζ_{optCZ} is the optimal damping ratio of the generator with the constrain of $Z_0 = Z_l$, and P_{maxCZ} is the corresponding maximum generated power by the generator.

When the KEH works at the resonant frequency, which means ω_c, there are:

$$\zeta_{optres} = \frac{Y_0}{2Z_l} \qquad (2\text{-}22)$$

$$P_{maxres} = \frac{1}{2}Y_0^2\omega^3 m\frac{Z_l}{Y_0} \qquad (2\text{-}23)$$

, where ζ_{optres} is the optimal damping ratio of the generator if it works at the resonant frequency, and P_{maxres} is the corresponding maximum generated power by the generator.

If taking the undesired parasitic damping with the damping ratio ζ_p into consideration, the equations *(2-16)* and *(2-18)* should be modified as [142, 143]:

$$P = \frac{\zeta{\omega_c}^3 m Y_0^2\omega^3}{[1-(\omega_c)^2]^2+[2(\zeta+\zeta_p)\omega_c]^2} \qquad (2\text{-}24)$$

$$\zeta_{opt} = \frac{1}{2\omega_c}\sqrt{1-2{\omega_c}^2+{\omega_c}^4+4{\omega_c}^4{\zeta_p}^2} \qquad (2\text{-}25).$$

A significant undesired parasitic damping will apparently reduce the output electrical power of a KEH, therefore ζ_p should be as low as possible to get the maximum output power. Note that other practical constraints such as the limitation on the achievable ζ range and on the vibration power source are not considered in this model. And the theoretical generated power is calculated during the steady-state working cycles of the generator. The practical output power of the generator must be lower than the theoretical value due to other possible energy losses due to the charge leakage, operational overhead, electrical losses in the circuit, etc. [142]. Nevertheless, this model provides a method to analyze the vibration-driven KEHs from a mechanical point-of-view, which is important to further analyze the electromechanical coupling of KEHs.

2.5.2.2 A complete electromechanical model for vibration-driven E-KEHs

The general 1 DOF linear damping model was firstly applied on micro electromagnetic generators [141, 144, 145], these generators were called as the velocity-damped resonant generator (VDRG) [142]. For electrostatic energy harvesters, the Coulomb's force that implement the mechanic-electric energy conversion can't be simply modeled as a linear damping force. Paul D. Mitcheson et al. [142] also proposed a coulomb-damped resonant generator (CDRG) model for electrostatic generators working under the constant voltage or constant charge model, and a coulomb-force parametric generator (CFPG) model for the case where $(Z_l/Y_0)<0.1$. However, all these models mainly focused on vibration mechanics, which are not intuitively related to the electric domain.

S. Boisseau, G. Despesse, and A. Sylvestre established a complete electromechanical model [65, 146] which combined both the theoretical analysis on the mechanic domain [140, 142] and the electric domain [63, 64, 147] of E-KEHs as shown in **Figure 2-19(a)**, based on a microstructured E-KEH proposed by Yoshihiko Sakane, et al. [148], and a cantilever-based E-KEH [146] fabricated by themselves. The active energy transduction component of the cantilever-based E-KEH is a one-side metalized electret film facing a counter electrode as shown in **Figure 2-19(b)**. In their experiments, the electret film is a piece of corona-charged Teflon FEP film with the rear side evaporated with a layer of alumina as the electrode, and the counter electrode is a silicon cantilever with a mass on the free end as shown in **Figure 2-19(c)**. An equivalent electric circuit was used analyze the electric output of the E-KEH as shown in **Figure 2-19(d)**, in which the charged electret film was regarded as a constant voltage source V and the total capacitance between the two electrodes was considered as a time-varying capacitor $C(t)$.

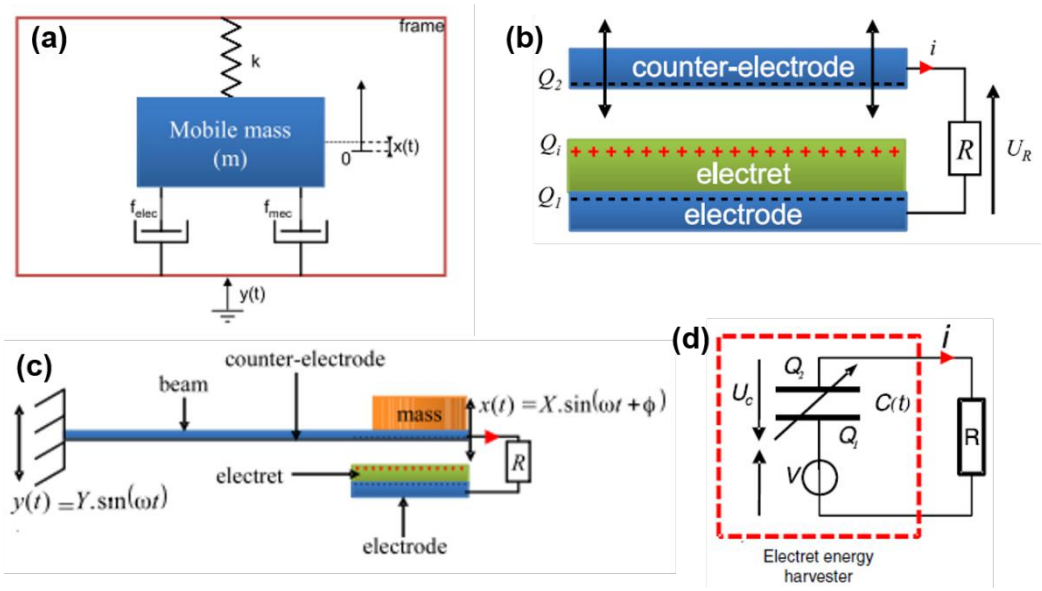

Figure 2-19 The complete electromechanical model for the undirect vibration driven cantilever-based E-KEH, from [146]. (a) The mass-spring-damper mechanical model concerning both the undesired mechanical friction force f_{mec} and the transduction electrostatic force f_{elec}. (b) The cross-section scheme of the energy conversion component and (c) the entire structure of the cantilever-based E-KEH. (d) The equivalent circuit model of the E-KEH.

In this complete electromechanical model, the undesired mechanical damping force, which causes the energy loss, was modeled as a linear (viscous) damping force f_{mec} with a damping coefficient of D_m, and the electrostatic force f_{elec} between the electret and the counter-electrode was calculated by [74]:

$$f_{elec} = -\frac{dW_e}{dx} = -\frac{1}{2}\frac{d}{dx}\left(\frac{Q_2^2(t)}{2C(t)}\right) = \frac{1}{2}\frac{Q_2^2(t)}{C^2(t)}\frac{dC}{dx} \qquad (2\text{-}26)$$

where x is the deflection of the silicon cantilever at the lateral position of the center of the mass, and W_e is the electrostatic energy stored in the $C(t)$ calculated by:

$$W_e = \frac{Q_2^2(t)}{2C(t)} \qquad (2\text{-}27)$$

where $-Q_2(t)$ is the charge amount on the counter electrode.

Here, the f_{elec} is a nonlinear damping force. When the clamped end of the cantilever is excited by an external vibration source $y(t)$, combing the mechanical model illustrated in **Figure 2-19(a)** and the equivalent circuit model illustrated in **Figure 2-19(d)**, there is:

$$\begin{cases} m\ddot{x} + D_m\dot{x} + kx + \frac{1}{2}\frac{Q_2^2(t)}{C^2(t)}\frac{dC}{dx} - mg = -m\ddot{y} \\ \frac{dQ_2(t)}{dt} = \frac{V}{R} - \frac{Q_2(t)}{RC(t)} \end{cases} \qquad (2\text{-}28).$$

In the mechanical motion equation of (2-28), k is the equivalent spring constant of the cantilever structure, and g is the gravitational acceleration. The weight of the mass was taken into consideration because it would always lead to a deflection of the cantilever.

With the analytical function *C(x)* and the dependence of *k* on the geometric parameters of the cantilever structure being deduced, with given $y(t) = Y\sin(\omega t)$ and all parameter values, Sebastien Boisseau et al. [146] numerically solved the equation set *(2-28)* in Simulink. They also considered the effect of the parasitic capacitance in the whole system by adding a constant capacitor C_{par} in parallel with the *E-KEH* and the resistor as shown in **Figure 2-20**.

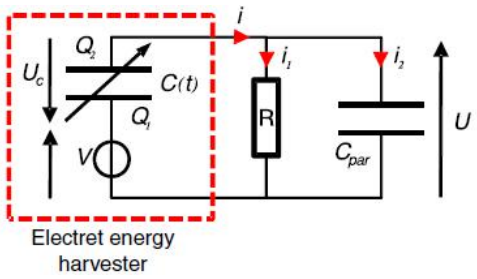

Figure 2-20 The equivalent circuit model of the *E-KEH* taking the effect of the parasitic capacitance into consideration [146].

Correspondingly, the second equation in *(2-28)* was modified to:

$$\frac{dQ_2}{dt} = \frac{C(t)}{(C(t)+C_{par})}\left(\frac{V}{R} - Q_2\left(\frac{1}{RC(t)} - \frac{C_{par}}{C(t)}\frac{dC(t)}{dt}\right)\right) \qquad (2\text{-}29).$$

From both the simulation results in Simulink and experimental data, Boisseau et al. [146] pointed out that the parasitic capacitance would decrease the harvested power especially when the load resistance is higher than the impedance induced by the parasitic capacitance.

2.5.2.3 Lumped-parameter equivalent circuit model

Another electromechanical modeling method for undirect-vibration driven E-KEHs is based on the lumped-parameter equivalent circuit model. In 1994, Gary Keith Fedder presented this method in his thesis [149], in which he proposed an electrical analogy of the mass-spring-damper system to an inductor-capacitor-resistor

(LCR) circuit, as illustrated in **Figure 2-21**, and he also gave the time-varying capacitor model in SPICE software as shown in **Figure 2-22**.

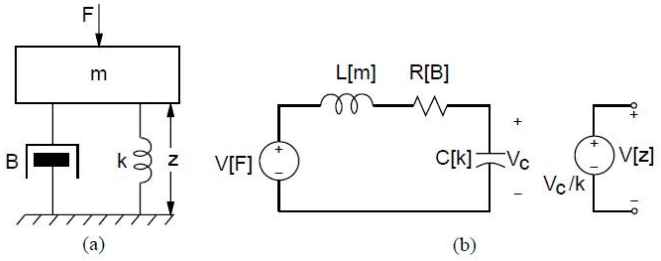

Figure 2-21 Electrical analogy to a mechanical system [149]. (a) A mechanical mass-spring-damper system. (b) The equivalent LCR circuit.

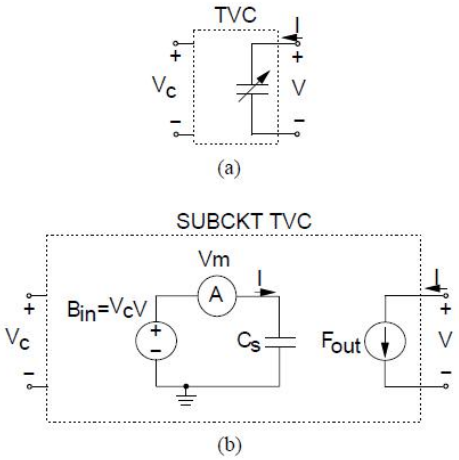

Figure 2-22 The time-varying capacitor model in SPICE [149]. (a) Circuit instance. (b) Sub-circuit.

With the equivalent circuit analog of the mass-spring-damper system and the time-varying capacitor model in SPICE, Gary Keith Fedder simulated the output voltage of micro a position sensor based on the parallel-plate variable capacitance structure, which could also be an electrostatic actuator. This method is also applicable to vibration-driven E-KEHs since they have basically the same electromechanical model with the position sensor.

Harrie A.C. Tilmans [150, 151] also employed the analog of mechanical systems to the equivalent circuit to analyze the mechanic-electric coupling in electromechanical transducers. He proposed several possible equivalent circuits for EM-, PE-, and ES- mode transducers. D. Galayko and P. Basset [152] used the concept of the mechanical impedance based on the mechanic-electric analog to

analyze the performance of first-harmonic vibration-driven KEHs, as illustrated in **Figure 2-23**.

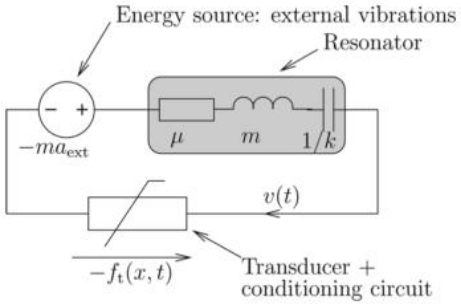

Figure 2-23 Equivalent electrical representation of the mechanical domain of the vibration energy harvester [152].

The mechanical impedance of the mechanic-electric transducer together with the conditioning circuit in the energy harvester was defined as [152]:

$$\Psi_t = -\frac{\dot{F}_t^{\omega}}{\dot{v}} \qquad (2\text{-}30)$$

where Ψ_t is the mechanical impedance, $\dot{F}_t^{\omega}$ is the complex amplitude of the fundamental harmonic of the complex Fourier series of the electrostatic transduction force, and $\dot{v}$ is the complex amplitude of the sinusoidal velocity of the moving component of the energy transducer. It was deduced that the energy harvester would harvest the maximal power when the real part of Ψ_t is maximal in steady states.

2.6 Chapter remarks

In summary, E-KEHs are quite application-specific power sources. Many different structure designs for E-KEHs are introduced in this chapter, most of them are based on the variable capacitance principle. The variable capacitance of E-KEHs can be the total or partial capacitances of the E-KEHs. Driving modes of E-KEHs are divided into two categories: the direct motion-driven mode and the undirect vibration-driven mode. Several different analytical models to analyze the output of E-KEHs are also introduced.

This page is intentionally left blank

Chapter 3 Amplitude-variable output characteristics of a contact-separation mode E-KEH during multiple transitory working cycles

3.1 Introduction

The analytical solution of the compact equivalent electrical model for the direct motion-driven parallel-plate E-KEHs has been introduced in section 2.5.1. In this chapter, the general analytical solution of the detailed equivalent electrical model for a direct motion-driven contact-separation (CS) mode (which means a gap-varying mode with a minimum air gap of 0) parallel-plate E-KEH is given in section 3.2. Then simulations of the output voltage/current/power of the E-KEH based on this model are presented in section 3.3. Most previous theoretical researches on E-KEHs focused on the steady-state output of E-KEHs driven by harmonic motions [35, 153, 154]. Though some researchers already obtained asymmetric and amplitude-variable simulation results of output voltage [18, 35] or current [154] of E-KEHs, the detailed cause of these characteristics need to be further discussed, which could be helpful for optimizing the performance of E-KEHs. In section 3.3, the reason for the asymmetric and amplitude-variable output characteristics of the E-KEH, and their dependence on the load resistance are discussed based on the simulated results. The output power of the E-KEH with different load resistances and initial conditions are analyzed using the QV cycle analysis method. At last, in section 3.4, the asymmetric and amplitude-variable output voltage of an E-KEH made with PTFE film is verified by both experimental and simulated data.

3.2 Analytical solution of the detailed equivalent electrical model for a contact-separation mode E-EKH

3.2.1 The analytical solution with arbitrary initial conditions

A simplified CS mode E-KEH with three rigid-body components (one electret film layer and two electrodes) is taken as the research object of this chapter. The structure of the E-KEH is illustrated in **Figure 3-1(a)**, and the cross-section sketch of the E-KEH is shown in **Figure 3-1(b)**. In the sketch, σ is the effective homogenous

surface charge density on the top side of the electret film, S is the area of the electret film, ε_r and d_f is the dielectric constant and the thickness of the electret film respectively, $z(t)$ is the time-varying air gap distance, $Q(t)$ is the time-dependent charge amount on the back electrode (the polarity of $Q(t)$ is opposite with σ), and R is the load resistance in the external circuit. Using the hypothesis of neutrality [74] to the E-KEH, the charge amount on the top electrode is $-\sigma S-Q(t)$. The electret film was regarded as a perfect electret without charge decay, which means σ was considered as a constant. The planar dimensions of the electret film and the two electrodes are the same, which are assumed to be much larger than d_f and the maximum $z(t)$, which means the fringe effect of the electric field is always negligible.

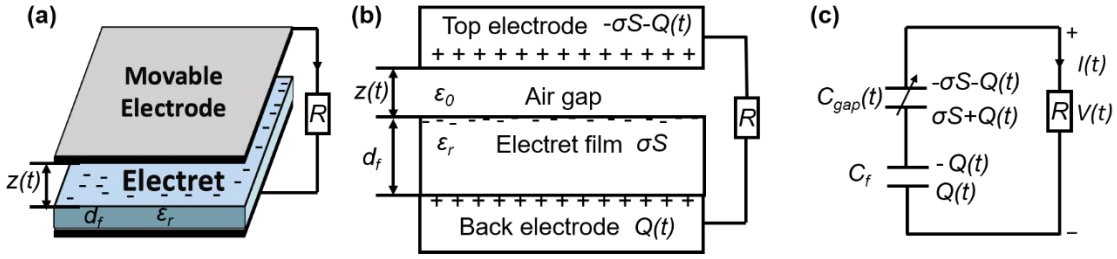

Figure 3-1 (a) The schematic of the CS mode E-KEH. (b) The cross-section structure of the E-KEH. (b) The detailed equivalent electrical model of the E-KEH.

Figure 3-1(c) shows the detailed equivalent electrical model of the E-KEH, where $C_{gap}(t)$ represents the variable capacitance formed by the air gap between the top electrode and the top surface of the electret film, which is variable with the variation of $z(t)$, C_f represents the capacitance between the back electrode and the top surface of the electret film. The value of C_f and $C_{gap}(t)$ ignoring the fringe capacitance can be calculated by:

$$C_f = \frac{S\varepsilon_0\varepsilon_r}{d_f} = \frac{S\varepsilon_0}{d_{0f}} \qquad (3\text{-}1)$$

$$C_{gap}(t) = \frac{S\varepsilon_0}{z(t)} \qquad (3\text{-}2)$$

where d_{0f} is the effective dielectric thickness of the electret film defined as d_f/ε_r [155]. With the relative approaching and separating movement between the top electrode and the electret film, $C_{gap}(t)$ changes with $z(t)$ while C_f keeps unchanged.

According to the Gauss' law, the back electrode holds an electric potential of $Q(t)/C_f$, while the top electrode holds an electric potential of $(-\sigma S-Q(t))/C_{gap}(t)$, both

taking the top surface of the electret film as the reference. The potential difference between these two electrodes is the output voltage $V_{E\text{-}KEH}(t)$ of the E-KEH. If regarding the top electrode as the positive electrode, there is:

$$V_{E-KEH}(t) = \frac{-\sigma S - Q(t)}{C_{gap}(t)} - \frac{Q(t)}{C_f} \qquad (3\text{-}3)$$

The $V_{E\text{-}KEH}(t)$ leads to the charge-transfer between the top and back electrodes, which give rise to an output current $I(t)$ in the circuit. According to charge conservation, there is:

$$I(t) = \frac{dQ(t)}{dt} \qquad (3\text{-}4)$$

On the other hand, applying Ohm's law to the load resistance, there is:

$$V_{E-KEH}(t) = I(t)R \qquad (3\text{-}5).$$

Substitute *(3-1) ~ (3-4)* to *(3-5)*, there is

$$R\frac{dQ(t)}{dt} + \frac{\sigma z(t)}{\varepsilon_0} + \frac{Q(t)\left(d_{0f}+z(t)\right)}{S\varepsilon_0} = 0 \qquad (3\text{-}6).$$

It's easy to prove that the differential equation *(3-6)* is equivalent to the equation *(2-14)* based on the compact equivalent electrical model with the help of the equations *(2-8) ~ (2-10)* and the following substitution:

$$Q_{E-KEH}(t) = -\sigma S - Q(t) \qquad (3\text{-}7).$$

Note that the total capacitance $C_{E\text{-}KEH}(t)$ of the E-KEH equals the series connection of C_f and $C_{gap}(t)$, which is:

$$C_{E-KEH}(t) = \frac{C_f C_{gap}(t)}{C_f + C_{gap}(t)} = \frac{S\varepsilon_0}{d_{0f}+z(t)} \qquad (3\text{-}8).$$

Therefore, both the compact and detailed electrical models are applicable to the CS mode E-KEH. The compact model is more concise, while the detailed model is more intuitive.

For the first-order linear differential equation *(3-6)* about $Q(t)$, if $Q(0)$ is given, and $z(t)$ has a known analytical form, it can be analytically solved as:

$$Q(t) = \left[Q(0) - \frac{\sigma}{R\varepsilon_0}\int_0^t z(w)exp\left(\frac{\int_0^w (d_{0f}+z(u))du}{RS\varepsilon_0}\right)dw\right] exp\left(-\frac{\int_0^t (d_{0f}+z(u))du}{RS\varepsilon_0}\right) \qquad (3\text{-}9)$$

where u and w are intermediate variables for the integration.

I(t) can be derived from *(3-4)* and *(3-9)* as:

$$I(t) = \frac{(d_{0f}+z(t))}{RS\varepsilon_0}\left[\frac{\sigma}{R\varepsilon_0}\int_0^t z(w)exp(\frac{\int_0^w (d_{0f}+z(u))du}{RS\varepsilon_0})\ dw - Q(0)\right]exp(-\frac{\int_0^t (d_{0f}+z(u))\,du}{RS\varepsilon_0}) - \frac{\sigma z(t)}{R\varepsilon_0} \quad (3\text{-}10).$$

Then $V_{E\text{-}KEH}(t)$ can be easily obtained from *(3-5)* and *(3-10)*, and the output power *P(t)* of the E-KEH to the load resistance can be calculated by the Joule's law as:

$$P(t) = I^2(t)R \quad (3\text{-}11).$$

3.2.2 The initial electric equilibrium assumption

The equation *(3-9)* gives the analytical solution of *Q(t)* without specifying *Q*(0). Now assuming the E-KEH starts working from the electric equilibrium state, which means $V_{E\text{-}KEH}(0) = 0$, according to the equations *(3-1) ~ (3-3)*, there are:

$$\frac{Q(0)}{C_f} + \frac{\sigma S+Q(0)}{C_{gap}(0)} = 0 \quad (3\text{-}12)$$

$$Q(0) = \frac{-\sigma S z(0)}{d_{0f}+z(0)} \quad (3\text{-}13).$$

With this assumption, the initial condition *Q*(0) can be easily obtained from the equation *(3-13)* once *z*(0) is given.

For instance, for the most used case [122, 155, 156] *z(0)* = 0, the initial condition is *Q(0)* = 0, the equation (3-9) becomes:

$$Q(t) = \left[-\frac{\sigma}{R\varepsilon_0}\int_0^t z(w)exp\left(\frac{\int_0^w (d_{0f}+z(u))du}{RS\varepsilon_0}\right)\ dw\right]exp\left(-\frac{\int_0^t (d_{0f}+z(u))\,du}{RS\varepsilon_0}\right) \quad (3\text{-}14).$$

For another case *z(0)* = z_{max}, where z_{max} is the maximum air gap during the working of the E-KEH, there are:

$$Q(0) = \frac{-\sigma S z_{max}}{d_{0f}+z_{max}} = Q_{max} \quad (3\text{-}15)$$

$$Q(t) = \left[Q_{max} - \frac{\sigma}{R\varepsilon_0}\int_0^t z(w)exp(\frac{\int_0^w (d_{0f}+z(u))du}{RS\varepsilon_0})\ dw\right]exp(-\frac{\int_0^t (d_{0f}+z(u))\,du}{RS\varepsilon_0}) \quad (3\text{-}16).$$

The simulation results in section 3.3 are mainly based on these two cases together with this initial electric equilibrium assumption.

3.2.3 The short-circuit current and the open-circuit voltage

The short-circuit current and the open-circuit voltage of E-KEHs are two of the most widely used indicators to evaluate the performance of E-KEHs.

In the short-circuit condition, there always is $V_{E\text{-}KEH}(t) = 0$, which means the top and back electrodes of the CS mode E-KEH are always at the electrical equilibrium state. If using $Q_{eq}(t)$ instead of $Q(t)$ to represent the charge amount on the back electrode in the short-circuit condition for distinction, according to the equation *(3-3)*, there is:

$$Q_{eq}(t) = \frac{-\sigma S z(t)}{d_{0f}+z(t)} \qquad (3\text{-}17).$$

The short-circuit current is:

$$I_{eq}(t) = \frac{dQ_{eq}(t)}{dt} = \frac{-\sigma S d_{0f} v(t)}{(d_{0f}+z(t))^2} \qquad (3\text{-}18)$$

where $v(t)$ is the relative movement velocity of the top electrode with respect to the electret film, which can be obtained by:

$$v(t) = \frac{dz(t)}{dt} \qquad (3\text{-}19).$$

In the open-circuit condition, there always is $Q(t) = Q(0)$, $I(t) = 0$, according to the equations (3-1) ~ (3-3), the open-circuit voltage of the CS mode E-KEH is:

$$V_{oc}(t) = \frac{-\sigma S - Q(0)}{C_{gap}(t)} - \frac{Q(0)}{C_f} = \frac{-\sigma z(t)}{\varepsilon_0} - \frac{(d_{0f}+z(t))Q(0)}{S\varepsilon_0} \qquad (3\text{-}20).$$

3.3 Simulation results and discussion

3.3.1 Parameters for the simulation

Based on section 3.2, the $Q(t)$, $I(t)$, $V_{E\text{-}KEH}(t)$, and $P(t)$ of the CS mode E-KEH can be simulated when the driving motions and parameter values are given, by using a symbolic differential equation solver *"dsolve"* in MATLAB to solve the equation *(3-6)*. In previous researches, mainly two types of movements were studied for the CS mode E-KEHs. One is a single separation process with a given average velocity [155], the other one is regular harmonic movements [35, 157]. Here, a piecewise acceleration-uniform motion-deceleration cyclic movement, which can be realized by a linear motor system in our laboratory, was used to simulate the output of E-KEH.

For comparison with other research, the same geometrical (thickness and area of electret film), material parameters (permittivity and surface charge density), and movement speed during the uniform motion with references [35, 155] were used, except that both large acceleration and deceleration of ±100 m/s^2 were used to make the movement reciprocating and cyclic. The detailed parameter values are listed in **Table 3-1**.

Table 3-1 Parameter values used in simulating the output of E-KEH for comparisons with the literature [35, 155]

Parameter	Value
Area of electret film S	9 inch^2
The dielectric constant of the electret film ε_r	3.4
The thickness of the electret film d_f	125 μm
Effective surface charge density on the electret film σ	-10 μC/m^2
Maximum air gap z_{max}	1 mm
Minimum air gap	0
Acceleration a_1	100 m/s^2
Maximum speed v_1	0.1 m/s
Deceleration a_2	-100 m/s^2
Deceleration a_3	-100 m/s^2
Maximum speed v_2	-0.1 m/s
Acceleration a_4	100 m/s^2

At first, the case $z(0) = 0$ was considered. The $z(t)$ was described by the following periodic piecewise function:

$$z(t) = \begin{cases} \frac{a_1 t^2}{2} (0 \le t < t_1) \\ \frac{{v_1}^2}{2a_1} + v_1(t - t_1)(t_1 \le t < t_2) \\ z_{max} + \frac{a_2(t-t_3)^2}{2} (t_2 \le t < t_3) \\ z_{max} + \frac{a_3(t-t_3)^2}{2} (t_3 \le t < t_4) \\ z_{max} + \frac{{v_2}^2}{2a_3} + v_2(t - t_4)(t_4 \le t < t_5) \\ \frac{a_4(t-T)^2}{2} (t_5 \le t < T) \\ z(t - T)(t \ge T) \end{cases} \quad (3\text{-}21)$$

$$with\begin{cases} t_1 = \frac{v_1}{a_1} \\ t_2 = \frac{z_{max}}{v_1} + \frac{v_1}{2a_1} + \frac{v_1}{2a_2} \\ t_3 = \frac{z_{max}}{v_1} + \frac{v_1}{2a_1} - \frac{v_1}{2a_2} \\ t_4 = \frac{z_{max}}{v_1} + \frac{v_1}{2a_1} - \frac{v_1}{2a_2} + \frac{v_2}{a_3} \\ t_5 = \frac{z_{max}}{v_1} + \frac{v_1}{2a_1} - \frac{v_1}{2a_2} - \frac{z_{max}}{v_2} + \frac{v_2}{2a_3} + \frac{v_2}{2a_4} \\ T = \frac{z_{max}}{v_1} + \frac{v_1}{2a_1} - \frac{v_1}{2a_2} - \frac{z_{max}}{v_2} + \frac{v_2}{2a_3} - \frac{v_2}{2a_4} \end{cases} \quad (3\text{-}22)$$

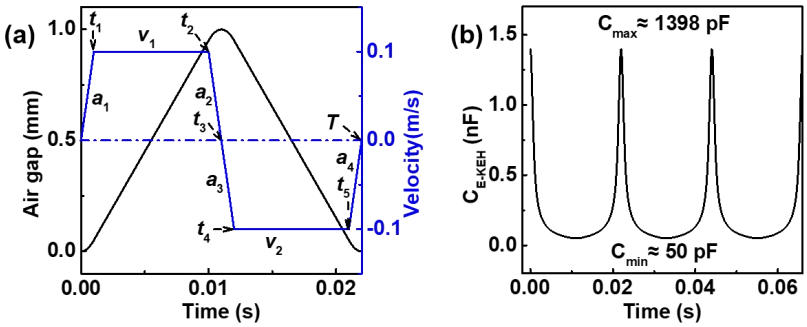

Figure 3-2 (a) Simulated *z(t)*, *v(t)*, and (b) $C_{E\text{-}KEH}(t)$, in the case *z*(0) = 0.

The movement defined by the equations *(3-21)* and *(3-22)* and the corresponding parameter values in **Table 3-1** is cyclic and reciprocating with symmetric *z(t)* and *v(t)* profiles in both separating and approaching directions. **Figure 3-2(a)** shows the simulated *z(t)* and *v(t)* during one movement cycle, with the period (*T*) of 0.022s. **Figure 3-2(b)** shows the corresponding $C_{E\text{-}KEH}(t)$ calculated by the equation (3-8) during three motion cycles.

3.3.2 Charge-transfer process

For the case *z*(0) = 0, *Q*(0) = 0, **Figure 3-3** shows corresponding simulated charge-transfer processes between the two electrodes of the E-KEH in the first three motion cycles with load resistances of 1 MΩ, 100 MΩ, and 1 GΩ respectively. Many information can be obtained from this figure.

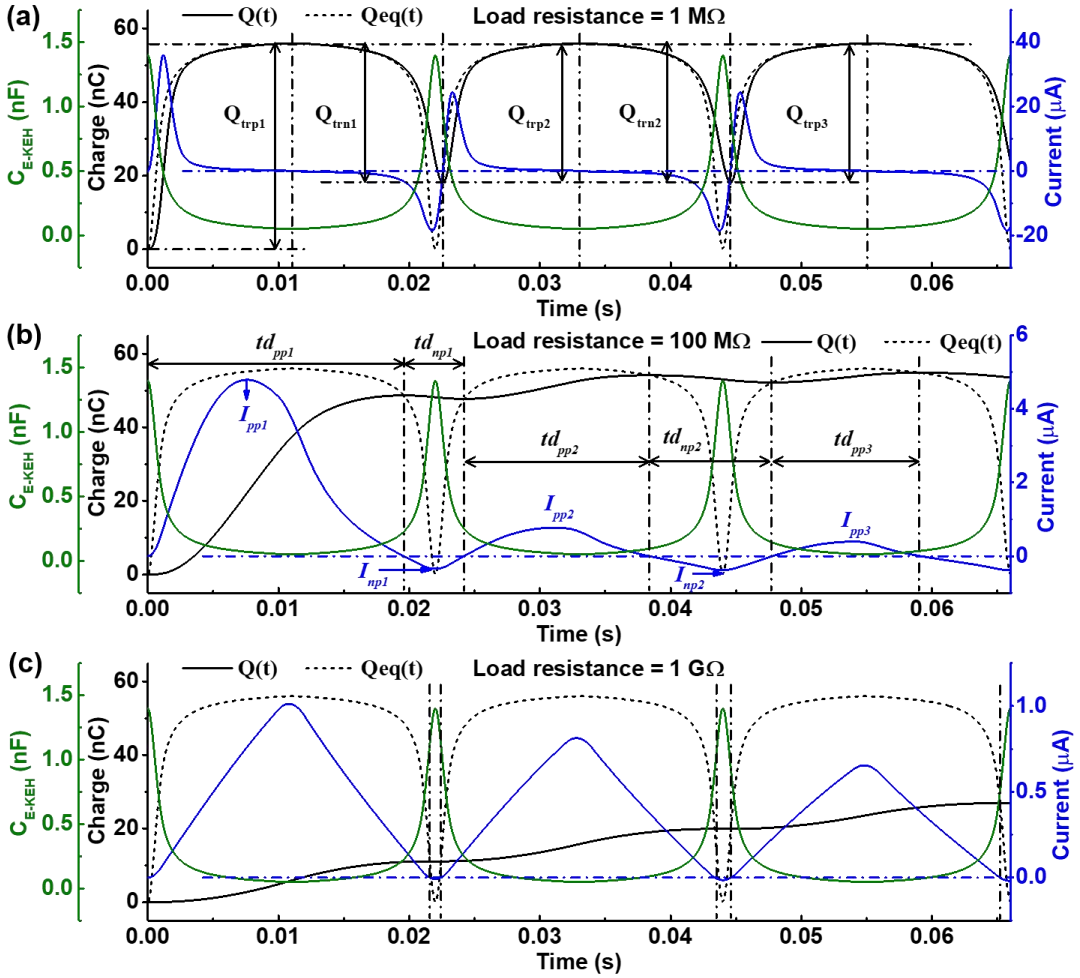

Figure 3-3 Charge-transfer processes of the E-KEH simulated with the load resistances of (a) 1 MΩ, (b) 100 MΩ, and (c) 1 GΩ, using $z(0)=0$ and $Q(0)=0$, in the first three motion cycles.

Firstly, by comparing the $Q(t)$ and the short-circuit equilibrium charge $Q_{eq}(t)$, it can be found that positive charges will transfer to the back electrode when $Q(t)<Q_{eq}(t)$, generating positive current. And when $Q(t)>Q_{eq}(t)$, positive charges will transfer in an opposite direction, generating negative current. The vertical dash-dot lines in Fig. 2(a)~(c) mark the moment when $Q(t)=Q_{eq}(t)$ and meanwhile $I(t)=0$. It can be summarized that the difference between $Q(t)$ and $Q_{eq}(t)$ leads to the charge-transfer between the two electrodes in a direction that can reduce this difference.

Secondly, the first positive current peak (I_{pp1}) has an obviously larger amplitude than other current peaks. For example in **Figure 3-3(a)**, I_{pp1} is ~36 μA, while the first negative current peak (I_{np1}) is ~−18.6 μA, and the second positive current peak (I_{pp2}) is ~24.5 μA. This can be explained by the characteristics of the charging and discharging processes of the RC series circuit. For an RC series circuit, the charge or

discharge time of the capacitor depends on the time constant ($\tau=R\times C$) of the circuit. With a larger τ, the charge or discharge takes a longer time. For instance, in **Figure 3-3(b)**, at t=0, $Q(t)$, $Q_{eq}(t)$, and $|\Delta Q|$ (the difference between $Q(t)$ and $Q_{eq}(t)$) are 0, the $C_{E\text{-}KEH}$ value is at the maximum value C_{max}. Then $C_{E\text{-}KEH}$ decreases but is still high, the $z(t)$-dependent $Q_{eq}(t)$ increases fast but the $Q(t)$ increases slower because of large τ with high $C_{E\text{-}KEH}$, making $|\Delta Q|$ increase. With $C_{E\text{-}KEH}$ further decreasing, τ decreases a lot so that the charge can transfer faster, and $|\Delta Q|$ is gradually reduced to 0 at the time marked by the first vertical dash-dot line. After that, both $Q_{eq}(t)$ and $Q(t)$ decrease but $C_{E\text{-}KEH}$ increases dramatically, resulting in an increasing τ and $|\Delta Q|$. When a whole motion cycle ends, $Q_{eq}(t)$ decreases to 0 but $Q(t)$ is still much larger than 0. Then $Q_{eq}(t)$ starts to increase again in the second movement cycle, τ starts to decrease, meanwhile $Q(t)$ keeps decreasing until the moment that $|\Delta Q|$ becomes 0 again as marked by the second vertical dash-dot line. Then the second charge-transfer cycle begins. The charge-transfer cycle (including an entire positive and an entire negative current peaks) falls behind the movement cycle, resulting in that transferred charge amount in the first positive current peak (Q_{trp1}) is larger than that in the first negative current peak (Q_{trn1}) and in following current peaks (Q_{trp2}, Q_{trn2}, Q_{trp3}…), making the first current peak higher than the others. In Fig. 2(b), I_{pp1} is ~4.8 μA, I_{np1} is ~ −0.35 μA, and I_{pp2} is ~0.77 μA.

At last, in **Figure 3-3(a)**, the positive current peaks have a larger amplitude of ~24.5 μA than that of negative peaks of 18.6 μA in latter charge-transfer cycles even with the same transferred charge amount ($Q_{trp2} = Q_{trn2} = Q_{trp3} =$…). And in **Figure 3-3(b)** and **(c)**, not only the amplitude and the transferred charge amount Q_{trp} of the positive current peaks (I_{pp}) are apparently larger than those of the negative ones (I_{np} and Q_{trn}), but also the time duration of the positive current peak (td_{pp}) is apparently longer than the negative one (td_{np}) in each charge-transfer cycle. Though the movement profile is symmetric in both approaching and separating directions. Moreover, it can be noticed from **Figure 3-3(b)** and **(c)** that I_{pp} and td_{pp} gradually decrease from the first to the third charge-transfer cycle, meanwhile the amplitude of I_{np} and td_{np} gradually increase. This asymmetric output characteristic of the E-KEH is also attributed to the lag between the charge-transfer cycle and the movement cycle. And the asymmetric output characteristic becomes more obvious when R is larger since a larger R leads to larger τ that heavily retards the charge-transfer process.

3.3.3 Amplitude-variable output current/voltage/power

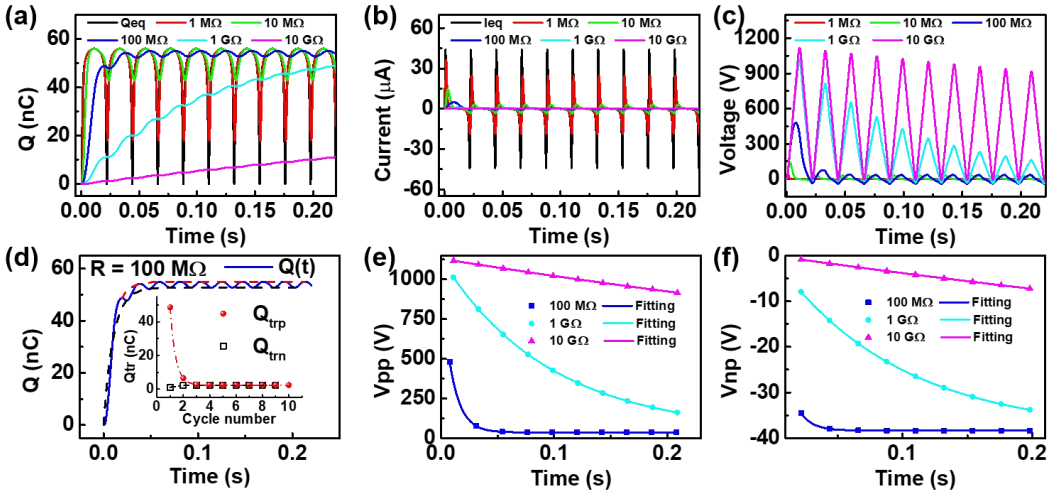

Figure 3-4 Output characteristics of the E-KEH simulated with the different load resistances during the first 10 motion cycles, using the initial condition $z(0)$=0 and $Q(0)$=0. (a) Time-dependent $Q(t)$, (b) $I(t)$, and (c) $V_{E\text{-}KEH}(t)$ of the E-KEH. (d) The variation in the amplitude of $Q(t)$, the inset shows the variation in transferred charge amounts in two directions (Q_{trp} and Q_{trn}). (e) Positive (V_{pp}) and (f) negative (V_{np}) output voltage peak values with fitted curves.

Figure 3-4(a)~(c) shows the simulated $Q_{eq}(t)$, $Q(t)$, $I_{eq}(t)$, $I(t)$, and $V_{E\text{-}KEH}(t)$ of the E-KEH with different load resistances in the first 10 motion cycles, and with the first initial condition i.e. $z(0)$=0 and $Q(0)$=0.

In **Figure 3-4(a)**, all $Q(t)$ simulated with different load resistances show smaller variation range than $Q_{eq}(t)$ in each charge-transfer cycle, and a larger R leads to a smaller variation range, meaning fewer charge is transferred in each cycle due to the larger resistance. With the resistance of 1 MΩ, 10 MΩ, and 100 MΩ, $Q(t)$ is limited in a stable range after three charge-transfer cycles. Taking the charge-transfer process with R of 100 MΩ as an example shown in **Figure 3-4(d)**, the amplitude of $Q(t)$ varies from the first to the third charge-transfer cycles and then is limited between steady upper and lower limiting values marked by the red and black dash lines, respectively. This is because Q_{trp} is larger than Q_{trn} in the first and second charge-transfer cycles and becomes the same with Q_{trn} in the third cycle as shown in the inset of **Figure 3-4(d)**. While with the resistance of 1 GΩ and 10 GΩ, the amplitude of $Q(t)$ keeps a growing trend in 10 motion cycles.

In **Figure 3-4(b)**, larger Resistance leads to a lower amplitude of $I(t)$, which is in accordance with the literature [155, 156]. This makes the current peaks and the

variations in the amplitude of $I(t)$ with larger resistances unobservable in **Figure 3-4(b)**. On the contrary, the amplitude of $V_{E\text{-}KEH}(t)$ is higher with larger Resistance, making the variation in the amplitude of $V_{E\text{-}KEH}(t)$ prominent as shown in **Figure 3-4(c)**. With the resistance of 1 MΩ, 10 MΩ, and 100 MΩ, the positive voltage peak value (V_{pp}) and the negative voltage peak value (V_{np}) vary to steady ranges in three cycles. With the resistance of 1 GΩ and 10 GΩ, V_{pp} shows an apparent decreasing trend during all the ten cycles.

All positive (V_{pp}) and negative (V_{np}) output voltage peak values with resistances of 100 MΩ, 1 GΩ, and 10 GΩ from the first the tenth cycles are plotted in **Figure 3-4(e)** and **(f)** respectively. V_{pp} and V_{np} values vary with time perfectly in accordance with the following equation:

$$Vp(t) = V_s + V_a exp(-(t - t_0)/\tau_d) \qquad (3\text{-}23),$$

where t_0 is the time when the first corresponding voltage peak value (V_{pp1} for V_{pp} values, and V_{np1} for V_{np} values) appears, τ_d is a fitting parameter with the same unit of time, V_s and V_a are two other fitting parameters with the same unit of voltage. These parameter values are given in **Table 3-2**.

Table 3-2 Parameter values in fitting V_{pp} and V_{np} with the first initial condition

Parameter	Load resistance R					
	100 MΩ	1 GΩ	10 GΩ	100 MΩ	1 GΩ	10 GΩ
	Fitting parameters for V_{pp}			Fitting parameters for V_{np}		
V_s (V)	35.65	38.70	38.75	-38.36	-38.69	-38.70
t_0 (s)	7.55×10^{-3}	1.08×10^{-2}	1.10×10^{-2}	2.20×10^{-2}	2.20×10^{-2}	2.20×10^{-2}
V_a (V)	444.00	974.70	1079.00	3.86	30.75	37.82
τ_d (s)	9.87×10^{-3}	9.57×10^{-2}	9.57×10^{-1}	9.57×10^{-3}	9.57×10^{-2}	9.57×10^{-1}

All adjusted coefficients of determination of these fittings are 1, indicating perfect fittings. Standard errors of these parameters in fitting are given in **Table 3-3**.

Table 3-3 Standard errors (SE) of the corresponding parameters in Table 3-2

Parameter	SE of fitting parameters for V_{pp}			SE of fitting parameters for V_{np}		
	100 MΩ	1 GΩ	10 GΩ	100 MΩ	1 GΩ	10 GΩ
V_s (V)	3.70×10^{-3}	4.95×10^{-2}	2.89×10^{-1}	1.21×10^{-7}	8.87×10^{-7}	5.84×10^{-6}
t_0 (s)	0	0	0	0	0	0
V_a (V)	1.08×10^{-2}	4.49×10^{-2}	2.88×10^{-1}	3.32×10^{-7}	8.02×10^{-7}	5.82×10^{-6}
τ_d (s)	1.09×10^{-6}	1.15×10^{-5}	2.84×10^{-4}	3.57×10^{-9}	6.02×10^{-9}	1.62×10^{-7}

The time-dependent part in the equation (3-23) has the same exponential form as the discharging curve equation of a resistor-capacitor (RC) circuit. In analogy with the RC circuit discharging process, we define the parameter τ_d as the time constant of this variation. From **Table 3-2**, τ_d is almost directly proportional to the resistance value R especially for the large R of 1 GΩ and 10 GΩ, meaning that it takes a longer time for the E-KEH to give steady output with larger R than with smaller R.

From the equation (3-23), it can be inferred that the V_{pp} or V_{pp} value will gradually approach the corresponding V_s value when the time is long enough. By using the equation (3-23) and parameter values in **Table 3-2**, V_{pp} and V_{np} values in 6 seconds were fitted and shown in **Figure 3-5(a)**. Though the first V_{pp} and V_{np} values with 100 MΩ, 1 GΩ, and 10 GΩ are so different as shown in **Figure 3-4(e)** and **(f)**, after 6 seconds, their difference becomes very small since the V_s values with 100 MΩ, 1 GΩ, and 10 GΩ are very close, as given in **Table 3-2**. The parameter V_a determines the difference between the V_{pp1} or V_{np1} and the corresponding V_s, which reveals the rangeability of V_{pp} or V_{np}. In **Table 3-2**, V_a is larger with larger resistance for both V_{pp} and V_{np}, meaning that the rangeability of V_{pp} or V_{np} is larger with larger Resistance as can be seen from **Figure 3-5 (a)**.

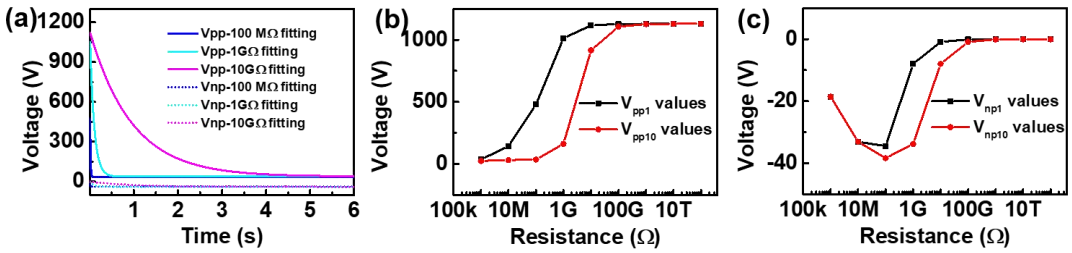

Figure 3-5 (a) Fitted variation trend of V_{pp} and V_{np} in 6s. (b) V_{pp1} and V_{pp10} values with different load resistances. (c) V_{np1} and V_{np10} values with different load resistances.

Simulated V_{pp1}, V_{pp10}, V_{np1}, and V_{np10} with different resistances are shown in **Figure 3-5 (b)** and **(c)**. Both V_{pp1} and V_{pp10} increase with R and saturate at a value of ~1130 V when R is high enough, while the absolute values of V_{np1}, and V_{np10} increase with R from 1 MΩ to 100 MΩ and then decrease with increasing R.

Figure 3-6(a) shows the simulated instantaneous output power $P(t)$ of the E-KEH with different load resistances in the first 10 motion cycles.

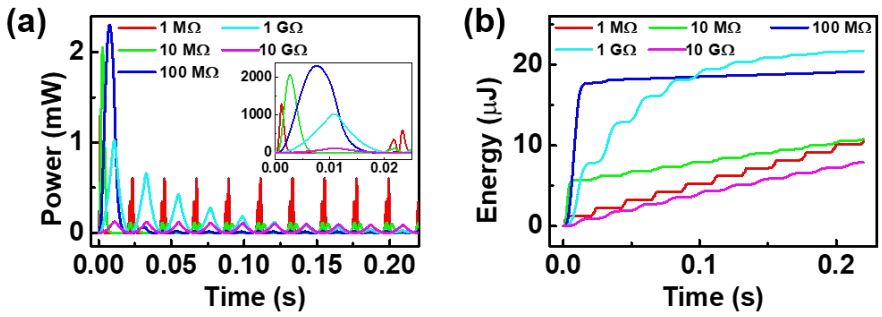

Figure 3- 6 Simulated output power and energy of the E-KEH with different load resistances during the first 10 motion cycles, using the first initial condition *z(0)*=0 and *Q(0)*=0. (a) The instantaneous output power of the E-KEH. (b) The accumulated output energy of the E-KEH.

In the first movement cycle, the peak *P(t)* increases from ~1.29 mW to ~2.30 mW if *R* increases from 1 MΩ to 100 MΩ, then decreases to ~0.125 mW if *R* further increases to 10 GΩ. However, in the followed motion cycles, *P(t)* peak values are much lower than those in the first cycle, especially for *P(t)* with *R* of 10 MΩ and 100 MΩ. This can also be noticed in **Figure 3- 6(b)** that presents the accumulated output energy *W(t)* of the E-KEH to different load resistance based on the following equation:

$$W(t) = \int_0^t P(t)dt \qquad (3\text{-}24).$$

Though the output energy with *R* of 100 MΩ after the first motion cycle is much higher than those with other resistances, in the followed cycles little energy is output with *R* of 100 MΩ and the total energy is overpassed by that with *R* of 1 GΩ after several cycles. The average output power (*AvgP*) of the E-KEH in each motion cycle can be calculated by:

$$AvgP(c) = \frac{\int_{(c-1)*T}^{c*T} P(t)dt}{T} \qquad (3\text{-}25)$$

where c is the motion cycle number and *T* is the period of one movement cycle.

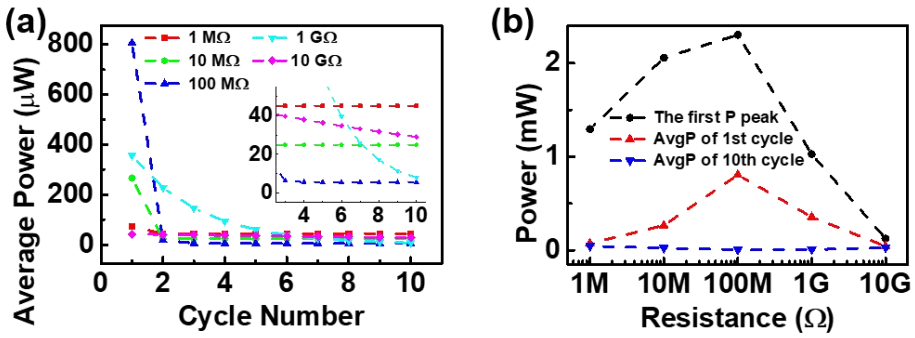

Figure 3-7 (a) Average output power per motion cycle (*AvgP*) of the E-KEH. (b) The first P(t) peak value, and the *AvgP* in the first and tenth motion cycles of the E-KEH with different load resistances.

As shown in **Figure 3-7(a)**, in the first cycle, the E-KEH outputs the highest average power of ~806 μW with R of 100 MΩ. But at the tenth cycle, the *AvgP(10)* with R of 1 MΩ is the highest as ~45 μW, and the *AvgP(10)* with R of 100 MΩ becomes the lowest as ~5.6 μW. The first *P(t)* peak values and *AvgP* values at the first and the tenth cycles with different load resistances are plotted in **Figure 3-7(b)** for better comparison.

3.3.4 Simulations with another initial condition

Then the case $z(0) = z_{max}$ i.e. the initial condition $Q(0) = Q_{max}$ was considered (will be called the second initial condition for convenience), using the same parameter values in **Table 3-1**. The *z(t)* and *v(t)* profiles are shifted half period from the case $z(0) = 0$, as plotted in **Figure 3-8**.

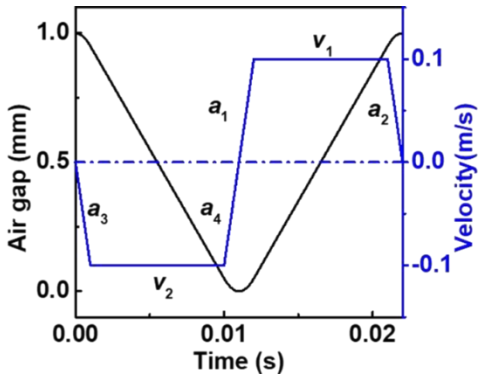

Figure 3-8 Simulated *z(t)* and *v(t)* curves in the first motion cycle with $z(0) = z_{max}$.

For this initial condition, **Figure 3-9(a)~(c)** shows corresponding simulated charge-transfer processes of the E-KEH in the first three motion cycles with load resistances of 1 MΩ, 100 MΩ, and 1 GΩ, respectively.

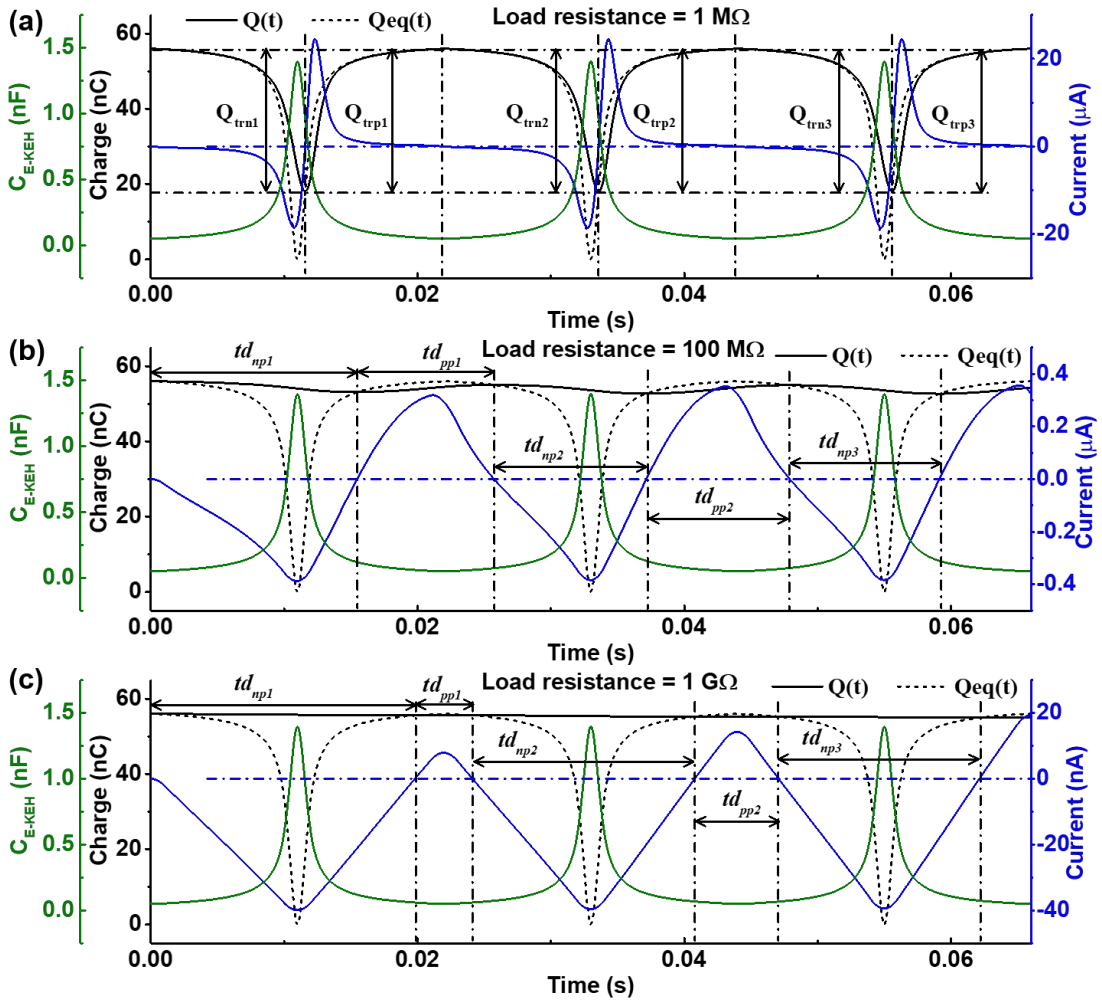

Figure 3-9 Simulated charge-transfer processes of the E-KEH with load resistances of (a) 1 MΩ, (b) 100 MΩ, and (c) 1 GΩ, using the second initial condition ($z(0) = z_{max}$ and $Q(0) = Q_{max}$), in the first three motion cycles.

The first current peak is negative due to the moving direction is opposite to that in **Figure 3-3**, and the amplitude of the first current peak (I_{np1}) shows a smaller difference with other current peaks than that in **Figure 3-3**. For instance, in **Figure 3-9(a)**, all negative current peak values are almost the same as about -18.6 μA, and all positive current peak values are almost the same as about 24.5 μA. Moreover, in **Figure 3-9(b)** and **(c)**, the amplitude of I_{np} is higher than that of I_{pp}, but their difference is also smaller than that in **Figure 3-3(b)** and **(c)**. This is also due to variations of $C_{E\text{-}KEH}$ and $|\Delta Q|$. For instance, in **Figure 3-9(b)**, in the time duration of the first negative current peak (td_{np1}), both the maximum $|\Delta Q|$ and $C_{E\text{-}KEH}$ are much larger than those in the time duration of the first positive current peak (td_{pp1}). So even though the transferred charge amount in the time duration of td_{np1} is larger, it takes a

longer time to complete the charge-transfer than that in the time duration of td_{pp1}, which contributes to making the difference between the amplitude of I_{np} and I_{pp} less than that in **Figure 3-3**. In addition, it can be noticed from **Figure 3-9(b)** and **(c)** that the amplitude of I_{np} and td_{np} gradually decrease from the first to the third charge-transfer cycle, meanwhile I_{pp} and td_{pp} gradually increase.

Figure 3-10(a)~(c) shows the simulated $Q(t)$, $I(t)$ and $V_{E\text{-}KEH}(t)$ of the E-KEH with different load resistances in the first 10 motion cycles using the second initial condition. Variations in the amplitude of $Q(t)$ and $I(t)$ with large R are not easy to observe in **Figure 3-10(a)** and **(b)**, but the variation in the amplitude of $V_{E\text{-}KEH}(t)$ can be clearly noticed in **Figure 3-10(c)**. In comparison with **Figure 3-4(c)**, it's similar that the amplitude of $V_{E\text{-}KEH}(t)$ varies at first and then goes to near-stable ranges in three cycles with R of 1 MΩ, 10 MΩ, and 100 MΩ, and it keeps varying even after ten cycles with larger R of 1 GΩ and 10 GΩ.

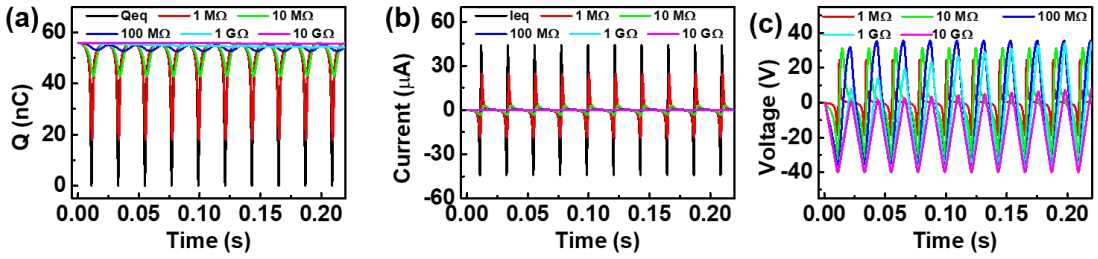

Figure 3-10 Simulated output characteristics of the E-KEH with different load resistances during the first 10 motion cycles, using the second initial condition ($z(0) = z_{max}$ and $Q(0) = Q_{max}$). (a) $Q(t)$, (b) $I(t)$, and (c) $V_{E\text{-}KEH}(t)$ of the E-KEH with different load resistances.

The V_{pp} and V_{np} values also vary with time perfectly in accordance with the equation (3-23). The parameter values in fitting V_{pp} and V_{pp} in **Figure 3-10(c)** are given in **Table 3-4**, with corresponding Standard errors given in **Table 3-5**.

Table 3-4 Parameter values used in fitting V_{pp} and V_{np} with the second initial condition ($z(0) = z_{max}$ and $Q(0) = Q_{max}$).

Parameter	Load resistance R					
	100 MΩ	1 GΩ	10 GΩ	100 MΩ	1 GΩ	10 GΩ
	Fitting parameters for V_{pp}			Fitting parameters for V_{np}		
V_s (V)	35.66	38.66	38.71	-38.36	-38.69	-38.70
t_0 (s)	2.1×10^{-2}	2.2×10^{-2}	2.2×10^{-2}	1.1×10^{-2}	1.1×10^{-2}	1.1×10^{-2}
V_a (V)	-3.743	-30.73	-37.83	-0.3658	-1.221	-1.357
τ_d (s)	9.56×10^{-3}	9.57×10^{-2}	9.58×10^{-1}	9.55×10^{-3}	9.57×10^{-2}	9.57×10^{-1}

Table 3-5 Standard errors (SE) of the corresponding parameters in Table 3-4

Parameters	SE of fitting parameters for V_{pp}			SE of fitting parameters for V_{np}		
	100 MΩ	1 GΩ	10 GΩ	100 MΩ	1 GΩ	10 GΩ
V_s (V)	2.42×10^{-5}	5.99×10^{-4}	0.01029	6.90×10^{-6}	1.24×10^{-5}	5.52×10^{-5}
t_0 (s)	0	0	0	0	0	0
V_a (V)	7.06×10^{-5}	5.44×10^{-4}	1.03×10^{-2}	2.02×10^{-5}	1.12×10^{-5}	5.51×10^{-5}
τ_d (s)	7.80×10^{-7}	4.40×10^{-6}	2.85×10^{-4}	2.29×10^{-6}	2.29×10^{-6}	4.32×10^{-5}

V_s values in **Table 3-4** are almost the same as those in **Table 3-2**, meaning that stable peak values of $V_{E\text{-}KEH}(t)$ with these two different initial conditions will finally be the same. V_a values in **Table 3-4** are all negative, meaning that the amplitude of the positive voltage peaks ($|V_{pp}|$) gradually increases but that of negative voltage peak ($|V_{np}|$) decreases with the cycle number. Each $|V_a|$ is smaller than the corresponding one in **Table 3-2**, reflecting the fact that variation ranges of $V_{E\text{-}KEH}(t)$ in **Figure 3-10(c)** are smaller than those in **Figure 3-4(c)** with the same R. And the time constant τ_d values in **Table 3-4** are almost the same with those corresponding in **Table 3-2**.

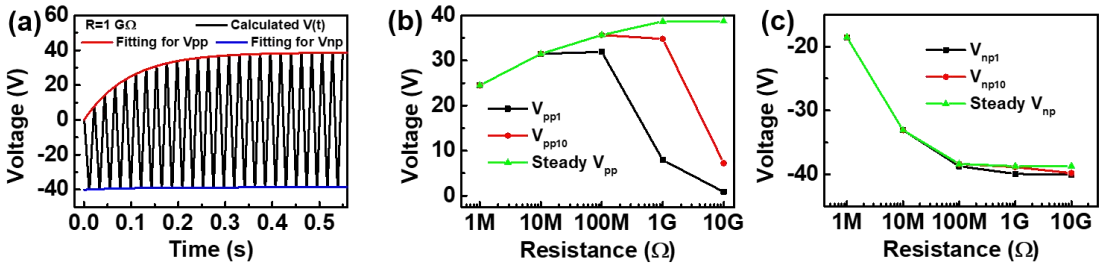

Figure 3-11 (a) $V_{E\text{-}KEH}(t)$ of the E-KEH with the load resistance of 1GΩ during 25 motion cycles, with the variation trend of the amplitude of $V_{E\text{-}KEH}(t)$ marked by fitting curves. (e) Positive (V_{pp}) and (f) negative (V_{np}) voltage peak values of the E-KEH with different load resistances in the first and tenth motion cycles and their final steady-state values.

Figure 3-11(a) shows $V_{E\text{-}KEH}(t)$ in the first 25 motion cycles of the E-KEH with R of 1 GΩ as an example. The amplitude of positive voltage peaks shows an apparent increasing trend and then approaches a steady value, while the amplitude of negative voltage peaks slightly decreases and then approaches to a steady value. And the variation of $V_{E\text{-}KEH}(t)$ is limited between the fitting lines for V_{pp} and V_{np} using the values of parameters given in **Table 3-4**.

The $V_{E\text{-}KEH}(t)$ peak values with this initial condition and with different load resistances are plotted in **Figure 3-11(b)** and **(c)**. For positive voltage peaks, both the

V_{pp1} and V_{pp10} firstly increase with R from 1 MΩ to 100 MΩ, and then decrease with larger R. Nevertheless, the final steady V_{pp} value shows a monotone increasing trend with R. For the negative voltage peaks, all the amplitude of V_{np1}, V_{np10} and steady V_{np} values monotonically increase with R from 1 MΩ to 10 GΩ. To be more explicit, the steady V_{pp} and V_{np} values with R of 100 MΩ, 1 GΩ, and 10 GΩ are the corresponding V_s values in **Table 3-4**.

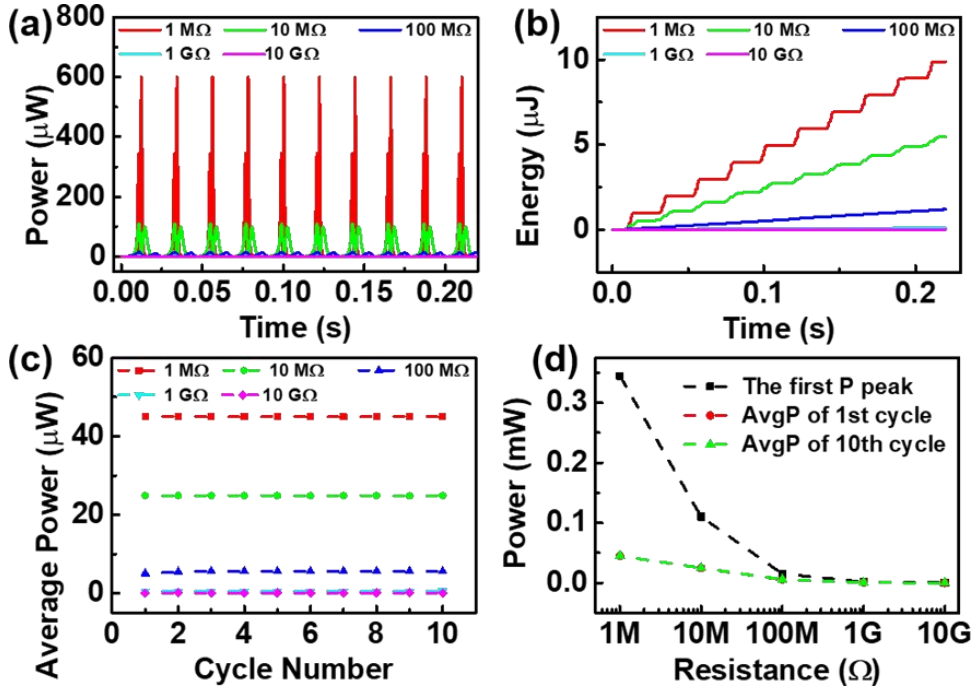

Figure 3-12 Simulated output power and accumulated output energy of the E-KEH with different load resistances during the first 10 motion cycles, using the second initial condition. (a) Instantaneous output power (*P(t)*), (b) the accumulated output energy (*W(t)*), and (c) average output power per motion cycle (*AvgP(c)*) of the E-KEH. (d) The first *P(t)* peak value, and the *AvgP* of the E-KEH in the first and tenth motion cycles with different load resistances.

Figure 3-12(a)~(c) presents the output power, accumulated output energy, and average power per motion cycle of the E-KEH in the first 10 motion cycles, using the second initial condition. The influences of R on the output power and average power is shown in **Figure 3-12(d)**. In all motion cycles, smaller R leads to both higher peak power and average power, which is quite different from the result shown in **Figure 3-6** and **Figure 3-7**. The peak values of the *P(t)* and the *AvgP* in the first motion cycle with different R are lower than those in **Figure 3-7(b)**. More similarities and differences in the simulated output energy and power of the E-KEH from these two initial conditions are discussed in section 3.3.5.

3.3.5 QV cycle analysis

The output energy of the E-KEH can be explicitly evaluated from the charge-voltage (QV) diagram. The area of the QV loop equals the output energy of the E-KEH per charge-transfer cycle [27, 158].

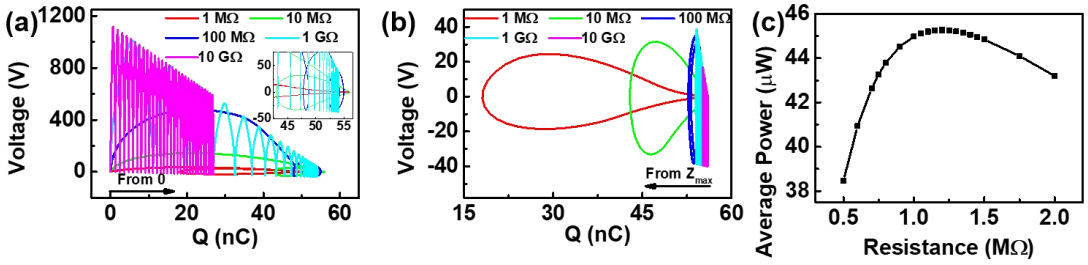

Figure 3-13 QV diagrams of the E-KEH simulated with (a) the first initial condition ($z(0)$=0 and $Q(0)$=0) and (b) the second initial condition ($z(0)$= z_{max} and $Q(0)$=Q_{max}), with different load resistances. (c) The influence of the load resistance on the output average power per motion cycle of the E-KEH simulated with the second initial condition.

Figure 3-13(a) and **(b)** show the QV diagrams of the E-KEH during no less than 10 motion cycles simulated with the first and the second initial conditions respectively. In **Figure 3-13(a)**, with relatively small R as 1 MΩ, 10 MΩ, and 100 MΩ, the QV curve shows a large span arc-shaped line in the first charge-transfer cycle and then becomes a closed-loop after less than 3 motion cycles, while for the results with large R as 1 GΩ, and 10 GΩ, the QV curve keeps unclosed with a damped variation trend in simulated 30 motion cycles. In **Figure 3-13(b)**, with *R* of 1 MΩ, 10 MΩ, and 100 MΩ, there is no arch-shaped line and the QV line becomes a closed teardrop-shaped loop after less than 3 motion cycles, which is typical for E-KEH with the continuous conditioning circuit [27, 35], while with larger R as 1 GΩ, and 10 GΩ, the QV line keeps unclosed with a growing variation trend in simulated 25 motion cycles. The area of the closed QV cycle with *R* of 1 MΩ in **Figure 3-13(b)** is the largest as ~ 0.99 μJ per cycle, which is also in accordance with **Figure 3-12(b)~(d)**. To get the more accurate optimum load resistance (R_{opt}) for the E-KEH to output the maximum steady *AvgP*, the *AvgP* in the third motion cycle of the E-KEH with *R* from 0.5 MΩ to 2 MΩ were calculated with the second initial condition and shown in **Figure 3-13(c)**. The *AvgP* increases and then decreases with increasing *R* and gets the maximum value of ~45.27 μW with *R* of 1.2 MΩ among all the calculated data.

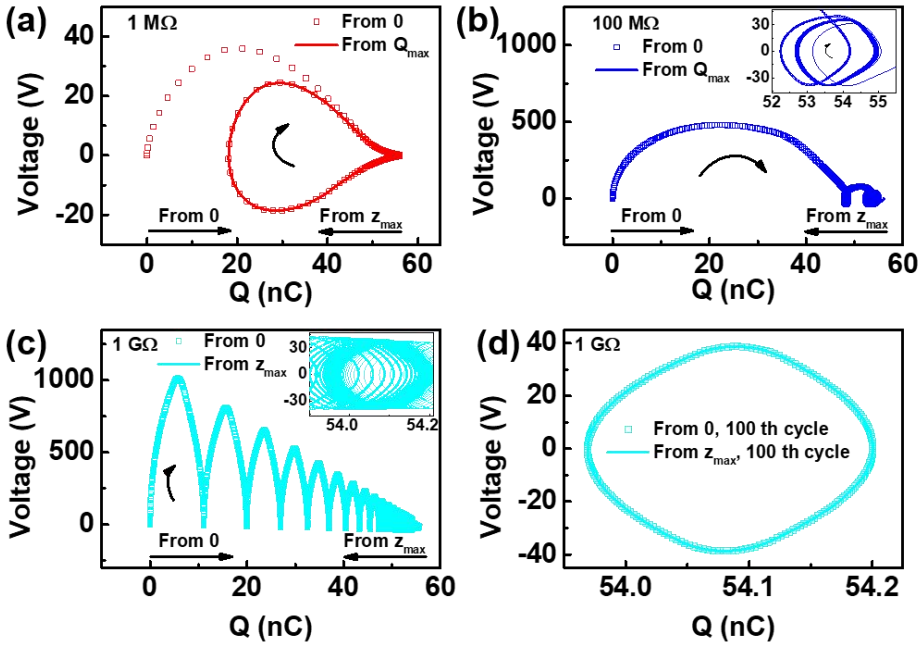

Figure 3-14 Simulated QV diagrams of the E-KEH with the first and second initial conditions, with load resistances of (a) 1 MΩ, (b) 100 MΩ, and (c) 1 GΩ, respectively. (d) The overlapped QV cycle with 1 GΩ load resistance at the 100th working cycle of the E-KEH that starts working from the first (from 0) and the second (from z_{max}) initial conditions respectively.

For a better comparison, the simulated QV diagrams with these two different initial conditions with R of 1 MΩ, 100 MΩ, and 1 GΩ were plotted in **Figure 3-14(a)~(c)** respectively. **Figure 3-14(a)** and **(b)** present the results of the first 10 motion cycles from the first initial condition (from 0) and from the second initial condition (from z_{max}). The QV cycles from the two different initial conditions become overlapped after the first cycle with R of 1 MΩ, and it takes about three cycles for those with R of 100 MΩ to become fully overlapped. In **Figure 3-14(c)** with the data of the first 100 motion cycles from the first and second initial conditions. **Figure 3-14(d)** clearly shows that the 100th QV cycles of the E-KEH with R of 1 GΩ starting from these two initial conditions overlap with each other.

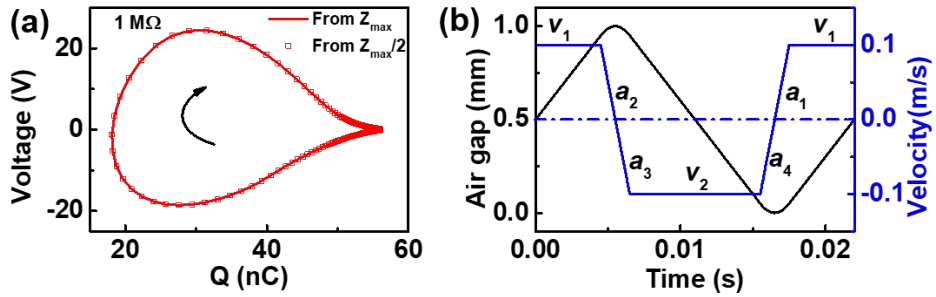

Figure 3-15 (a) Overlapped QV cycles of the E-KEH starts working from $z(0)=z_{max}$ and from $z(0)=z_{max}/2$, with R of 1 MΩ and $Q(0)=Q_{eq}(0)$. (b) $z(t)$ and $v(t)$ profiles using the initial condition $z(0)=z_{max}/2$, and $v(0)=v_1$.

In addition, **Figure 3-15(a)** indicates that the E-KEH with R of 1 MΩ also outputs the same QV diagram using another initial condition $z(0) = z_{max}/2$ and $Q(0) = Q_{eq}(0)$. It can be inferred that the QV cycle of an E-KEH with a given R and driven by a specific steady periodic motion cycle will finally become a specific steady closed loop after long enough time. And it takes a longer time for the E-KEH to output the steady QV cycle with a larger R than with smaller R.

3.4 Experimental and simulation verifications

3.4.1 Experimental Methods

To verify the simulated amplitude-variable characteristics, a TE-KEH with a piece of ~4 cm × 4 cm rectangular 100 μm-thick skived PTFE film as the electret layer was made and tested. The PTFE film was cleaned by deionized water and ethanol using an ultrasonic cleaner at first. After fully dried, a piece of conductive and adhesive copper tape (3M, type 1181) was pasted on one side of the PTFE film to form the back electrode. Then the PTFE film with the back electrode was attached to the sliding block of a linear motor (Afag Electro slide ES20-100 with LinMot servo drive) by double-sided adhesive tapes, and a piece of Al foil was attached to a fixed plate faced with the PTFE film as shown in **Figure 3-16(a)**.

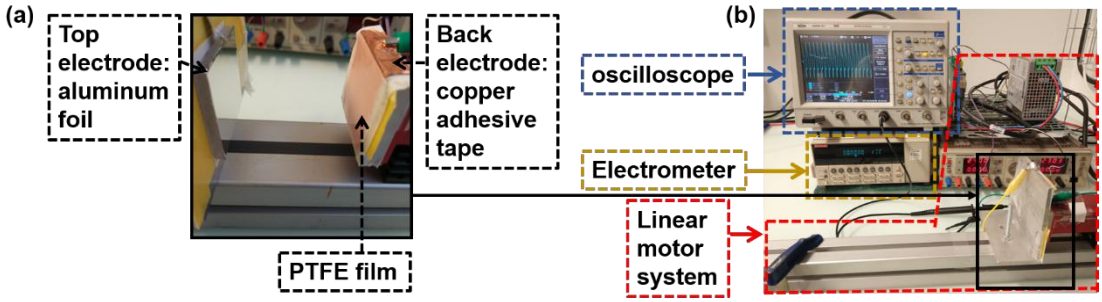

Figure 3-16 (a) Photograph of the PTFE film-based TE-KEH mounted on the sliding rail of the linear motor. (b) Photograph of the linear motor system together with electrical measuring equipment.

During the tests, the sliding block of the linear motor was set to move forward and backward as the driving motion to make the PTFE film contact with and separate from the Al foil cyclically. It is noteworthy that the PTFE film was not pre-charged before tests, the electrostatic charges on the PTFE film were obtained probably by the tribo-charging effect during the fabrication process or during tests, therefore this E-KEH is called as TE-KEH. To measure the output voltage of the TE-KEH, the back and top electrodes were connected to an oscilloscope (Wavejet 354A, Lecroy) through a high impedance probe with an input impedance of 100 MΩ as shown in **Figure 3-16(b)**. The short-circuit transferred charge amount was recorded with a Keithley 6514 electrometer by directly connecting the two electrodes of the TE-KEH with the two input terminals of the electrometer. In all electrical measurements, the top electrode was connected to the positive terminal.

Motion parameters (z_{max}, v_1, v_2, a_1, a_2, a_3, and a_4) of the sliding block of the linear motor were set in the control software (LinMot-Talk 6.0) as values listed in **Table 3-1**. However, the recorded values of these parameters by the software were different from set values. **Figure 3-17(a)** and **(b)** show $z(t)$ and $v(t)$ data recorded by the control software of the linear motor. These differences may be caused by the uncontrollable impact or vibrations, or the neglected deformations of the components and substrates of the TE-KEH during movements of the sliding block in such a short distance and with high acceleration/deceleration.

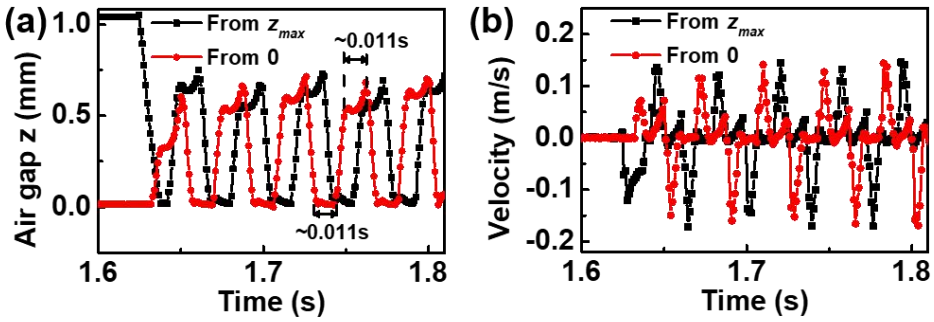

Figure 3-17 (a) *z(t)* and (b) *v(t)* data recorded by the linear motor system during the measurement of the TE-KEH starts working from $z(0)=z_{max}$ *and* $z(0)=0$ respectively.

3.4.2 Estimations of parameter values for corresponding simulations

To do corresponding simulations with the experiments, the effective motion parameter values and the charge density need to be redetermined. From the data in **Figure 3-17(a)** and **(b)**, the actual z_{max} was estimated at 0.7 mm, v_1 and v_2 were estimated at 0.14 m/s and -0.17 m/s respectively. The acceleration and deceleration of the slider block were estimated according to the linear fitting results of the *v(t)* data as shown in **Figure 3-18** and **Figure 3-19**.

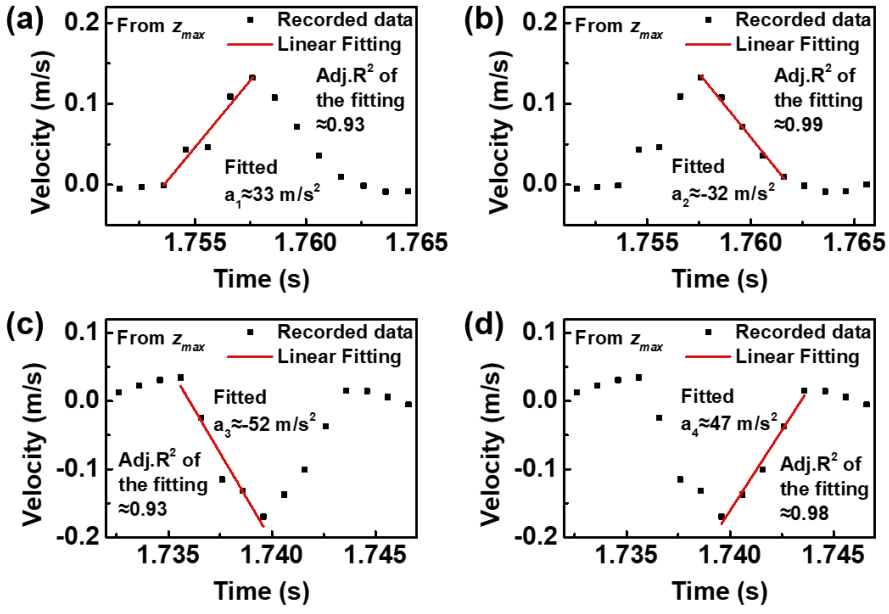

Figure 3-18 Recorded *v(t)* data with linear fitting for (a) a_1, (b) a_2, (c) a_3, and (d) a_4 with the motion starting from the fully-separated position.

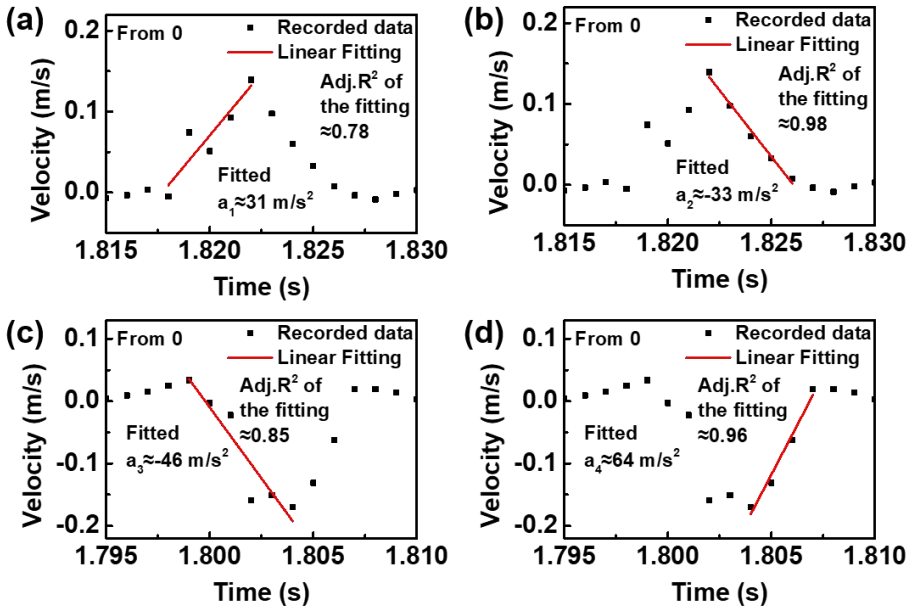

Figure 3-19 Recorded *v(t)* data with linear fitting for (a) a_1, (b) a_2, (c) a_3, and (d) a_4 with the motion starting from the contact position.

It can also be noticed from **Figure 3-17(a)** and **(b)** that the slider block kept almost still for ~0.011s when it moved to the position of z=0, and it moved at a rather low velocity for ~0.011s when it got close to the position of z=0.7 mm. To simplify the simulation, the movement velocity during these two durations of 0.011 s was set as 0, and these two durations were called as the wait time t_{w1} and t_{w2}.

To estimate the charge density on the PTFE film, the transfer charge amount of the TE-KEH was measured, with setting the z_{max} as 10 mm and the wait time as 5 s at both limiting positions of z=0 and z=z_{max}. With such a large z_{max} and wait time, it's reasonable to assume that the maximum short-circuit transferred charge amount approximates to the charge amount on the PTFE film [90, 91]. From the results shown in **Figure 3-20**, the polarity of charges on the PTFE film was confirmed to be negative since positive charges were transferred from the top electrode to the back electrode during the gap enlarging process, and in the opposite direction during the gap closing process. And the effective surface charge density on the PTFE film was estimated to be -50 μC/m^2 according to the measured maximum transferred charge amount of ~80 nC for the PTFE film with the area of ~16 cm^2.

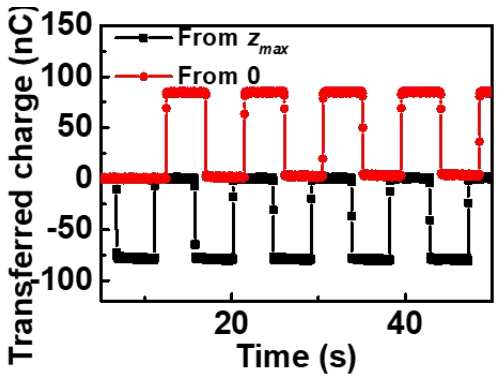

Figure 3-20 The measured short-circuit transferred charge amount data of the TE-KEH that starts working from the two different positions.

All the parameter values for corresponding simulations are listed in **Table 3-6.** The corresponding simulated $z(t)$, $v(t)$, and $C_{TE\text{-}KEH}(t)$ curves are shown in **Figure 3-21**.

Table 3-6 Parameter values in simulating the output of TE-KEH corresponding to the experimental verification.

Parameter	Value
Area of electret film S	16 cm^2
The dielectric constant of the electret film ε_r	2.1
The thickness of the electret film d_f	100 μm
Effective surface charge density on the electret film σ	-50 $\mu C/m^2$
Maximum gap z_{max}	0.7 mm
Acceleration a_1	33 m/s^2
Maximum speed v_1	0.14 m/s
Deceleration a_2	-33 m/s^2
Wait time t_{w1}	0.11 s
Deceleration a_3	-50 m/s^2
Maximum speed v_2	-0.17 m/s
Acceleration a_4	50 m/s^2
Wait time t_{w2}	0.11 s

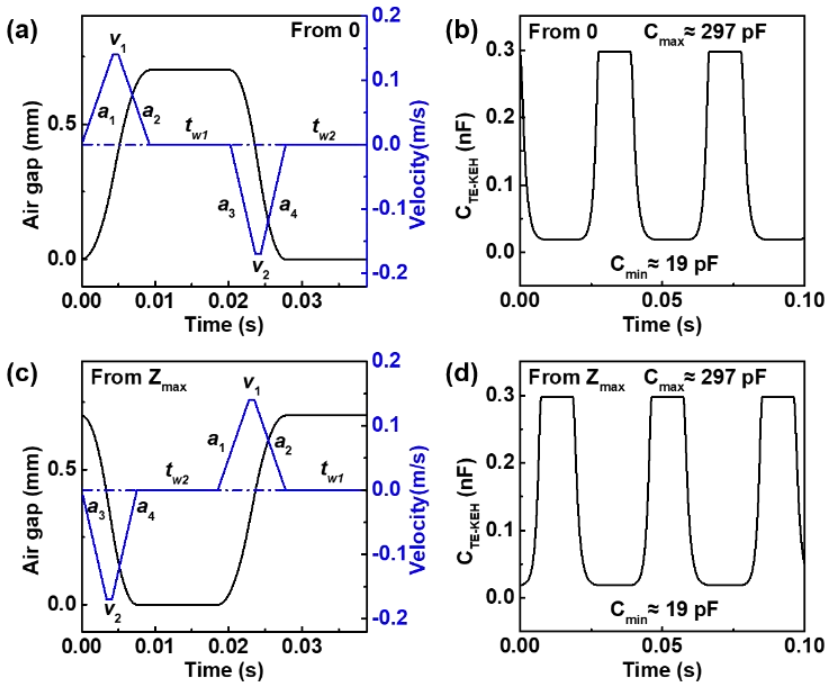

Figure 3-21 (a) Simulated *z(t)*, *v(t)*, and (b) $C_{TE\text{-}KEH}$ *(t)* curves using parameter values in Table 3-6 and the initial condition that *z(0)*=0 and *Q(0)*=0. (c) Simulated *z(t)*, *v(t)*, and (d) $C_{TE\text{-}KEH}$ *(t)* data using parameter values listed in Table 4 and the initial condition *z(0)*= z_{max}.

3.4.3 Results and discussion

The measured output voltages of the TE-KEH with the load resistance of 10 MΩ, 100 MΩ, and 1.1 GΩ are plotted in **Figure 3-22(a)~(c)**. And the simulated output voltages of the TE-KEH with corresponding load resistances are presented in **Figure 3-22(d)~(f)**. With *R* of 10 MΩ, both the simulated and measured output voltages have no apparent variation in the peak amplitude for both initial conditions. With *R* of 100 MΩ, the first positive voltage peak (V_{pp1}) of both the simulated and measured data using the first initial condition ($z(0) = 0$) has a much larger amplitude than other voltage peaks. And with *R* of 1.1 GΩ, apparent variations in the amplitude of voltage peaks appear both in the experimental and simulated data during several motion cycles, especially for the result using the first initial condition, and then the amplitude of voltage peaks becomes almost the same for both initial conditions. These results confirm the presence of variations in the amplitude of output voltages of the TE-KEH with large load resistances and reveal the influence of the initial condition and the load resistance on the amplitude-variable output voltage of the TE-KEH.

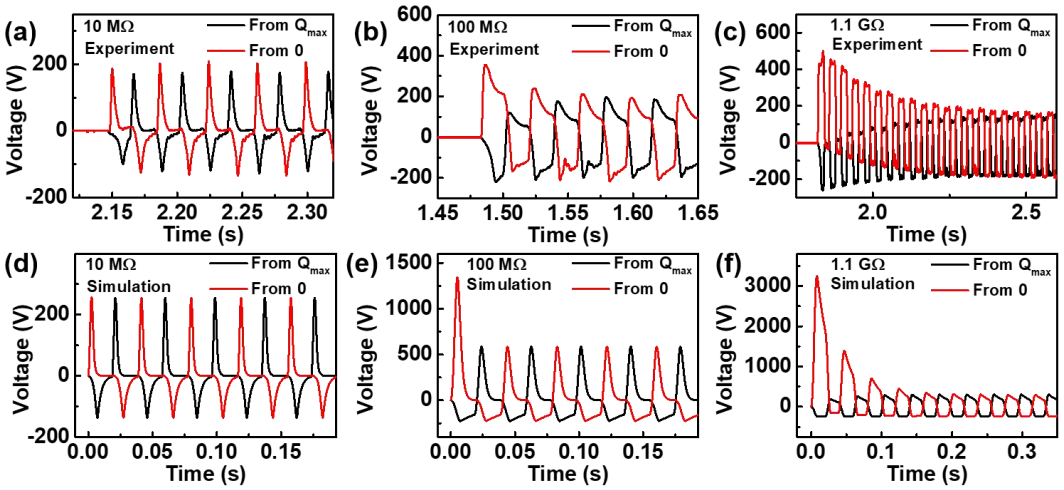

Figure 3- 22 (a), (b), and (c) Measured output voltage of the TE-KEH with load resistances of 10 MΩ, 100 MΩ, and 1.1 GΩ respectively. (d), (e), and (f) Simulated output voltage of the TE-KEH with load resistances of 10 MΩ, 100 MΩ, and 1.1 GΩ respectively.

Though the variation trends of the measured and simulated voltage are similar, however, the voltage peak values in simulated results are much larger than those in measured values, especially with high R of 100 MΩ and 1 GΩ. The difference between the actual and simulated relative motion profiles could be one reason for this difference, other possible reasons will be discussed in section 4.4 in Chapter 4.

3.5 Chapter conclusion

In this chapter, at first, the analytical solution of the CS mode E-KEH with a resistive load was given based on the detailed equivalent electrical model. Then symbolic computations in MATLAB were used to calculate the charge-transfer process and output current/voltage/power of an E-KEH driven by a piecewise periodic reciprocating movement with acceleration/deceleration processes, with different load resistances.

It was found that the amplitudes of the output voltage/current of the E-KEH varied over time in an exponential form and finally got to steady ranges, which was caused by the lag between the charge-transfer cycle and the driving motion cycle. This lag also led to the asymmetric between the output positive and negative current/voltage peaks. And the time for the E-KEH to get steady output is positively correlated to the load resistance.

It was also found, with the first initial condition that the E-KEH started working from the contact position, the variation range of the output voltage peaks was much larger than that the E-KEH started working from the fully-separated position (the second initial condition) with the same load resistance, and the optimum load resistance in latter motion cycles could be very different from that in the first cycle. By comparing QV diagrams of the E-KEH simulated from the two initial conditions, it was found that the E-KEH would finally output the same steady QV cycle with the same load resistance after long enough time if the periodic driving motion was kept the same.

At last, the influences of the load resistance and the initial condition on the amplitude-variable output voltage of a TE-KEH made with PTFE film were confirmed by both experiments and simulations.

Chapter 4 Optimizing the output power of the contact-separation mode TE-KEH

4.1 Introduction

It has been demonstrated that if the time constant of the RC circuit formed by E-KEHs with load resistance is too large, the charge-transfer cycle may fall behind the periodic motion cycle a lot, resulting in the incomplete charge-transfer and consequently dramatical decay in the output power of E-KEHs during continuous multiple working cycles. It's clear that the maximum time constant is obtained when the capacitance of E-KEHs is maximum, which corresponding to the contact state (air gap is 0) for the CS mode E-KEHs. Therefore, prolonging the contact time (wait time at the contact state) could possibly help to complete the charge-transfer process and improve the output power and efficiency of contact-separation (CS) mode E-KEHs with large load resistances.

In this chapter, at first, the strategy of improving the output power and efficiency of a CS mode TE-KEH by the optimization of the contact time is verified by both experimental and simulation results. The theoretical maximum output energy per working cycle of the TE-KEH is deduced. Then several usually unfavorable factors that would reduce the effective output energy per working cycle of the TE-KEH are discussed. At last, the tribo-charging method and the optimization of the maximum air gap are also used to further improve the output power of the TE-KEH.

4.2 Optimization of the contact time

4.2.1 Experimental results

The TE-KEH was made with a 4 cm × 4 cm sized 55 μm-thick PTFE film, with conductive copper tape (3M 1181-50.8) as the back electrode and aluminum foil as the top electrode. The structure of the TE-KEH and the measurement equipment are the same as those introduced in section 3.4.1. The output voltages of a TE-KEH driven by periodical linear motions with the same maximum air gap, same motion velocity, and same acceleration/deceleration profiles but different contact times were measured. All measurements were started from the contact state ($z(0)=0$), and the top

and back electrodes were short-circuited before each measurement to ensure the initial electrostatic equilibrium.

The recorded time-dependent air gap *z(t)* and relative motion velocity *v(t)* between the top electrode and the PTFE film are shown in **Figure 4-1.** The maximum air gap z_{max} is ~1.82 mm, the maximum movement velocity is about ±0.064 m/s, the acceleration/deceleration are listed in **Table 4-1**. With different contact times, the shape of the *z(t)* and *v(t)* profiles almost kept unchanged, excluding possible influences of z_{max} and the maximum velocity and acceleration/deceleration on the output of power of the TE-KEH.

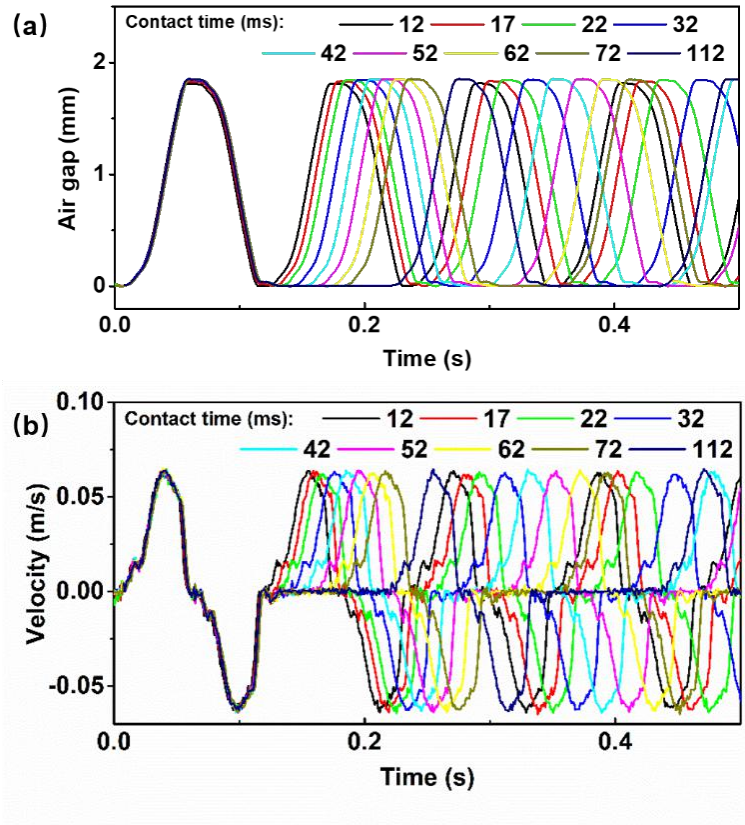

Figure 4-1 The time-dependent (a) air gap and (b) motion velocity profiles with different contact times, recorded by the linear motor system in experiments.

The output voltages of the TE-KEH with different contact times were measured with oscilloscope using a 100 MΩ probe and shown in **Figure 4-2**. The first positive voltage peak value is around 480 V in all measurements, the negative voltage peak values are all around -250 V, and the rest positive voltage peak values monotonically increase with the contact time.

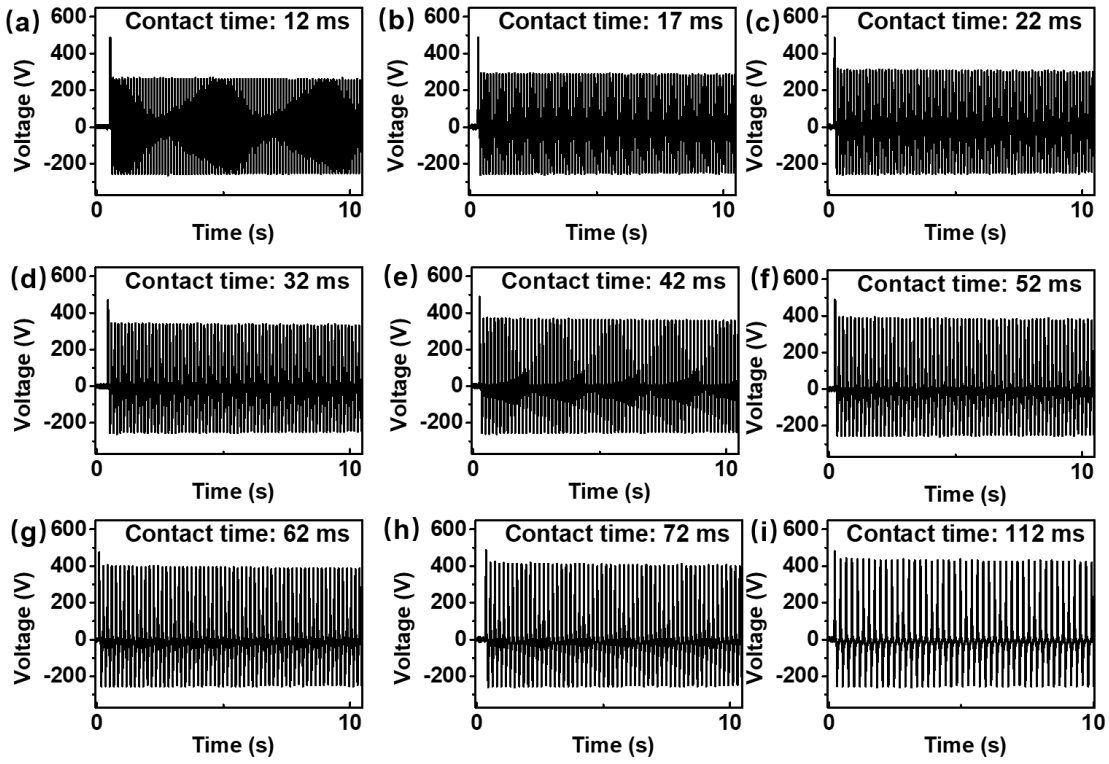

Figure 4-2 The output voltages of the TE-KEH with the contact time of (a) 12 ms; (b) 17 ms; (c) 22 ms; (d) 32 ms; (e) 42 ms; (f) 52 ms; (g) 62 ms; (h) 72 ms; and (i) 112 ms, respectively.

The instantaneous output power *P(t)* of the TE-KEH were calculated from the output voltage using the Joule's law and shown in **Figure 4-3(a)**. With increasing contact time, all the first two *P(t)* peaks corresponding to the positive and negative voltage peaks in the first motion cycle were almost the same. From the second motion cycle, the *P(t)* peak values monotonically increased with the contact time. The average output power (*AvgP*) of the TE-KEH in ten seconds from the beginning of the first *P(t)* peak were calculated by dividing the integration of the *P(t)* during this period by the period (ten seconds), which is shown in **Figure 4-3(b)**. With the contact time increasing from 12 ms to 52 ms, the *AvgP* was increased from ~150 μW to the maximum value of ~197 μW though the frequency of the driving motion was decreased, which means the efficiency of the kinetic-electric conversion by the TE-KEH was increased with the contact time. With the contact time further increasing to 112 ms, the *AvgP* decreased to ~165 μW due to a decrease of the input kinetic energy power with lower motion frequency.

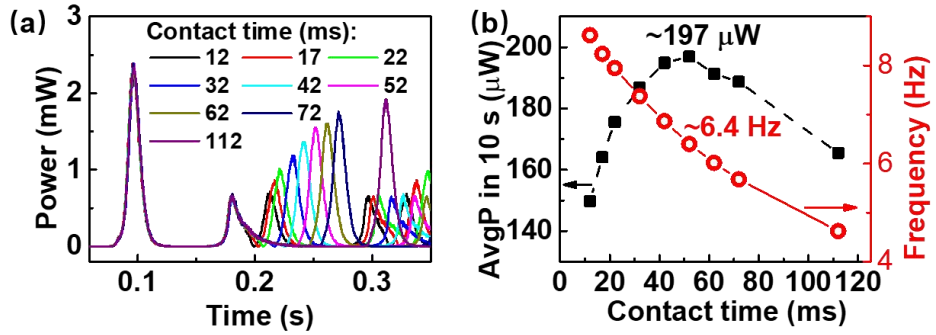

Figure 4-3 (a) The instantaneous output power and (b) the average output power of the TE-KEH with different contact times which also led to different driving motion frequencies.

To further ensure it was the contact time not the possible variation in the surface charge amount on the PTFE film that had influenced the output *AvgP* of the TE-KEH, the transferred charge amount of the TE-KEH before and after all the output voltage measurements were recorded and shown in **Figure 4-4**. In these charge-transfer measurements, the maximum air gap was set at ~20 mm, both the contact time at zero-gap and the maximum air gap position were set as 1s. The maximum transferred charge amount was ~93 nC before and ~96 nC after all the measurements. The change in the transferred charge amount is ignorable, excluding the influence of the surface charge amount on the results shown in **Figure 4-2** and **Figure 4-3**.

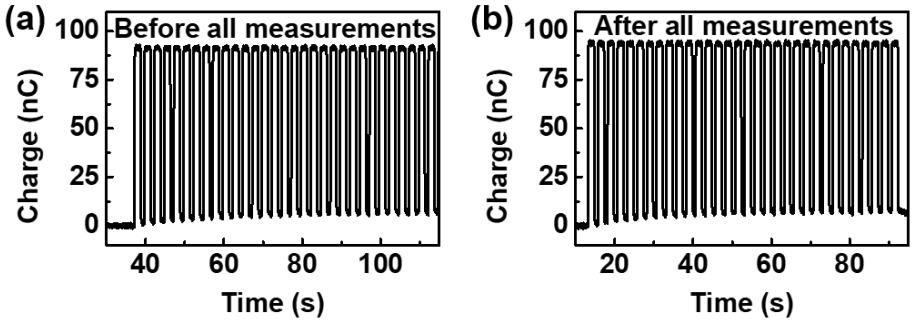

Figure 4-4 The transferred charge amount of the TE-KEH (a) before and (b) after all the output voltage measurements.

These experimental results verify that appropriate contact time is beneficial for improving the output power and the mechanic-electric conversion efficiency of the TE-KEH. To further investigate this strategy, corresponding simulations in MATLAB were conducted and discussed in section 4.2.2.

4.2.2 Simulation results

The similar simulation method with that in **Chapter 3** was used, except that a finite differential equation solver *"ode45"* instead of the symbolic differential equation solver *"dsolve"* was used for a faster calculation speed. The geometric parameter values were set same with the TE-KEH in the experiment, the surface charge density was estimated from the maximum transferred charge amount in **Figure 4-4**, and the driving motion parameter values (z_{max}, v_1, v_2, a_1, a_2, a_3, and a_4) were estimated from recorded data in **Figure 4-1**. All parameter values used in the simulations are listed in **Table 4-1.**

Table 4-1 Parameter values used in simulating the output of the TE-KEH with different contact times.

Parameter	Value
Area of electret film S	16 cm^2
The dielectric constant of the electret film ε_r	2.1
The thickness of the electret film d_f	55 μm
Effective surface charge density on the electret film σ	-60 $\mu C/m^2$
Maximum air gap z_{max}	1.82 mm
Minimum air gap	0
Acceleration a_1	2 m/s^2
Maximum speed v_1	0.064 m/s
Deceleration a_2	-3.1 m/s^2
Wait time t_{w1}	0.012 s
Deceleration a_3	-2.2 m/s^2
Maximum speed v_2	-0.064 m/s
Acceleration a_4	3.65 m/s^2
Load resistance R	100 MΩ
Contact time (Wait time t_{w2})	0~252ms

The simulated $z(t)$ and $v(t)$ curves with different contact times are shown in **Figure 4-5**. The corresponding $Q(t)$, $V_{E\text{-}KEH}(t)$, $P(t)$, and QV curves of the TE-KEH are shown in **Figure 4-6**, **Figure 4-7**, **Figure 4-8**, and **Figure 4-9**, respectively.

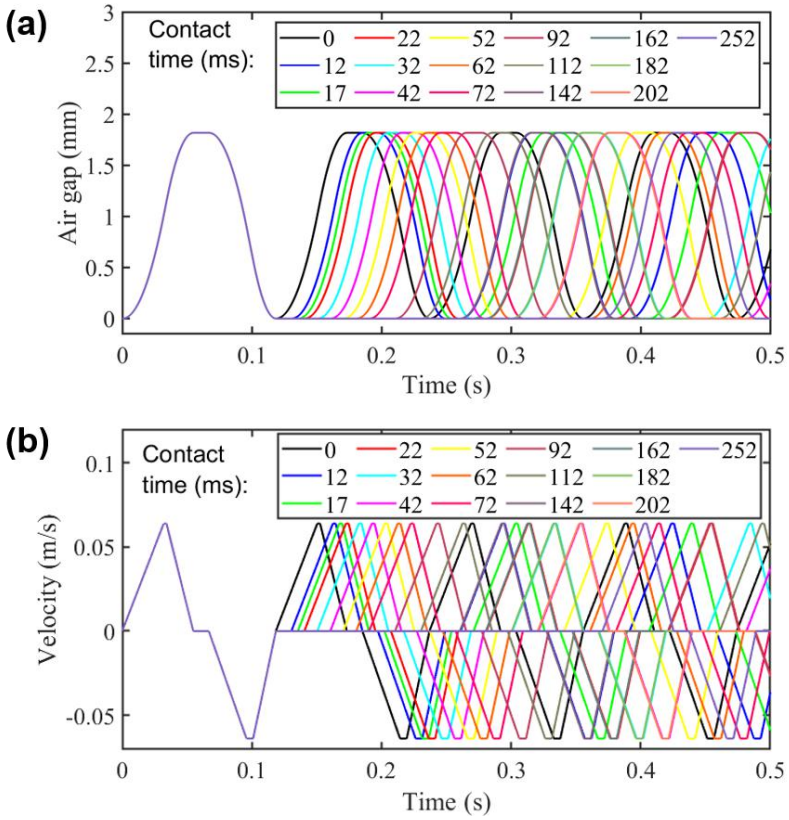

Figure 4-5 Simulated (a) *z(t)* and (b) *v(t)* curves with different contact times, using parameter values in Table 4-1.

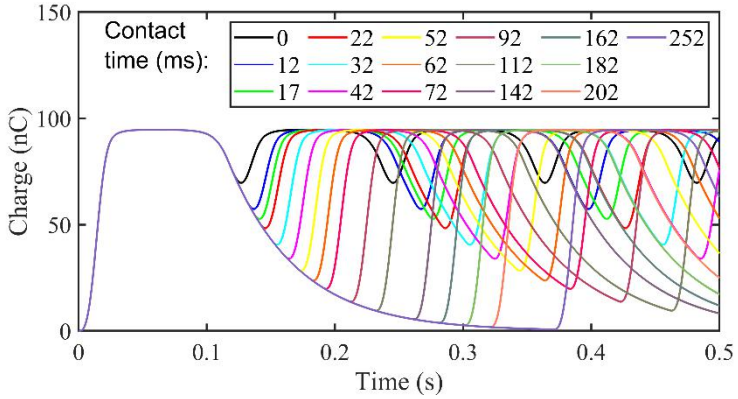

Figure 4-6 Simulated *Q(t)* curves of the TE-KEH with different contact time.

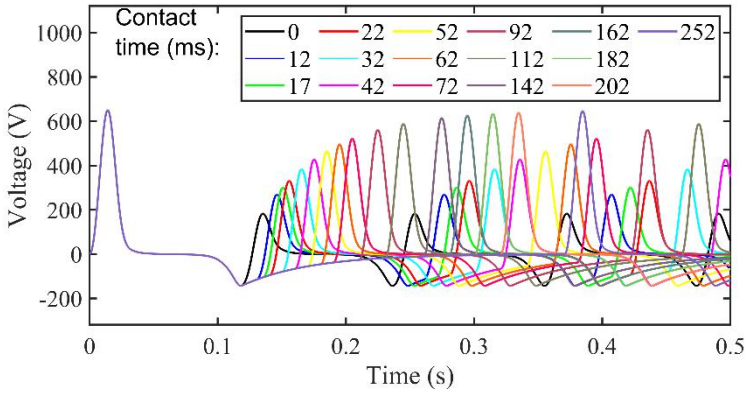

Figure 4- 7 Simulated $V_{E\text{-}KEH}(t)$ curves of the TE-KEH with different contact time.

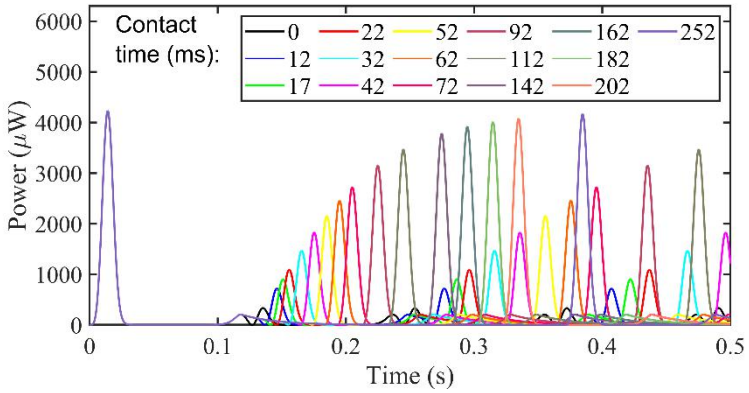

Figure 4- 8 Simulated *P(t)* curves with different contact time.

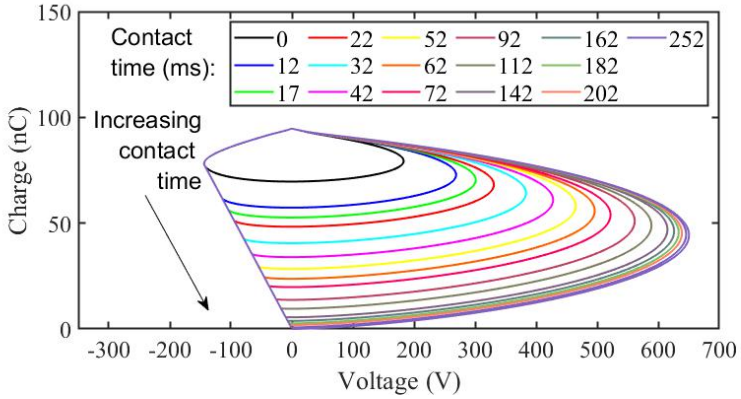

Figure 4- 9 Simulated QV curves of the TE-KEH with different contact times.

As shown in **Figure 4- 9**, with increasing contact time, the QV loop has a larger area, which means the TE-KEH outputs more energy per working cycle to the load resistance. The average output power (*AvgP*) of the TE-KEH in each motion cycle was calculated from the simulated *P(t)* curves using the equation *(3-25)*. As shown in **Figure 4- 10**, in the first motion cycle, the *AvgP* decrease with increasing contact time since most of the output energy in this cycle is released during the first separation

process which is all the same whatever the contact time is as shown in **Figure 4-8**, and a larger contact time leads to a longer period. But from the second motion cycle, the *AvgP* with 0 contact time becomes the lowest due to the least transferred charge per cycle.

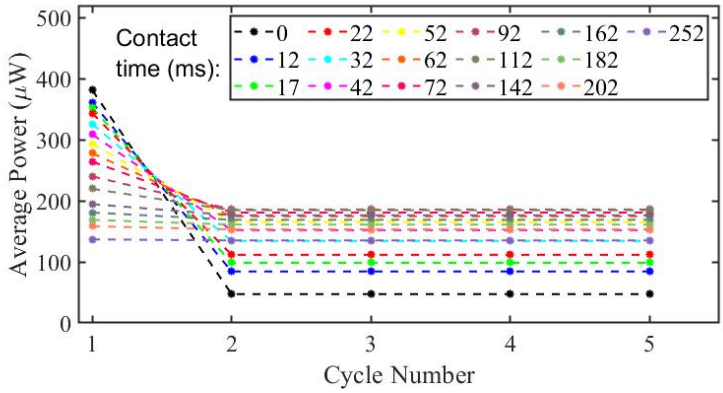

Figure 4-10 The average output power per motion cycle of the TE-KEH from the first to the fifth cycle.

The *AvgP* in the fifth working cycle with different contact times are plotted in **Figure 4-11** to clearly show the influence of the contact time on *AvgP* of the TE-KEH. Like the experimental results presented in **Figure 4-3**, the *AvgP* first increases and then decreases with the contact time.

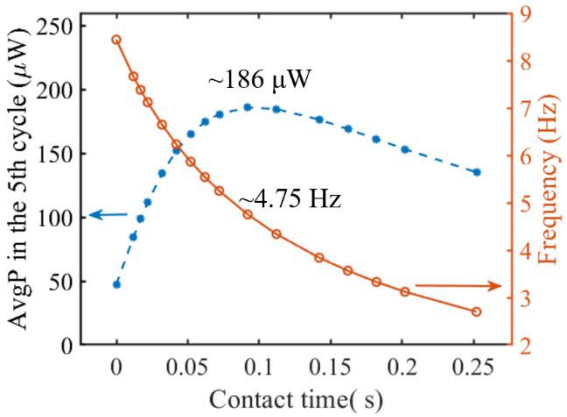

Figure 4-11 Simulated average output power (*AvgP*) of the TE-KEH in the fifth working cycle with different contact times.

The simulated maximum *AvgP* is ~186 μW, which is close to the experimental value of ~197 μW in **Figure 4-3(b)**. However, the optimum contact time of around 0.092s (corresponding to the motion frequency of ~4.75 Hz) is quite different from the experimental result of around 0.052s (corresponding to the motion frequency of ~6.4 Hz). There are several possible causes for this, such as the slight difference

between the actual and the simulated motion curves, the influence of the surface morphology of the electret film and the electrodes, the influence of parasitic capacitance. Several of these possible causes will be discussed in section 4.4.1.

4.3 The maximum theoretical output energy per working cycle of the TE-KEHs with switch controlling

4.3.1 Parallel-connected switch-controlled working cycles

The output energy of the TE-KEH per working cycle increase with the contact time as shown in **Figure 4-9**. There must be a limit of the output energy of the TE-KEH with given maximum air gap and surface charge density. To calculate the maximum theoretical output energy per working cycle of the TE-KEHs, Zi et al. [91] proposed the concept of the 'cycles for maximized energy output' (CMEO). They defined the CMEO by four working steps as shown in **Figure 4-12**, using a lateral-sliding (LS) mode TE-KEH (termed as TENG in their article) as an example. The TE-KEH was connected in parallel to a switch. In step 1 of the CMEO, the switch was open-circuited while the relative displacement between the tribo-electret layer and the top electrode increased from 0 to the maximum value of x_{max}; in step 2, the switch was closed to enable the complete charge-transfer between the two electrodes; then in step 3, the switch was open-circuited again while the relative displacement decreased from x_{max} to 0; at last in step 4, the switch was closed again to enable the complete charge-transfer in the opposite direction with that in step 2, making the QV curve go back to the beginning state in step 1 and become a closed loop.

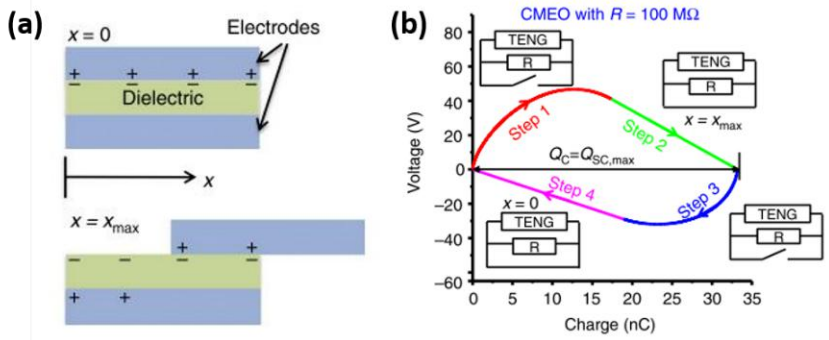

Figure 4-12 The CMEO of a lateral sliding mode TE-KEH defined by Zi et al. [91]. (a) Schematic diagram of the LS-mode TE-KEH with the displacement x=0 and x=x_{max}. (b) QV curve of the TE-KEH during the CMEO with the load resistance R=100MΩ.

They declared that the TE-KEH could output the maximum energy per cycle in such a working cycle with load resistors. However, it should be noticed that the load resistance was short-circuited by the closed switch in step 2 and step 4 of the cycle, which means most of the electric energy was not consumed by the load resistance but was dissipated by the switch during these two steps. Therefore, we propose a series-connected switch-controlled CMEO, taking a CS mode TE-KEH as an example.

4.3.2 Series-connected switch-controlled working cycles

As illustrated in **Figure 4-13**, for the series-connected switch-controlled CMEO, the switch is connected in series with the load resistance (here is the oscilloscope with a 100 MΩ probe).

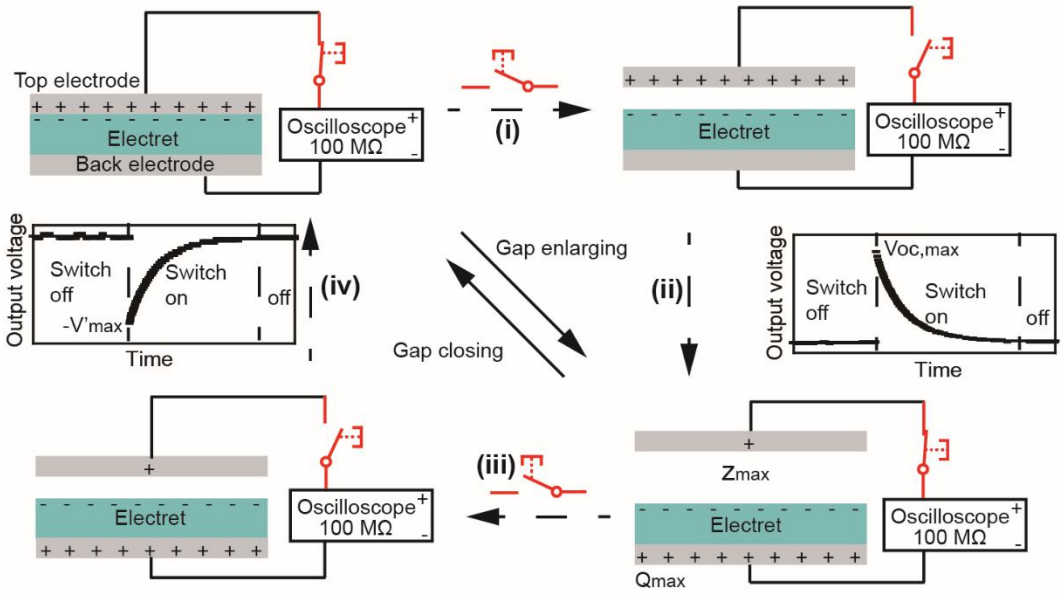

Figure 4-13 Illustration of four working steps of the series-connected switch-controlled CMEO of a CS mode TE-KEH.

The working process also consists of four steps. In step (i), the top electrode fully contacts with the electret film while keeping the switch closed for long enough time to have an initial electric equilibrium state, then the switch is disconnected, and the top electrode moves away from the electret film; in step (ii), the top electrode keeps still after arriving the maximum distance with gap of z_{max}, then the switch is closed and kept closed for long enough time to complete the charge-transfer (which means the electric equilibrium state is re-established, i.e. $V_{E\text{-}KEH} = 0$) between the top and back electrodes through the load resistance, the TE-KEH outputs a voltage pulse with the peak value of $V_{oc,\,max}$ during this process; next, in step (iii), the switch is turned off and

kept open-circuited, and the top electrode moves towards the electret film; finally in step (iv), the top electrode keeps contact with the electret film, the switch is closed and kept short-circuited for long enough time to complete the charge-transfer, the TE-KEH outputs an opposite voltage pulse with peak value of $-V'_{max}$ and goes back to the initial electric equilibrium state in step (i).

In this series-connected switch-controlled CMEO, the TE-KEH output the same maximum energy per cycle with the same maximum air gap whatever the load resistance is, as illustrated in **Figure 4- 14.**

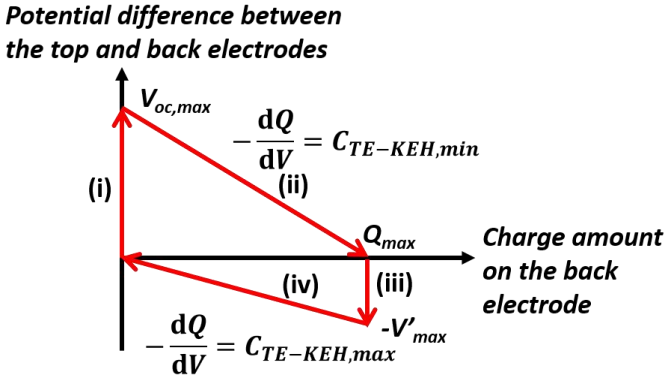

Figure 4- 14 The maximum possible QV cycle of the TE-KEH.

This maximum possible QV cycle consists of two right triangles. In step (i), the voltage ($V_{E\text{-}KEH}$) between the top and back electrodes increases to $V_{oc,max}$ without charge-transfer since the switch is open-circuited; in step (ii), the top electrode stop moving at the maximum gap value of z_{max}, the total capacitance of the TE-KEH has the minimum value $C_{TE\text{-}KEH,\ min}$, and the charge-transfer between the two electrodes leads to the decrease of $V_{E\text{-}KEH}$ from $V_{oc,\ max}$ to 0 and the increase of charge amount on the back electrode from 0 to Q_{max}; in step (iii), the voltage decrease from 0 to $-V'_{max}$ without charge-transfer; finally in step (iv), the top electrode contacts with the electret film and keeps still, the total capacitance of the TE-KEH gets the maximum value $C_{TE\text{-}KEH,\ max}$ which equals the capacitance of the electret film C_f, the charge-transfer between the two electrodes leads to the increase of $V_{E\text{-}KEH}$ from $-V'_{\ max}$ to 0 and the decrease of charge amount on the back electrode from Q_{max} to 0.

This QV cycle is the same with the CMEO with infinite load resistance proposed by Zi et al [91], but it can be reached with any load resistance if the TE-KEH follows the series-connected switch-controlled CMEO, and the electric energy during the charge-transfer process is all consumed by the load resistance. Note that the required

time for complete charge-transfers in step (ii) and (iv) is dependent on the time constant of the total circuit which is related to the load resistance.

From **Figure 4-14**, it is easy to calculate the area of this QV cycle as:

$$W_{max} = \frac{1}{2} Q_{max}\left(V_{oc,max} + V'_{max}\right) \qquad (4\text{-}1).$$

Q_{max} is the maximum transferred charge amount between the two electrodes, which can be calculated by:

$$Q_{max} = \frac{-Q_f C_f}{C_f + C_{gap}(z_{max})} \qquad (4\text{-}2)$$

with Q_f is the effective surface charge amount on the top side of the electret film, C_f is the capacitance between the top side of the electret film and the back electrode, and $C_{gap}(z_{max})$ is the capacitance between the top electrode and the top side of the electret film when the air gap reaches the maximum value of z_{max}.

The $V_{oc,\,max}$ and V'_{max} can be calculated by:

$$V_{oc,\,max} = \frac{-Q_f}{C_{gap}(z_{max})} \qquad (4\text{-}3)$$

$$V'_{max} = \frac{Q_{max}}{C_f} = \frac{-Q_f}{C_f + C_{gap}(z_{max})} (4\text{-}4).$$

Combing equations *(4-1) ~ (4-4)*, there is:

$$W_{max} = \frac{Q_f^2 (C_f^2 + 2C_f C_{gap}(z_{max}))}{2C_{gap}(z_{max})(C_f + C_{gap}(z_{max}))^2} \qquad (4\text{-}5).$$

It can be noticed that W_{max} is only related to Q_f, C_f, and $C_{gap}(z_{max})$. Further, if the fringe and parasitic capacitance are ignorable, and all the components of the TE-KEH are regarded as ideal rigid bodies, with replacing the Q_f by the product of the effective surface charge density σ and area S of the electret film, equations *(4-2) ~ (4-5)* can be rewritten as:

$$Q_{max} = \frac{\sigma S z_{max}}{d_f/\varepsilon_r + z_{max}} \qquad (4\text{-}6)$$

$$V_{oc,\,max} = \frac{\sigma z_{max}}{\varepsilon_0} \qquad (4\text{-}7)$$

$$V'_{max} = \frac{Q_{max}}{C_f} = \frac{\sigma}{\varepsilon_0 \varepsilon_r / d_f + \varepsilon_0 / z_{max}} (4\text{-}8)$$

$$W_{max} = \frac{\sigma^2 S z_{max}^2}{2\varepsilon_0 (d_f/\varepsilon_r + z_{max})} \qquad (4\text{-}9)$$

From equation *(4-9)*, W_{max} is proportional to the square of σ, and it is also correlated to S, z_{max}, and d_f which are geometric parameters of the TE-KEH, and ε_r which is a material's property of the electret. This equation provides a general guide on how these parameters influence the theoretical limitation of the output energy of the contact-separation mode TE-KEH in one working cycle, which however can't be used to estimate the output power of the TE-KEH since it doesn't contain the information on the period of such a working cycle.

4.4 Several usually unfavorable factors that would reduce the practical output energy per working cycle of the TE-KEH

4.4.1 The microscale incomplete surface contact

In the series-connected switch-controlled CMEO illustrated in **Figure 4-13**, the step (ii) and (iv) can be regarded as the discharging process of an RC circuit. The voltage across the capacitor varies with time in an exponential during this process, with the time constant that equals the product of the load resistance R and the capacitance C, where C is the $C_{TE\text{-}KEH,\ min}$ in step (ii), and is $C_{TE\text{-}KEH,\ max}$ which equals C_f in step (iv). Therefore, the value of $C_{TE\text{-}KEH,\ min}$ and $C_{TE\text{-}KEH,\ max}$ can be evaluated by fitting the measured output voltage curves of the TE-KEH.

A pushbutton switch was used to implement the switch-controlled CMEO working cycle on the same TE-KEH made with the 4 cm × 4 cm sized 55 μm-thick PTFE film. Three fitted discharging voltage curves in the step (iv) of the CMEO cycle are given in **Figure 4-15**. The experimental data were measured with the oscilloscope using a probe with 10 MΩ input impedance. From the fitted results, $C_{TE\text{-}KEH,\ max}$ is around 246 pF.

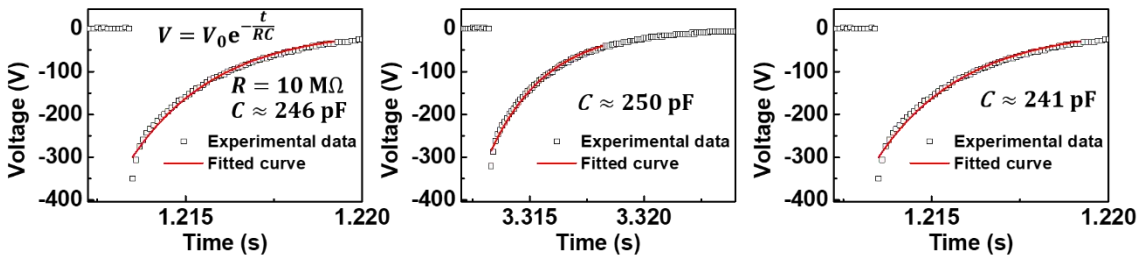

Figure 4-15 Three fitted output voltage curves of the TE-KEH at the contact state.

However, if using the formula *(2-7)* for calculating the capacitance of an ideal parallel-plate capacitor, the calculated C_f is ~ 541 pF, which is more than two times of the fitted $C_{TE\text{-}KEH,\ max}$ result in **Figure 4-15**. If taking the fringe or parasitic capacitance into consideration, the calculated C_f would be larger. Therefore, this difference between the calculated C_f and the fitted $C_{TE\text{-}KEH,\ max}$ must come from other reasons. The microscale surface morphologies of the electrodes and the electret film were considered.

By using the scanning electron microscope (SEM, JEOL JSM-6010PLUS/LV), the microscale surface morphologies of the top electrode (Al foil) and the PTFE film were observed and presented in **Figure 4-16**. There are apparent micro scratches on both of Al foil and the skived PTFE film, which might be formed during their fabrication processes.

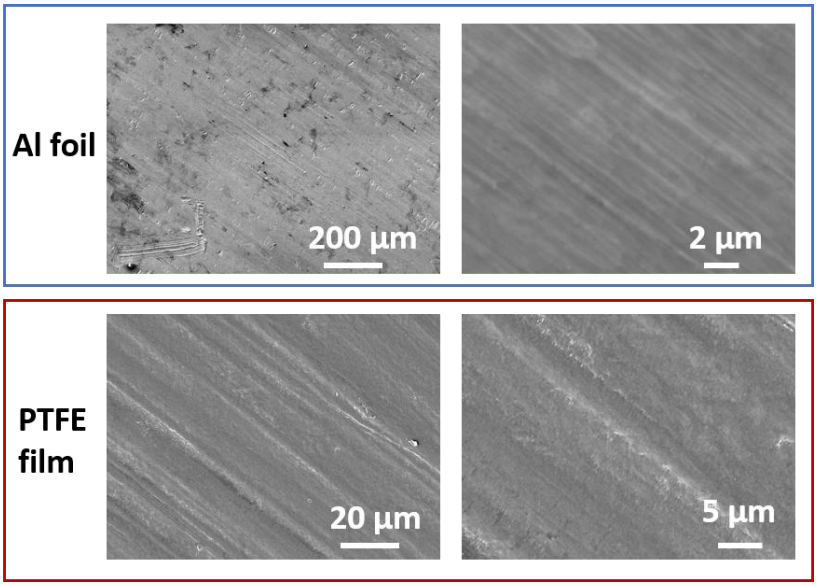

Figure 4-16 SEM images of the Al foil and the PTFE film.

The copper conductive tape as the back electrode may also have some microbubbles between the adhesive matrix and the copper substrate as shown in **Figure 4-17**.

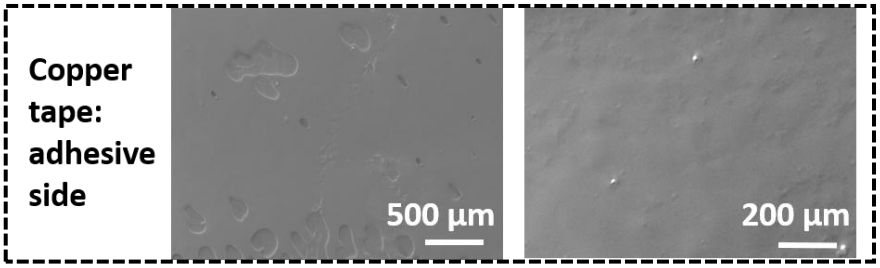

Figure 4-17 SEM images of the adhesive side of the copper tape.

Besides, the adhesive matrix of the copper tape may also form an extra dielectric layer and micro air gaps between the PTFE film and the copper substrate. The micro scratches, microbubbles, the extra dielectric layer, and micro air gaps prevent the ideal complete contact between the back electrodes and the electret film, and between the Al foil and the surface of the electret film at the contact position. It's like that they form many micro capacitors connected in-series with C_f as illustrated in **Figure 4-18(a)**, which makes $C_{TE\text{-}KEH,\ max}$ becomes lower than C_f.

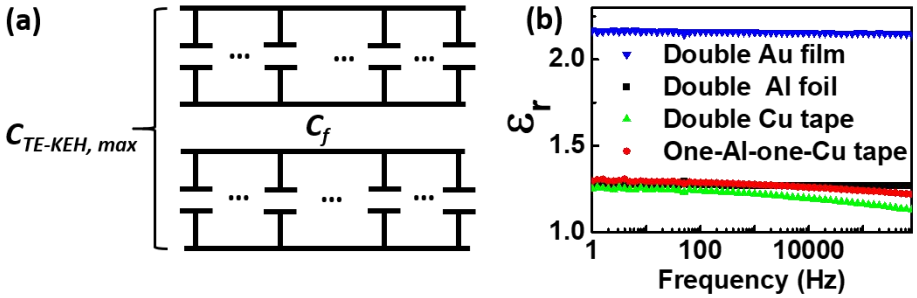

Figure 4-18 (a) The schematic showing how the micro scratch and bubble introduced micro air gap capacitors influence the $C_{TE\text{-}KEH,\ max}$. (b) Frequency-dependent dielectric constant spectra of the PTFE film with different electrodes.

To verify this assumption, the dielectric constant of the PTFE film with different electrodes were measured with the ModuLab® XM MTS system and presented in **Figure 4-18(b)**. All the sample is 1 cm × 1 cm sized 55 μm-thick PTFE film. Double Au film means that both faces of the sample were deposited with a thin layer of gold films by plasma sputtering, double Al foil means that both faces of the sample were attached with Al foil, double Cu tape means that both faces of the sample were attached with the adhesive copper tapes, and one-Al-one-Cu tape means that one face of the sample was attached with the copper tape and the other one with Al foil which is the same with the TE-KEH structure. For the sample with sputtered Au films which could have good contact with the PTFE film, the measured dielectric constant ε_r at 1 Hz is about 2.17 that is in agreement with the reported value of 2.1~2.2 [159], while for other samples, measured ε_r at 1 Hz is between 1.25~1.30 which is quite lower than the reported value.

The lower effective ε_r value would lead to lower output energy per working cycle of the TE-KEH than the maximum possible value according to the equation *(5-9)*. And it may be responsible for that the optimum contact time from simulation results in section 4.2.2 is about 1.77 times of the optimum contact time from experimental

results in section 4.2.1, since the ε_r of the PTFE film measured with good surface contact (double Au film) is about 1.67~1.73 times of the effective ε_r value of the PTFE film with incomplete surface contact. It may also be one reason that leads to lower output voltage peak values of the TE-KEH form experimental results than those in form experimental results in section 3.4.3.

4.4.2 The electric breakdown

The positive output voltage peak curves in step (ii) of the series switch-controlled CMEO of the same TE-KEH were also fitted to evaluate the $C_{TE\text{-}KEH,\ min}$, as shown in **Figure 4-19(a)~(c)**. There were two positive voltage peaks correspond to one negative voltage peak, which implied the occurrence of an electric breakdown in the circuit.

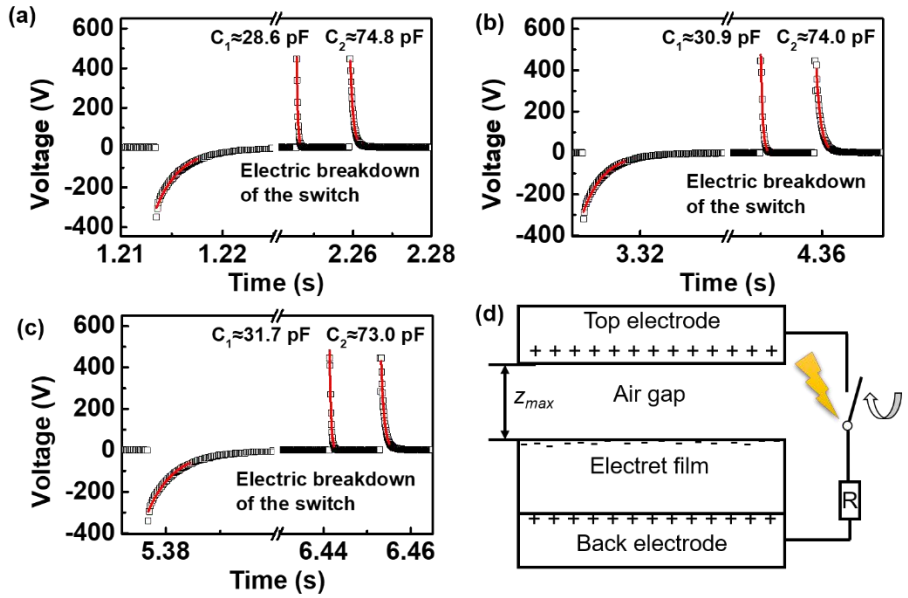

Figure 4-19 (a), (b), and (c) are three fitted output voltage curves of the TE-KEH at the separation state. (d) The illustration shows the electric breakdown that happens at the open-circuited switch.

From the discharge curve fitting result, the total capacitance of the circuit corresponding to the first positive voltage peak (C_1) was around 30 pF, lower than the capacitance corresponding to the second positive voltage peak (C_2) which was around 74 pF. This implied that the electric breakdown occurred when the open-circuited pushbutton switch was pushing from the open-circuited state to the short-circuited state as shown in **Figure 4-19(d)**. As can be imagined, the open-circuited pushbutton switch can be regarded as a capacitance before it was fully closed since there was an

air gap between the two electrodes of it. When the switch was pushing from the open-circuited state to the short-circuited state, the capacitance formed by the switch increased with the air gap between its two electrodes decreasing, the capacitance of the total circuit also increased since the TE-KEH was connected in series with the switch, and the two electrodes kept holding a high voltage generated by the TE-KEH, then when the air gap between the two electrodes of the switch decreased to a certain value, air breakdown might occur according to the Paschen's law [90], some charge-transfer between the two electrodes would happen through the conductive path formed by the air gap breakdown though the switch was not fully closed yet, until the voltage was decreased below the threshold value for the electric breakdown, then the second charge-transfer process would occur when the switch was fully closed to complete the charge-transfer between the two electrodes of the TE-KEH. That's why there were two positive voltage peaks in one working cycle of the TE-KEH, and the first positive voltage peak corresponded to a smaller capacitance than the second one. If the electric breakdown occurred between the top electrode of the TE-KEH with the PTFE surface during their separation process, C_1 would be larger than C_2 since the $C_{TE\text{-}KEH}$ kept decreasing during the separation process.

This electric breakdown of the switch would also lead to lower output energy per working cycle of the TE-KEH than the maximum possible value since part of the electric energy was consumed by the air breakdown process.

Besides the electric breakdown of the switch, if the surface charge density of the electret film is too high, air breakdown may also occur between the top electrode and the electret film, which will reduce the effective surface charge density of the electret film and thus reduce the output power of E-KEHs. This may be happed to electrets pre-charged by other charging methods such as ion injections [90]. For the tribo-charging method, the maximum triboelectric charge density of the electret is also limited by the air breakdown effect. The threshold of the air breakdown voltage is related to the air pressure according to the Paschen's law. Therefore, Wang et al. [160] greatly improved the effective maximum triboelectric charge density on the electret film of a TE-KEH to remarkable 1003μC/m^2 by placing it in a vacuum chamber with extremely low air pressure which can shift the Paschen's curve and with the help of a doped ferroelectric barium titanate (BT) substrate layer. Quite recently, X. Xia, J.J. Fu,

and Y.L. Zi [161] proposed a method to assess the output capability of TE-KEHs with taking the constrain of the triboelectric charge density by the air breakdown effect.

Though the air breakdown will constrain the triboelectric charge density and output power of TE-KEHs in most cases, on the contrary, it can also be used to improve the triboelectric charge density and output performance of TE-EKHs with the special design. Also quite recently, D. Liu et al. [162] designed a special electrode structure to take advantage of the air breakdown to attain a quite high triboelectric charge density of 430μC/m^2 on the PTFE film in a TE-KEH and to acquire constant direct current (DC) from the TE-KEH without using rectification and energy storage units, which greatly simplifies the power managements of TE-KEHs.

4.4.3 The parasitic capacitance and the fringe capacitance

The parasitic capacitance means unavoidable and usually undesired capacitance in electric circuits that simply comes from the proximity of different components in the circuits or surrounding objects [163]. For E-KEHs, parasitic capacitance in the electric circuit was usually modeled as a constant capacitor (C_p) connected in parallel with the E-KEHs as introduced in section 2.3.5.3. The C_p would reduce the effective output energy per working cycle of the E-KEHs to the desired electric load, especially with large resistive loads [146, 164], since part of the output current will be shunted to the bypass formed by C_p.

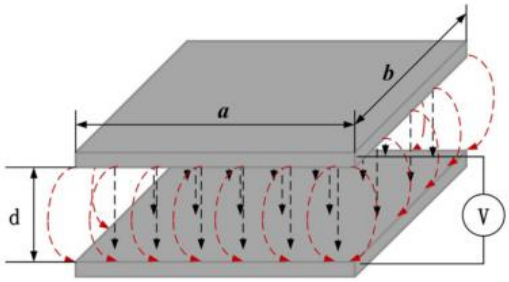

Figure 4- 20 Illustration of curved electric field lines around the plate edges of a parallel-plate capacitance [165].

The fringe capacitance means the excess capacitance of a parallel-plate capacitor due to the presence of curved electric field lines around the edges of plates, as illustrated in **Figure 4- 20**. For E-KEHs, the fringe capacitance will always increase the total capacitance $C_{E\text{-}KEH}$ in comparison with the value calculated by the equation *(2-7)*, but will reduce the ratio of $C_{E\text{-}KEH,max}/C_{E\text{-}KEH,min}$, and consequently reduce output energy of the E-KEHs in comparison with the theoretical value without considering

the fringe capacitance [65, 146]. The fringe capacitance can be analytically calculated using different models [91, 165-167] or numerically simulated using the finite element method [65, 91, 146], and its value is positively related to the ratio between the lateral dimension and the plate distance of the parallel-plate capacitor. For miniature E-KEHs with relatively large lateral dimensions and small air gaps, the influence of the fringe capacitance on the output energy of the E-KEHs can be ignorable in most cases in comparison with the impact from the parasitic capacitance.

The ignored parasitic capacitance and fringe capacitance could be one reason that leads to lower output voltage peaks of the TE-KEH form experimental results than those in form experimental results in section 3.4.3.

4.5 Other optimizations

4.5.1 Tribo-charging

With the optimum contact time, the output power of the TE-KEH could be further improved by tribo-charging the PTFE film with a higher surface charge density. Since PTFE is the most known tribo-negative material [168], it's facile to tribo-charge it with negative charges by rubbing it with other objects. **Figure 4-21** shows the transferred charge amount, output voltage, and output power of the TE-KEH before and after tribo-charging the PTFE film by rubbing its surface with a nitrile glove.

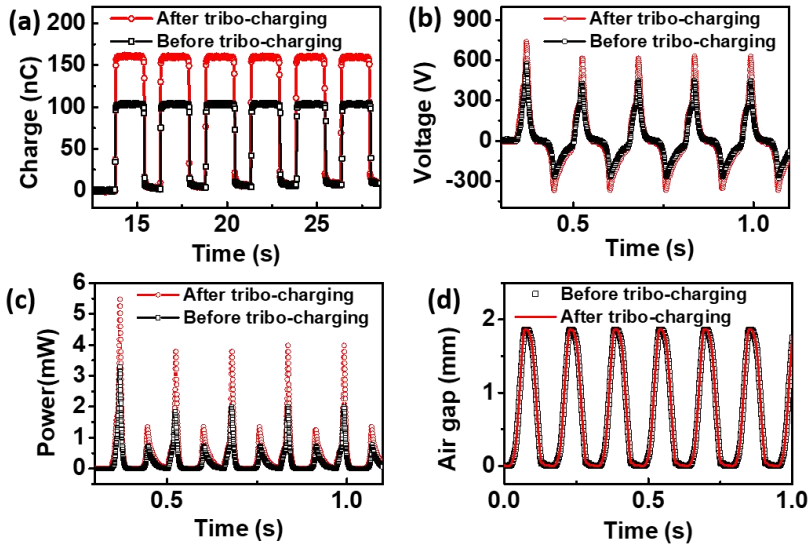

Figure 4-21 Improved (a) transferred charge amount, (b) output voltage and (c) output power of the TE-KEH by tribo-charging the PTFE film. (d) The time-dependent air gap profiles recorded by the linear motor system.

For the transferred charge measurements, the same measurement conditions with that in **Figure 4-4** was used. The maximum transferred charge amount was ~104 nC before the tribo-charging, corresponding to a charge density of ~65 μC/m^2, and it was improved to ~161 nC after the tribo-charging, corresponding to a charge density of ~100 μC/m^2. For the output voltage measurements, the oscilloscope with a 100 MΩ probe of was used, the contact time was set as ~52ms and the time-dependent air gap profiles were shown in **Figure 4-21(d)**, the output power in **Figure 4-21(c)** was calculated from the output voltage by the Joule's law. With the same air gap profile, the output voltage and power of the TE-KEH were apparently increased by the tribo-charging treatment.

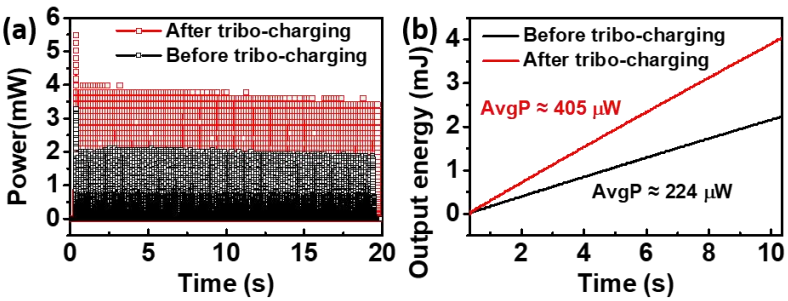

Figure 4-22 (a) The output power of the TE-KEH in 20 seconds, before and after tribo-charging. (b) The accumulated output energy of the TE-KEH in ~ 10 seconds, which clearly shows the improvement of the average output power of the TE-KEH by tribo-charging.

Figure 4-22(a) shows the instantaneous output power of the TE-KEH in 20 seconds. By integrating the instantaneous output power with time, the accumulated output energy and average output power (*AvgP*) of the TE-KEH were obtained and shown in **Figure 4-22(b)**. The *AvgP* of the TE-KEH in the first 10 seconds of measurements was improved from ~224 μW (power density of ~14 μW/cm^2) before the tribo-charging to ~405 μW (power density of ~25.3 μW/cm^2) after the tribo-charging.

4.5.2 Optimization of the maximum air gap

The maximum air gap z_{max} is another significant parameter that influences the performance of the TE-KEH. **Figure 4-23(a)** shows *z(t)* profiles recorded by the linear motor systems when testing the TE-KEH with different z_{max} values, using the same optimized contact time of ~52ms, and other movement parameters (peak motion velocity, acceleration/deceleration) were set the same in the linear motor control

system. Corresponding output voltage and output power of the TE-KEH are plotted in **Figure 4-23(b) and (c)**. With the z_{max} of 1.87 mm, 1.37mm, and 0.87 mm, the peak output voltage and power values were close to each other, while with the z_{max} of 0.3mm, the peak output voltage and power values were apparently lower than others.

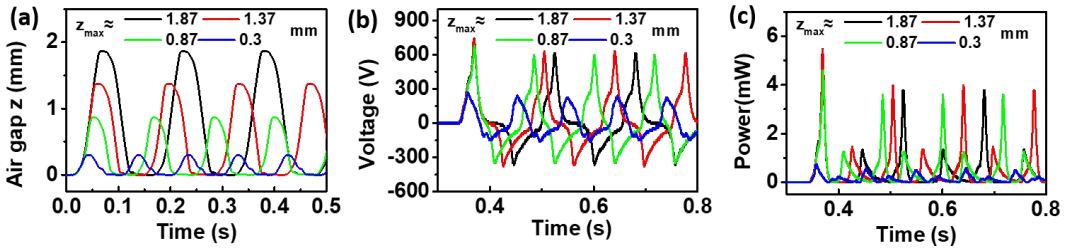

Figure 4-23 (a) z-t profiles with different z_{max} values, and corresponding (b) output voltage and (c) power of the TE-KEH measured with the oscilloscope using a 100 MΩ probe.

The accumulated output energy of the TE-KEH in ~10 seconds with different z_{max} values are plotted in **Figure 4-24(a)**, and corresponding *AvgP* of the TE-KEH in 10s is shown in **Figure 4-24(b)**. With the z_{max} increasing from 0.3 mm to 1.87 mm, the *AvgP* increased at first, peaked at 0.87 mm with *AvgP* of ~503 μW (power density of ~31.4 μW/cm^2), and then decreased, meanwhile the motion frequency monotonically decreased.

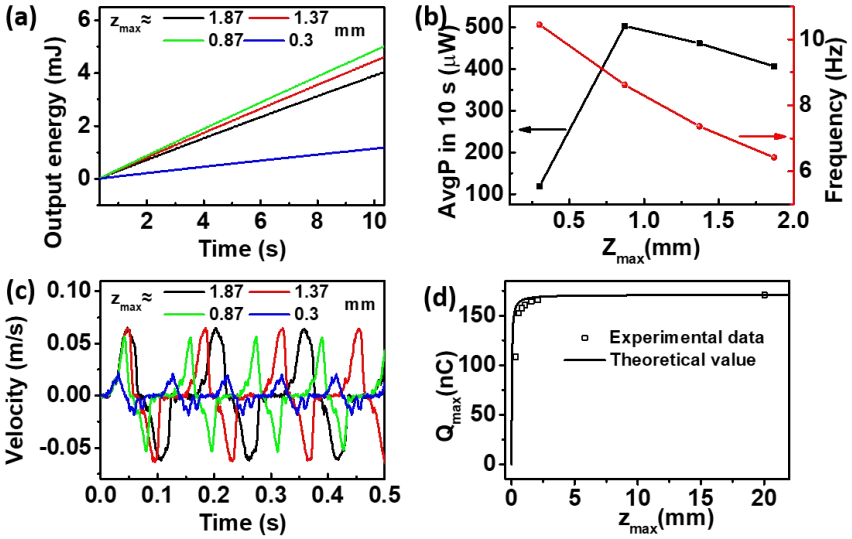

Figure 4-24 (a) The accumulated output energy of the TE-KEH in the first 10 seconds with z_{max}. (b) The average output power of the TE-KEH in ~ 10 seconds and the corresponding mechanical motion frequency with different z_{max}. (c) The recorded *v(t)* curves with different z_{max}. (d) The experimental and theoretical dependence of the maximum transferred charge amount Q_{max} on z_{max}.

This dependence trend of the *AvgP* on z_{max} maybe a consequence of the combination of several factors. At first, the frequency of the mechanical movement monotonically decreased with increasing z_{max} as shown in **Figure 4-24(b)**, this could lead to the decrease of the *AvgP* with increasing z_{max} since less working cycles were carried out by the TE-KEH within a certain period of time. Secondly, with the minimum z_{max} of 0.3 mm, although the movement frequency was the highest, the peak velocity of the motion became the lowest as shown in **Figure 4-24(c)**, because the movement velocity couldn't be accelerated to the same peak value in such a short distance with the same acceleration value (the slope in the velocity curves) with larger z_{max}, this could be one reason that led to the lower *AvgP* with the minimum z_{max} than others. Thirdly, according to the equation *(3-15)*, the maximum transferred charge amount Q_{max} is dependent on z_{max}. **Figure 4-24(d)** shows the theoretically calculated Q_{max}-z_{max} curve by the equation *(3-15)* and experimentally measured data, using the measured Q_{max} value with z_{max} = 20 mm to calibrate the measured and calculated total charge amount. It can be noticed that Q_{max} with z_{max} = 0.3 mm was apparently lower than others, which could also be a significant reason that led to the lower *AvgP* with the z_{max} of 0.3 mm than others. With increasing z_{max} from 0, Q_{max} increased dramatically with small z_{max} and then increased quite gently and approached almost flat with large z_{max}, which is in correspondence with other literature that most of the power of the CS mode TE-KEH is generated at small gap [35].

4.6 Chapter Conclusion

In this chapter, firstly, by increasing the contact time from ~12ms to ~52ms, the average output power of a contact-separation (CS) mode parallel-plate TE-KEH made with a 4 cm × 4 cm sized 55 μm-thick PTFE film to the load resistance of 100 MΩ was improved from ~150 μW to ~197 μW, with the corresponding frequency of the driving motion with the same maximum air gap was decreased from ~8.6 Hz to ~6.4 Hz, which means the energy conversion efficiency of the TE-KEH was also increased. This optimizing strategy to improve the output power of the was also verified by corresponding simulations results. Secondly, a series-connected switch-controlled working cycle was analyzed to obtain the dependence of the maximum theoretical output energy per working cycle of TE-KEHs on the geometrical parameters of TE-KEHs and on the effective surface charge density and dielectric constant of the

electret layer. Thirdly, the influences of the microscale incomplete surface contact, the electric breakdown, the parasitic and the fringe capacitance on the output energy of TE-KEHs were discussed. At last, by the tribo-charging method and the optimization of the maximum air gap, the average output power of the same CS mode parallel-plate TE-KEH made with PTFE film to the load resistance of 100 MΩ was further improved to ~503 μW (corresponding to a power density of ~31.4 μW/cm^2), with a ~100 μC/m^2 effective surface charge density on the PTFE film, an optimum maximum air gap of ~0.87 mm, and a driving motion with frequency of ~8.62 Hz.

This page is intentionally left blank

Chapter 5 Tape-peeling tribo-charged FEP film-based TE-KEHs

5.1 Introduction

Higher effective surface charge density on the electret layer can significantly improve the output power of TE-KEHs [5, 29, 65, 90, 169]. For most charging techniques, high voltage sources and other assorted apparatuses are usually indispensable [67, 170-174]. Triboelectrification, which is the charge-transfer phenomenon between two surfaces or fluid/solid interfaces after contact and separation [175-177], can be used as a facile method to charge dielectrics to get electrets without any equipment [46, 178]. Nevertheless, the triboelectric charge density cannot be directly controlled or varied without changing the materials employed [90].

In this chapter, a novel facile tape-peeling tribo-charging method is used to charge the fluorinated ethylene propylene (FEP) film. Firstly, the surface potential of the FEP film and corresponding output voltage and current of TE-KEHs made with the FEP film after different counts of tape-peeling treatment are measured. Secondly, the surface potential mapping technique is used to analyze the impact of the tape-peeling treatment on the potential distribution of the FEP film. At last, harvesting kinetic energy from wind and human motions with a prototype of this type of TE-KEH is demonstrated, with an apparent ~692% improvement in the output power by the tape-peeling charging method.

5.2 Material properties

Fluorinated ethylene propylene (FEP) is a copolymer of hexafluoropropylene and tetrafluoroethylene. It is the first thermoplastic processing fluoropolymer (due to its low viscosity in comparison with previous fluoropolymers) invented in 1960, with excellent chemical inertness, thermostability, a melting temperature of around 260~275°C, a low dielectric constant (ε_r=2.1 at 23 ℃, 10^2~10^6 Hz) and dielectric loss (0.00006~0.0005 at 23 ℃, 10^2~10^6 Hz), extremely low conductivity (~ 10^{-22} $\Omega^{-1}cm^{-1}$), and high dielectric strength (~19.7 kV/mm) [46, 159]. The FEP film used in our

experiments is 100 μm-thick NEOFLON FEP film produced by Daikin® and bought from Suzhou Guanghui Technology Co. Ltd. It is a flexible and highly transparent film as shown in **Figure 5-1.**

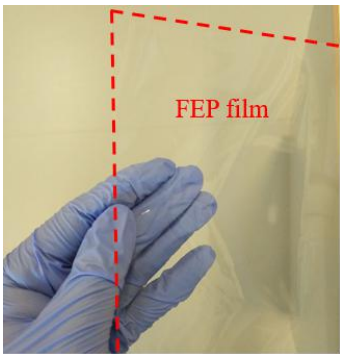

Figure 5-1 Photograph of a piece of the 100 μm-thick FEP film, with outlines marked by the dash red lines.

Figure 5-2 shows the chemical formula of FEP. As an all fluorinated polymer, its molecular link is full of the most electronegative functional group -F [90], which makes it one of the most triboelectrically negative materials in the triboelectric series [91]. This excellent electronegative property together with its outstanding insulating property makes it a good candidate for tribo-charged electrets.

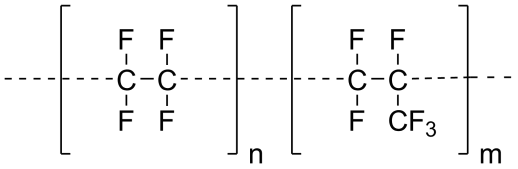

Figure 5-2 The chemical formula of FEP.

The infrared transmission spectrum of the FEP film was measured by a Fourier-transform infrared spectroscopy (FT-IR) spectrometer (type Perkin Elmer Spectrum Two with a Universal Attenuated Total Reflection (type UATR Two) accessory), with a resolution of 4 cm^{-1}. Before the FT-IR test, the FEP film was cleaned by deionized water and ethanol successively using an ultrasonic cleaner. Measured FT-IR spectrum is shown in **Figure 5-3**. the absorption band peaked at the wavenumber (1/wavelength) of 1202 cm^{-1} and 1147 cm^{-1} can be assigned to the CF_2 stretching vibrations, peaked at 982 cm^{-1} to the CF_3 stretching vibration, peaked at 638 cm^{-1} to the C-C-F bending vibration, and peaked at 554 cm^{-1} and 509 cm^{-1} to the CF_2 bending vibration [179, 180]. The FT-IR spectrum of the FEP film is in good accordance with its chemical structure.

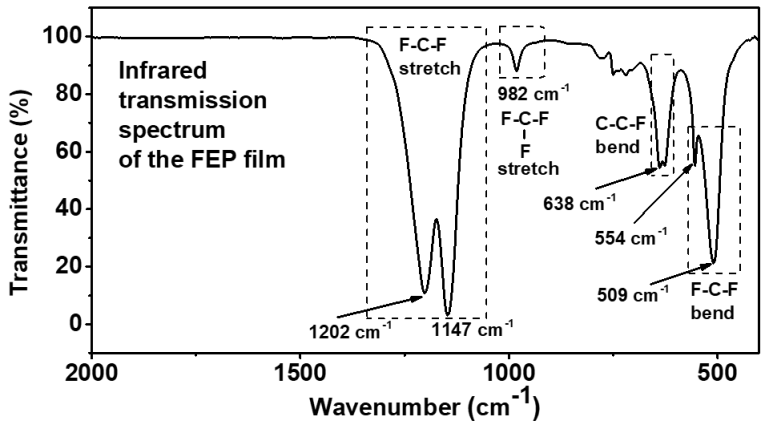

Figure 5-3 The infrared transmission spectrum of the FEP film.

5.3 Methods

5.3.1 Structure and test set-up of the energy harvester

The FEP film-based TE-KEH consists of two parts: one is a piece of FEP film with one side metalized, the other is a metal electrode. To fabricate the TE-KEH, a piece of rectangular FEP film with a size of ~4 × 4 cm^2 was cleaned by deionized water and ethanol using an ultrasonic cleaner at first. Then silver paint was coated on one side of the cleaned and dried FEP film as a back electrode, with margins of ~2 mm in each edge of the film to prevent possible short circuit with the other metal electrode (a piece of aluminum foil with the same size of the FEP film). A copper wire was fixed to the back electrode as a conductive export wire.

The processed FEP film was attached to the sliding block of the linear motor by double-sided adhesive tapes, and the Al foil was attached to a fixed plate faced with the FEP film. All the test set-up on the linear motor system is the same as in section 3.4.1.

5.3.2 Tape-peeling charging process

The FEP film was innovatively charged by an adhesive tape-peeling triboelectrification method. **Figure 5-4** illustrates the process of this method. Briefly, one piece of adhesive tape (Lyreco, polypropylene substrate with an acrylic adhesive) was firstly pasted on the naked side of the processed FEP film, then triboelectrification occurs when the tape was peeled off, making the FEP film negatively charged, and the acrylic adhesive on the sticky side of tape positively charged. The contact between the adhesive and the FEP film could be tight due to the

strong van der Waals interaction [181, 182], and this triboelectrification can change the surface charge density of the FEP film obviously.

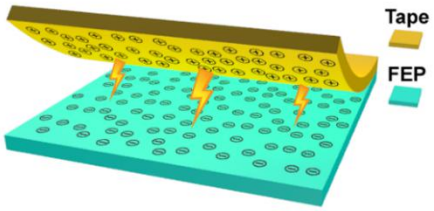

Figure 5-4 The schematic of charging the FEP film with tape.

The Raman spectrum analysis was done with a Jobin Yvon LabRam spectrometer (Horiba Scientific) to identify the main chemical composition of the adhesive on the tape. As shown in **Figure 5-5**, by comparing the measured Raman spectrum with the Raman spectra database, the main chemical component of the adhesive was confirmed to be butyl polyacrylate, also termed as poly(butyl acrylate).

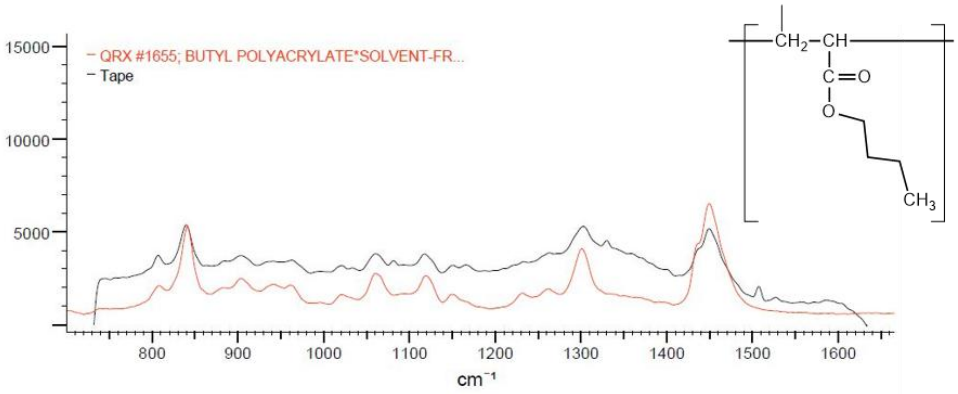

Figure 5-5 The Raman spectrum of the adhesive measured from the tape we used (black line), and the Raman spectrum of the butyl polyacrylate in the database provided by the Bio-Rad Laboratories, Inc (red line). Inset is the chemical constitution of the butyl polyacrylate.

5.4 Results and discussion

5.4.1 Improving the performance of the TE-KEH by the tape-peeling charging method

The improvement in the output voltage and current of the TE-KEH by this tape-peeling charging method for the FEP film is presented in **Figure 5-6**. All the results were measured with the minimum air gap set as 0 (which means a direct contact) and the maximum air gap set as ~20 mm, the maximum moving speed of the sliding block set as ±0.2 m/s and the acceleration/deceleration set as ±10 m/s^2 in both backward and

forward directions. And in each motion cycle, the wait time of the sliding block at the contact position (the contact time) and at the maximum air gap position were both set as ~0.1s for complete charge-transfer. These motion parameters are listed in **Table 5-1**. The period of such a motion cycle is ~0.45s, corresponding to a frequency of ~2.2 Hz.

Table 5-1 Linear motor motion parameters for measuring the output of the FEP film-based TE-KEH

Parameter	Value
Minimum air gap	0
Maximum air gap	~20 mm
Maximum moving speed	±0.2 m/s
Acceleration and deceleration at both directions	±10 m/s^2
Wait time at the two limiting positions	~0.1s

With increasing tape-peeling treatment count from 0 to 5, the output voltage of the TE-KEH gradually increased and then decreased a little after the sixth treatment as shown in **Figure 5-6(a)**. The short-circuit current density (the current divided by the area of the FEP film) had the same trend as shown in **Figure 5-6(b)**.

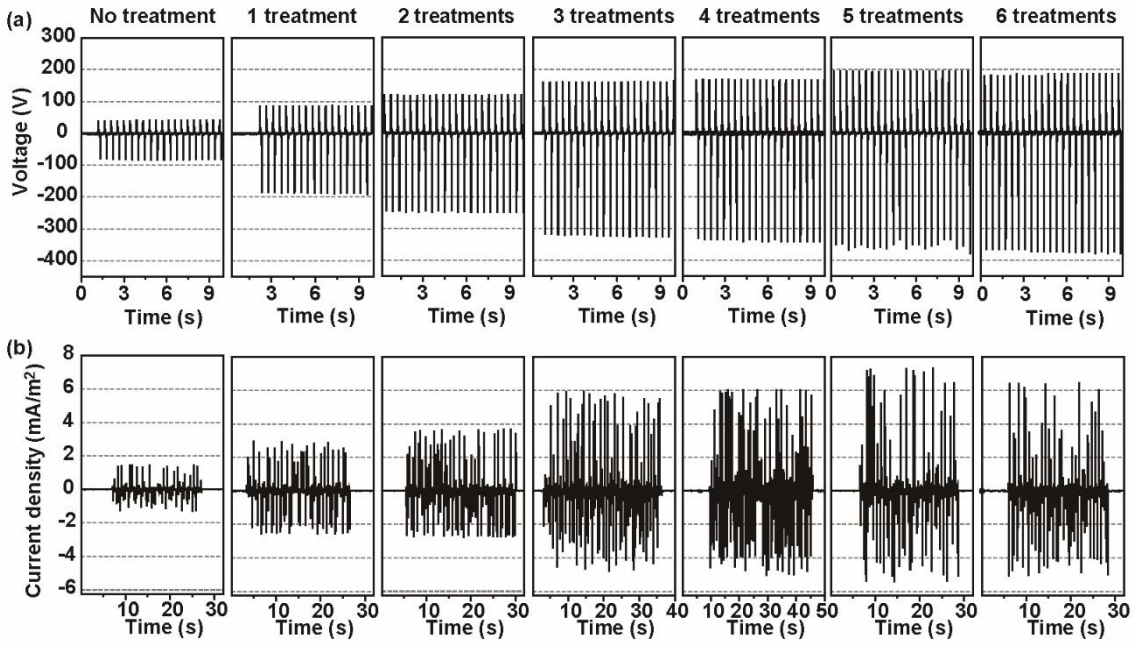

Figure 5-6 Increasing (a) output voltages and (b) current densities of the TE-KEH with the FEP film treated by the tape with increasing counts (from left to right: 0~5 counts). (b) Increasing current densities of the TE-KEH with increasing the treatment count.

The recorded current waveform was not so regular as the voltage. This is because the external circuit resistance was negligible during the current measurement, resulting in a quite transient charge-transfer process between the two electrodes. Meanwhile, the data sampling rate of the electrometer system we used (Keithley 6514 with IEEE 488 cable) is not high enough (the shortest time interval between two data points is ~18ms). Therefore, only one data point could be acquired in one current peak as shown in **Figure 5-7(a)**, which is far from enough to record the full waveform of current peaks. While the oscilloscope for the voltage measurement has a much higher data sampling rate (the time interval between two data points in the was set as 0.2ms), which is enough to record the shape of the full voltage waveform as shown in **Figure 5-7(b)**. Nevertheless, a general variation trend of the current density with the treatment count can still be clearly noticed in **Figure 5-6(b)**. It is noteworthy that for the treatment count from 1 to 4, each treatment count is corresponding to one tape-pealing process, while for the fifth and sixth treatments, three tape-peeling processes were performed to have an observable increase in the surface potential of the FEP film which is monitored with a USSVM2 surface voltmeter (a type of electric field meter, bought from the ALPHALAB Inc. in the U.S.A.) as shown in **Figure 5-8(a)**.

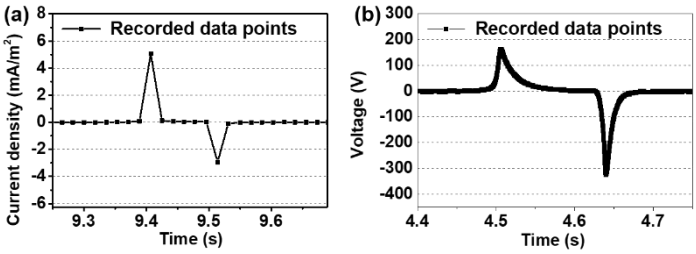

Figure 5-7 (a) Recorded data points in one positive and one negative short-circuit current peaks. (b) Recorded data points in one positive and one negative voltage peaks.

The distance between the probe of the field meter and the FEP film surface was always fixed as 5 mm when measuring the surface potential, as shown in **Figure 5-8(a)**, to exclude the influence of the probe distance on the measured surface potential values for comparisons. The surface potential of the FEP film before any tape-peeling treatment is already negative as -367 V as plotted in **Figure 5-8(b)**, meaning that the FEP film originally has negative charges which may be obtained during its fabrication and processing. With increasing tape-peeling treatment count from 0 to 5, the surface potential maintained negative with the absolute value

gradually increasing, meaning that more negative charges were obtained by the FEP film. However, in the fifth treatment, it took three tape-peeling processes to have such an apparent increase in the surface potential, and after the sixth treatment, the absolute surface potential value even decreases a little. Additionally, the surface potential of the FEP film almost kept unchanged before and after the linear motor test with the treatment count from 0 to 4, revealing the temporal stability of negative charges on the FEP film. While with the treatment count of 5 and 6, the surface potential shows a more apparent decrease after the linear motor test. Possible micro-scale air breakdown [46] may be responsible for the decrease of surface potential after the sixth treatment.

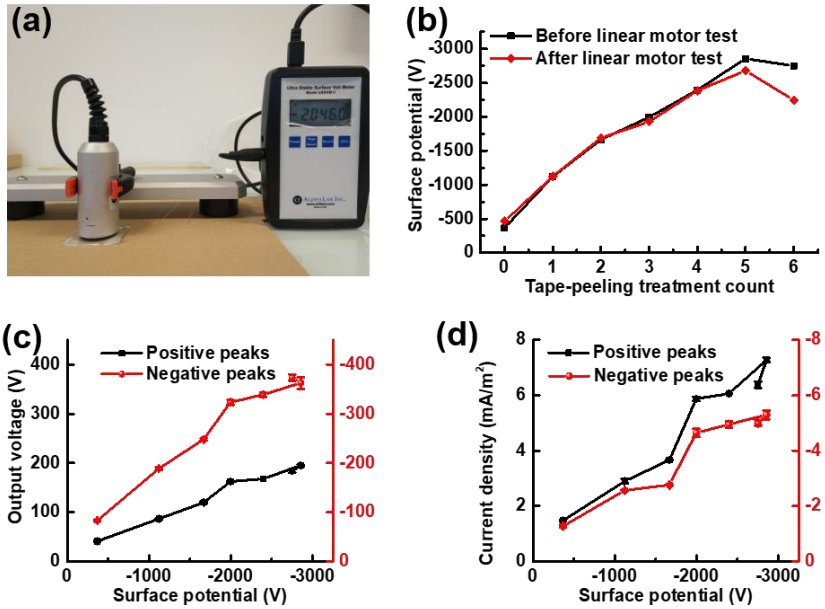

Figure 5-8 (a) Photograph of the surface voltmeter with the probe fixed. (b) The increasing surface potential of the FEP film with tape-peeling treatment counts, before and after the linear motor test. (c) Statistic results of the positive and negative output voltage peak values of the TE-KEH. (d) Statistic results of the positive and negative short-circuit current density peak values of the TE-KEH.

Statistical results of the voltage peak values with the FEP film surface potential controlled by the tape-peeling treatment count are presented in **Figure 5-8(c)**, where the first and the last three voltage peaks from each test result shown in **Figure 5-6(a)** are used for the statistic. With the surface potential of the FEP film increasing from about -367 V to about -2857 V after five tape-peeling treatment counts, the mean positive voltage peak value was increased from 41 V to 195 V, and the mean negative peak value increased from -83 V to -363 V, both with little standard deviation. After the sixth treatment, the mean positive voltage peak value decreased a little to 184V,

while the mean positive voltage peak value was increased a little to about -374 V. Five highest positive and negative short-circuit current peak values from each test result shown in **Figure 5-6(b)** were used for statistics also. As plotted in **Figure 5-8(d)**, with the treatment count increasing from 0 to 5, the mean positive peak current density was increased from 1.5 mA/m^2 to 7.3 mA/m^2, and the negative one increased from -1.3 mA/m^2 to -5.3 mA/m^2 correspondingly, also with little standard deviation. And after the sixth treatment, the mean positive and negative peak current density decreased to 6.4 mA/m^2 to -5.0 mA/m^2 respectively with the decrease of the surface potential.

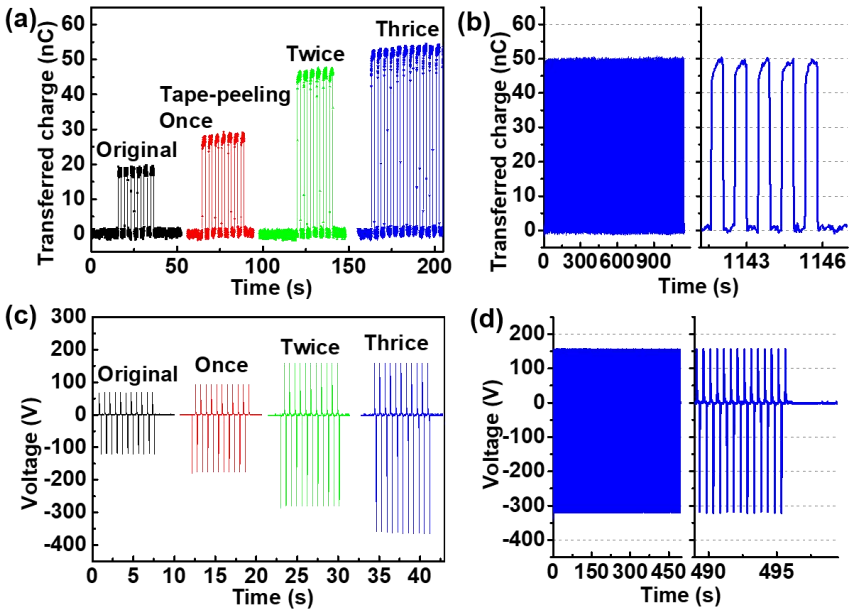

Figure 5-9 (a) Increasing short-circuit transferred charge amount of the TE-KEH by the tape-peeling charging method. (b) The stability of the transferred charge amount of the TE-KEH. (c) Increasing the output voltage of the TE-KEH by the tape-peeling charging method. and output voltage (d) The stability of output voltage of the TE-KEH.

The short-circuit transferred charge amount measured by the Keithley 6514 electrometer from another TE-KEH made with a ~4 cm × 4 cm sized FEP film was shown in **Figure 5-9(a)**. In these measurements, the minimum and maximum air gap, the moving speed and acceleration/deceleration were kept the same as listed in **Table 5-1**, but the wait time at both limit positions was set as ~2s. The transferred charge amount between the two electrodes of the TE-KEH was increased with the tape-peeling treatment count. After three times of tape-peeling treatment, the transferred charge amount in each half working cycle of the TE-KEH was increased from ~19nC to ~53nC, corresponding to an improvement of ~180%. The stability of the charge-

transfer amount of the TE-KEH after the third tape-peelings was verified in a relatively long-time test**.** In this test, the maximum air gap was set as ~2 mm, and the wait time was set as ~0.42s to shorten the period of one motion cycle for measuring more working cycles of the TE-KEH during the test, with other movement parameters unchanged. The period of such a motion cycle was ~0.94s. In more than 1140s, the transferred charge amount had no obvious change as shown in **Figure 5-9(b)**, revealing the stability of the tape-peeling introduced electrostatic charges on the FEP electret film.

The output voltage of this TE-KEH was also increased with the tape-peeling charging count correspondingly as shown in **Figure 5-9(c)**. For these measurements, the maximum air gap was set as ~20 mm, and the wait time was set as ~0.22s, with other movement parameters unchanged as listed in **Table 5-1**. The period of such a motion cycle was ~0.65s. After three times of tape-peeling treatment, the positive voltage peak value was increased from about 69 V to about 159 V, and the negative one was increased from about -120 V to about -365 V. The stability of the output voltage of the TE-KEH after the third tape-peelings was then verified in a relatively long-time test. In this test, the maximum air gap was set as ~5 mm, and the wait time was set as ~0.22s, with other movement parameters unchanged, corresponding to a reciprocating movement frequency of ~2 Hz. Like the transferred charge amount, the output voltage of the TE-KEH also kept stable peak values as shown in **Figure 5-9(d).**

5.4.2 Surface potential mapping

To further investigate the tape-peeling tribo-charging effect, the surface potential mapping technique was used. To get a surface potential mapping, the probe of a non-contacting Trek 341B electrostatic voltmeter was fixed on a pneumatic displacement system as shown in **Figure 5-10**, the FEP film was placed on a sample plate beneath the probe. The probe scanned the area of the FEP film by the stepping movement of the probe and the sample plate in two perpendicular directions to record the surface potential distribution of the FEP film. The scanning process and the data record were controlled by customized LABVIEW-based programs installed on a computer. The Trek 341B electrostatic voltmeter can precisely measure the very localized surface potential of the FEP film based on the field-nulling technique, regardless of the probe-to-surface distance. We set the spatial resolution of the probe scanning as 1 mm,

which means that the Trek 341B recorded one surface potential value per millimeter at both scanning directions.

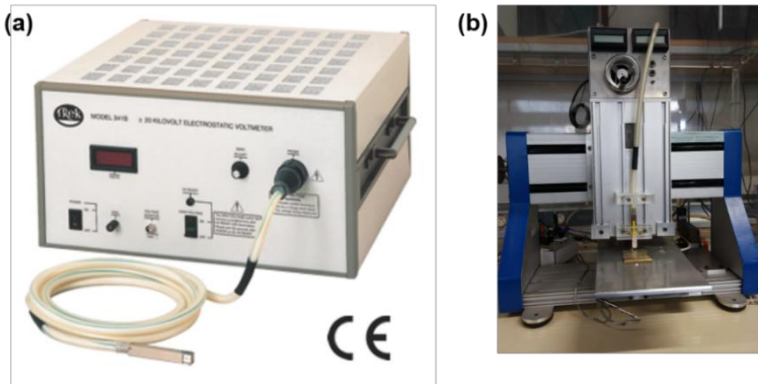

Figure 5-10 (a)Photograph of the Trek 341B electrostatic voltmeter. (b) Photograph of the pneumatic displacement system.

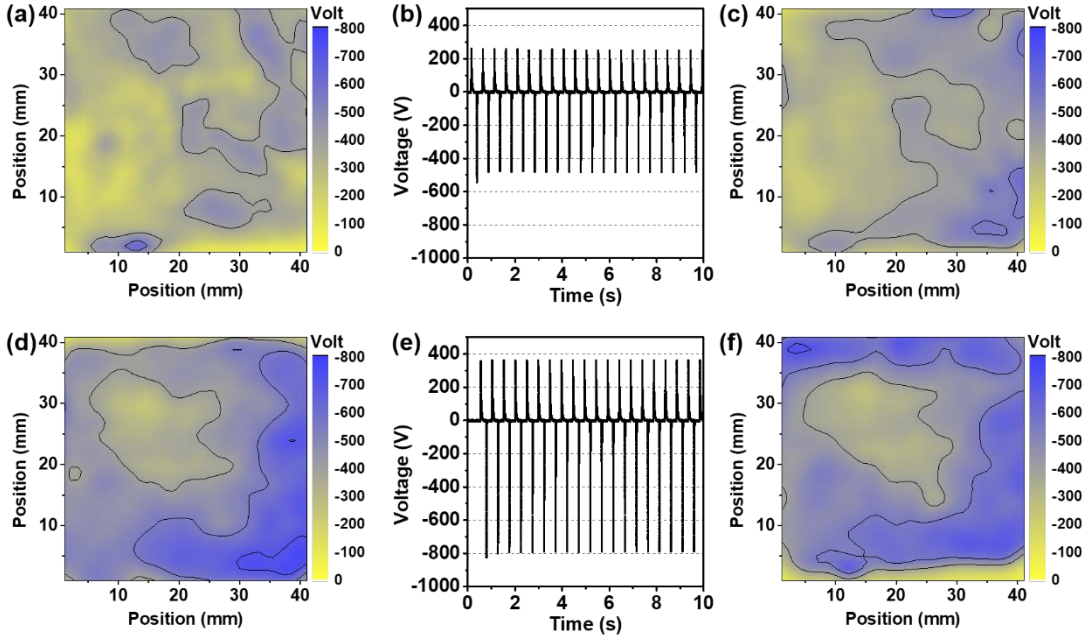

Figure 5-11 (a) The surface potential mapping of the ~4 cm × 4 cm sized FEP film before any test and treatment. (b) The output voltage of the FEP film-based TE-KEH. (c) and (d) Surface potential mapping of the FEP film after the linear motor and after the tape-peeling treatments. (e) The output voltage of the TE-KEH after the FEP film was charged by the tape-peeling method. (f) Surface potential mapping of the FEP film after all the tests.

Figure 5-11(a) is the surface potential mapping of a ~4 cm × 4 cm sized FEP film with backside metalized by silver paint before any test and without tape-peeling treatment. Then the FEP film was mounted onto the linear motor system to measure the output voltage of the FEP film-based TE-KEH. The measured output voltage was plotted in **Figure 5-11(b).** The time-varying air gap and movement velocity curves

during the measurement are shown in **Figure 5-12(a)**, with a maximum air gap of ~3.2 mm, maximum separation velocity of ~0.16 m/s, and maximum approaching velocity of ~-0.22m/s. The surface potential mapping of the FEP film after the linear motor test is shown in **Figure 5-11(c)**.

It can be noticed that the general shape of the potential distribution after the test is similar to that before the test, but the general color tone of the map has a slight shift to the more negative direction. Next, the FEP film was tribo-charged by 5 tape-peeling treatments, then its surface potential distribution was mapped again as presented in **Figure 5-11(d)**. The surface distribution was apparently changed to a more negative state by the tape-peeling treatments. After that, the output voltage of the TE-KEH based on this FEP film was measured again and shown in **Figure 5-11(e)**. It's clear that the output voltage of the TE-KEH was increased by the tape-peeling treatment by comparing **Figure 5-11(b) and (e)**. Finally, the surface potential distribution of the FEP film was mapped again as presented in **Figure 5-11(f)**. The general shape of potential distribution in **Figure 5-11(d) and (f)** also kept similar. The average surface potentials of the FEP film corresponding to the maps in **Figure 5-11(a), (c), (d), and (f)** are plotted in **Figure 5-12(b)**. The absolute average surface potential of the FEP film was slightly increased after the first linear motor test, then had a more obvious increase by tape-peeling, finally kept almost unchanged after the second linear motor test.

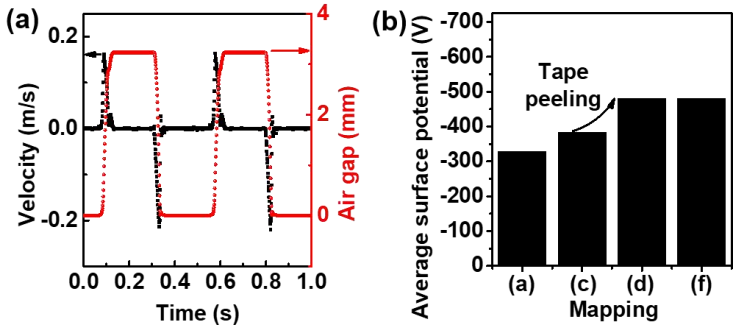

Figure 5-12 (a) The time-dependent movement velocity of the sliding block and the time-dependent air gap during the linear motor test. (b) The average surface potential values corresponding to the mapping images in Figure 3-15.

These surface potential mapping results confirm that the tape-peeling tribo-charging is an effective method to charge the FEP film with negative charges to get higher output voltage from the FEP film-based TE-KEH. The contact electrification

between the FEP film and Al foil could also charge the FEP film with negative charges, but the tape-peeling method has a greater influence on the surface potential distribution of the FEP film, which may be due to that the adhesive tape has better microscale contact with the FEP film than the Al foil.

5.4.3 Demonstration of harvesting energy from wind and human motions

To be more practical, the TE-KEH should be able to harvest energy from motions in the environment. Since the 100 μm-thick FEP film is very flexible, it can be driven by the wind to flutter, making the FEP film-based TE-KEH be able to generate electricity from the wind. **Figure 5- 13(a)** shows the photograph of the wind-driven TE-KEH made with a ~8 cm × 8 cm sized FEP film and the diagram illustrating its working process.

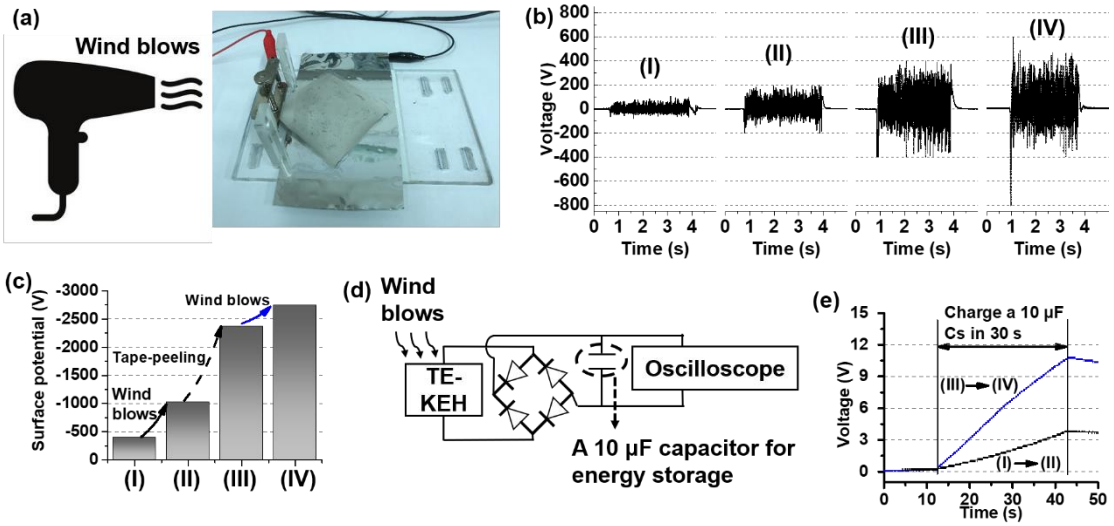

Figure 5- 13 (a) The wind-driven TE-KEH made with an ~8 cm × 8 cm sized FEP film. (b) Output voltages of the TE-KEH with FEP film holding different surface potentials. (c) Measured surface potentials of the FEP film corresponding to the output voltages in (b). (d) The circuit diagram of the TE-KEH driven by the wind to charge a capacitor. (e) Charging curves of the capacitor charged by the TE-KEH before and after tape treatment.

To fabricate the wind-driven TE-KEH, one side of the FEP film was metalized with silver paint, also with margins of ~2 mm in each edge, an Al foil was pasted on an acrylic plate, and then the FEP film was fixed upon the Al foil at one corner by a metal clamp, with non-metalized side faced with the Al foil. The FEP film contacted with the Al foil except that there was a slit of ~3mm between the FEP film and the Al

foil at the fixed corner. The TE-KEH was driven by the wind from a hairdryer for demonstration, with a wind speed of ~18m/s. The wind blew through the slit between the FEP film and the Al foil, making the FEP film flutter irregularly and flap the Al foil continuously. The flutter of the FEP film made the capacitance between the FEP film and the Al foil variable with time and consequently generated a time-variable potential difference between the Al foil and the back electrode of the FEP film which was measured by the oscilloscope with the 100 MΩ high-impedance probe.

Figure 5-13(b) presents the measured output voltages of the wind-driven TE-KEH. The four parts (I), (II), (III), and (IV) were measured in sequence. Among them, (I) was measured without any treatment to the surface of the FEP film, (II) was measured after the TE-KEH kept driven by wind for 30 s to charge a commercial aluminum electrolytic capacitor 10 μF capacitor through a full-wave rectifier (diagram of the electric circuit shown in **Figure 5-13(d)**), (III) was measured after the FEP film was treated twice by the tape-peeling process, and (IV) was measured after the TE-KEH kept working under wind blowing for another 30s to charge the 10 μF capacitor again. For each part, the output voltage obviously appeared when the wind began and disappeared when the wind stopped. Because the flutter of the FEP film was irregular, the measured voltage peak values are also irregular in each part. From (I) to (IV), the output voltage showed a gradually increasing trend. The surface potential of the FEP film before each test from (I) to (IV) was measured and presented in **Figure 5-13(c)**, which also had an increasing trend. These results reveal that the charge amount on the FEP surface can be improved not only by the tape-peeling treatment but also by the triboelectrification between the FEP film and the Al foil during the wind blowing process.

Figure 5-13(d) is the circuit diagram of the TE-KEH driven by the wind to charge a capacitor for energy storage (C_s). A rectifier bridge comprising four high voltage rectifier diodes (type IN4007) was used to convert generated irregular AC voltage output to DC output, which is essential for charging the C_s. In **Figure 5-13(e)**, the two charging curves of the 10 μF C_s during the 30s working processes of the wind-driven TE-KEH between test (I) and (V), and between test (III) and (IV) are presented. Before the tape-peeling treatment, the C_s was charged from 0V to a voltage of ~3.9 V in 30 s ((II) to (II)), corresponding to an average charging power of ~2.5 μW; after the FEP film was treated by the tape-peeling process, the C_s was charged

from 0V to 10.9 V in 30 s ((III) to (IV)), corresponding to an ~692% improvement in the average charging power to ~19.8 μW, which is enough to drive a sensor unit or other low power dissipation electronics [1, 183]. It is worthy to be noted that these average charging powers are calculated based on the energy stored in C_s. The high-impedance probe of the oscilloscope and the rectifier bridge also consume some power, so the actual average output power of the TE-KEH should higher than these C_s charging powers.

The energy loss during the rectification might be caused by the reverse current leakage of the diodes in the rectifier bridge. Sinusoidal voltage waves from a signal generator before and after rectification by the rectifier bridge is given in **Figure 5-14(a)** and **(b)** to show the voltage drop caused by rectifying. **Figure 5-14(c)** gives the no-rectified and rectified output voltages of the TE-KEH under wind blowing. The general amplitude of the voltage peaks shows a slight decrease after rectification due to energy loss. Even though, this FEP film-based TE-KEH is still capable of powering low power-consuming electronics. And it not only can harvest energy from the wind but is also able to harvest energy from low-frequency human motions. In the photograph **Figure 5-14(d)**, 42 light-emitting diodes (LEDs) were directly lighted up by the TE-KEH with a rectifier bridge when the FEP film was slightly and slowly swung by hand.

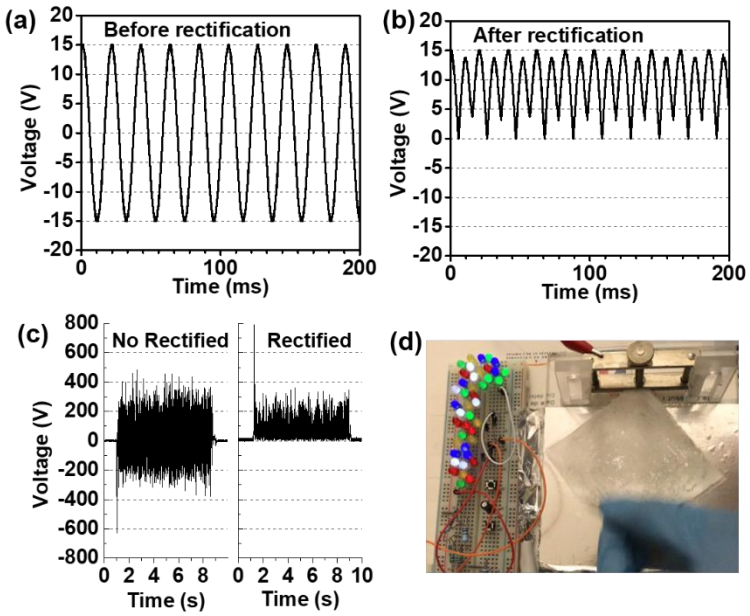

Figure 5-14 A 50 Hz sinusoidal voltage signal (a) before and (b) after rectification. (c) The output voltage of the wind-driven TE-KEH before and after

rectification. (d) 42 LEDs were directly lighted up by the hand-driven TE-KEH with the rectifier bridge.

5.5 Chapter conclusion

In this chapter, the chemical formula of the FEP film was confirmed by the FT-IR spectrum. An adhesive tape-peeling tribo-charging method was used to charge the FEP electret film used for TE-KEHs. The composition of the adhesive on the tape was identified to be butyl polyacrylate by the Raman spectrum analysis.

The surface potential of a ~4 × 4 cm^2 FEP film was improved from about -360V to about -2850V after several tape-peeling treatments. The positive out voltage peak of the TE-KEH comprised of the FEP film was correspondingly improved from 41 V to 195 V, negative peak improved from -83 V to -363 V, positive peak current density improved from 1.5 mA/m^2 to 7.3 mA/m^2, and negative peak current density improved from -1.3 mA/m^2 to -5.3 mA/m^2, in tests with the relative mechanical motion of the TE-KEH controlled by a linear motor system. The transferred charge amount of a TE-KEH made with another ~4 × 4 cm^2 FEP film were also apparently improved from ~19nC to ~53nC after several tape-peeling treatments, with corresponding positive voltage peak value increased from about 69 V to about 159 V, and the negative voltage peak value increased from about -120 V to about -365 V. The surface potential mapping of the FEP film confirmed that tape-peeling tribo-charging method could effectively charge the FEP film with negative charges, and it had more apparent influence on the surface potential distribution of the FEP film than the triboelectrification between the FEP film and Al foil during the linear motor test.

Moreover, a TE-KEH made with an 8 × 8 cm^2 FEP film was driven by the wind from a hairdryer with a wind speed of ~18m/s to charge a 10μF capacitor for energy harvesting and storage demonstration. Before the tape-peeling treatment, the wind-driven TE-KEH can charge the 10μF capacitor from 0 to 3.9 V in 30 s, corresponding to an average charging power of ~2.5μW; after the tape-peeling treatment, the same capacitor was charged by the TE-KEH from 0V to 10.9 V in 30 s, corresponding to an ~692% improvement in the average charging power to ~19.8μW. In addition, when the FEP film was slightly waved by hand, the TE-KEH was able to light up 42 LEDs. These demonstrations revealed potential applications of this miniature TE-KEH

prototype in harvesting energy from irregular mechanical motions to power low power-consuming electronics.

Chapter 6 General conclusions and perspectives

6.1 General conclusions

Firstly, the reason for the amplitude-variable output characteristics of contact-separation (CS) mode electret kinetic energy harvesters (E-KEHs) with load resistances during transitory working cycles is attributed to the lag of the charge-transfer cycle to the driving motion cycle, based on simulated and experimental output data of a CS mode tribo-electret KEH (TE-KEH) made with PTFE film with different load resistances and initial working conditions.

Secondly, the optimization of the contact time to improve the output power and efficiency of a CS mode TE-KEH with large resistive load was proved to be effective with both experimental and simulation results, the maximum theoretical output energy per working cycle of the TE-KEH with resistive loads was deduced from a series-connected switch-controlled working cycle, and the tribo-charging method and the optimization of the maximum air gap were also used to improve the output power of the TE-KEH. With these optimizations, the average output power of the CS mode TE-KEH made with a 4 cm × 4 cm sized 55 μm-thick PTFE film to the load resistance of 100 MΩ was improved from ~150 μW to ~503 μW, under a driving motion with frequency of ~8.62 Hz and with a maximum air gap of ~0.87 mm.

Thirdly, via a novel tape-peeling tribo-charging method, the output voltage and current of 4 cm × 4 cm sized TE-KEH made with 100 μm-thick FEP film was apparently increased, and the average output power of a wind-driven flexible TE-KEH prototype made with 8 cm × 8 cm sized and 100 μm-thick FEP film to charge a 10μF capacitor was improved from ~2.5 μW to ~19.8 μW. The capability of this TE-KEH prototype to harvest energy from low-frequency human motions was also demonstrated.

It is noteworthy though all these results are based on the CS mode TE-KEHs, they are also applicable to other types of E-KEHs with variable capacitance structures since they have the same basic working principle as will be discussed in section 6.2.1.

6.2 Remarks and perspectives

6.2.1 Remarks on simulations and power managements of E-KEHs

The effectiveness of the contact time optimization strategy to optimize the output power of the gap-varying E-KEHs with large load resistances had been demonstrated. In practice, there are several methods to implement this strategy, such as put the top electrode or the electret film with the back electrode on soft substrate, or use deformable low-modulus electret materials, which could prolong the effective contact time by the deformation of the substrate or electret film at the contact state. This strategy could also be applicable to other types of E-KEHs when the total electrical circuit has a relatively large time constant in comparison with the cycle period of the driving motions. However, the limitation of this strategy is that the output power of the E-KEHs is calculated by Joule's law applying to pure resistive loads. The power consumed by resistive loads can only be converted into heat, which is not practical in many applications.

For E-KEHs with complex load circuits, the analytical modeling and simulations could be complicated. Graphical modeling tools for electrical circuits, such as the SPICE and Simulink, would be very helpful to simulate the output of E-KEHs with complex load circuits and to design the power management unit for E-KEHs. A mechanic-electric coupling Simulink model for an undirect vibration-driven E-KEH with a cantilever structure had been developed by S. Boisseau, G. Despesse, and A. Sylvestre, as introduced in section 2.3.5.2. For direct motion-driven E-KEHs, modeling and simulations based on SPICE software had been demonstrated by Niu et al. [184] and R. Hinchet et al. [35]. More broadly speaking, the utilization of SPICE software and Simulink for simulations of microelectromechanical systems was demonstrated by Gary Keith Fedder in 1994 [149] based on the lumped-parameter modeling, as introduced in section 2.3.5.3.

Therefore, besides the analytical modeling in this thesis, a Simulink model for the direct motion-driven E-KEH was also established as shown in **Figure 6-1**, with a series-connected LRC load in the circuit, which however will not be discussed in detail in this thesis.

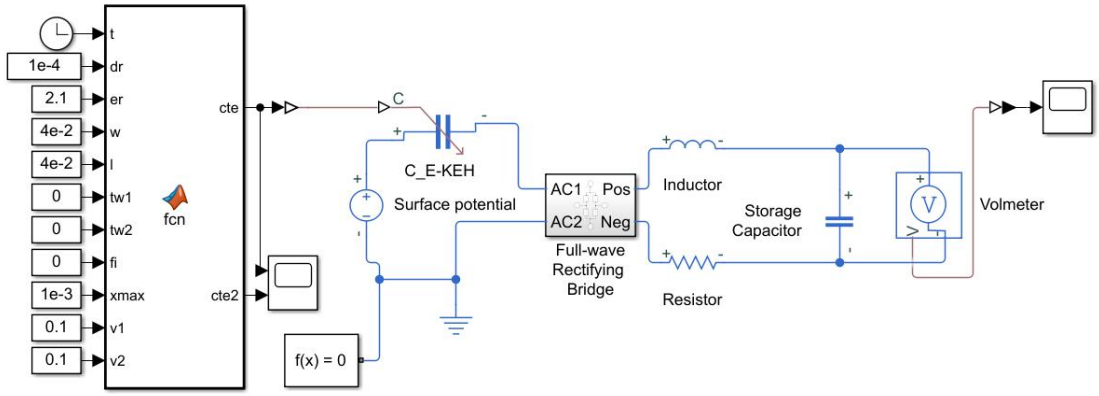

Figure 6- 1 The Simulink model for E-KEHs with a series-connected LRC load.

In fact, three aspects of key information to simulate the performance of E-KEHs are the time-varying capacitance of the E-KEHs, the effective surface charge density (or the surface potential) of the electret layer, and the configuration of the load circuit. If the information for all these three aspects is totally known, the simulation of E-KEHs would become just the electrical circuit simulation problem whatever the structure of the E-KEH is.

The time-varying capacitance can be recorded with an LCR meter with enough sampling speed or measured with a two-channel voltage recorder together with an alternative current (AC) voltage source with enough frequency range in comparison with the expected driving motion frequency [35, 132, 185].

The effective surface charge density or surface potential of the electret film can be measured by the method we used (termed as the dynamic capacitor method [46]), or by other methods such as the dissectible capacitor method, the capacitive probe method, the compensation method, the thermal-pulse method, and the polarization and depolarization current method. These methods were reviewed in the book *Electrets* by G. M. Sessler et al [46]. Nowadays, the most widely used surface potential measurement method is the compensation method with the help of commercialized electrostatic voltmeters [35, 44, 88].

The configuration of the load circuit depends on the specific application scenario of E-KEHs. Not only the power-consuming circuit but also the circuit of possible power management unit for E-KEHs in practical applications should be taken into consideration. The configuration of the load circuit has a significant influence on the effective output power of E-KEHs, that's why power management units to modulate

the output characteristics of E-KEHs are important and sometimes necessary. Typical power management units for E-KEHs include full-wave [112, 184, 186-188] or half-wave[189, 190] rectifying circuits with energy storage or buffer capacitors and with possible transformer [191] or voltage comparator[192], charge pump or voltage multiplier or bennet's doubler circuits [45, 190] as introduced in section 1.2.3, and integrated commercial power management circuits [129, 193].

6.2.2 Future work

E-KEHs are quite application-specific devices. In practical energy harvesting cases, E-KEHs should be designed according to the driving motion characteristics including the motion amplitude and frequency distribution, the circuit characteristics including the power demand of the electric load, and other specific considerations such as the cost, the eco-friendly, the fabrication technique, the matching power management circuit, and the expected service life-time, as illustrated in **Figure 6-2**. Though the basic working principle of E-KEHs is easy to understand, and prototypes of E-KEHs are facile to fabricate and investigate in labs, the successful design, fabrication, and widespread applications of E-KEHs need cooperation of experts from multiple disciplines [128, 194].

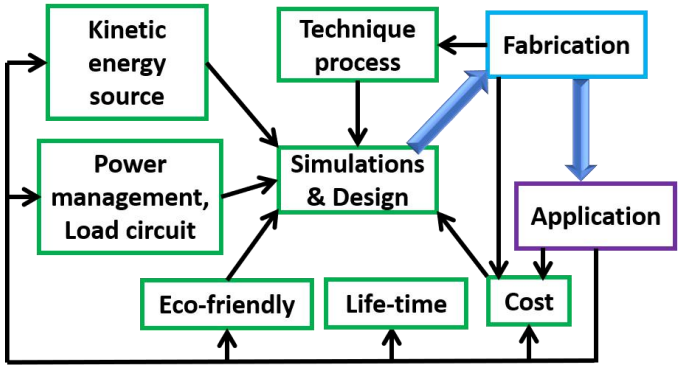

Figure 6-2 Comprehensive considerations on the design, fabrication, and application of E-KEHs.

In the future, with specifying the application scenario, the following works related to this thesis could be interesting to construct systems powered by E-KEHs with high efficiencies:

1. Data acquisition and analysis of the motion/vibration amplitude and frequency spectra in the aimed application environment of the E-KEHs-powered systems.

2. To design the specific geometric structure of E-KEHs according to features of the motion/vibration source in the environment and the power demand of the system.
3. Preparation of electret layers using amorphous fluoropolymer resins with high and stable effective surface charge density by multiple charging methods.
4. Measurement of the time-varying capacitance of the E-KEHs working in the application environment, and the impedance spectra of the electric load of the system.
5. To simulate the output of the E-KEHs based on the measured time-varying capacitance data, the effective surface charge density of the electret layers, and the impedance spectra of the electric load. To design or choose appropriate power management units with the help of the simulation method and verify their effectiveness by measured data.

References

[1] P.D. Mitcheson, E.M. Yeatman, G.K. Rao, A.S. Holmes, T.C. Green, Energy harvesting from human and machine motion for wireless electronic devices, Proceedings of the IEEE, 96 (2008) 1457-1486. https://doi.org/10.1109/JPROC.2008.927494

[2] S. Roundy, Energy scavenging for wireless sensor nodes with a focus on vibration to electricity conversion, 2003, Ph.D. thesis.

[3] F.G. Dell'Anna, T. Dong, P. Li, Y. Wen, Z. Yang, M.R. Casu, M. Azadmehr, Y. Berg, State-of-the-art power management circuits for piezoelectric energy harvesters, IEEE Circuits and Systems Magazine, 18 (2018) 27-48. https://doi.org/10.1109/MCAS.2018.2849262

[4] Z.L. Wang, L. Lin, J. Chen, S. Niu, Y. Zi, *Triboelectric nanogenerators*, Springer, 2016.

[5] S. Boisseau, G. Despesse, B.A. Seddik, *Electrostatic conversion for vibration energy harvesting*, in: M. Lallart (Ed.) *Small-scale energy harvesting*, IntechOpen, 2012.

[6] S. Cao, J. Li, A survey on ambient energy sources and harvesting methods for structural health monitoring applications, Advances in Mechanical Engineering, 9 (2017) 1687814017696210. https://doi.org/10.1177/1687814017696210

[7] https://en.wikipedia.org/wiki/Kinetic_energy_recovery_system, 28th Oct., 2019

[8] E.C. Jordan, K.G. Balmain, *Electromagnetic waves and radiating systems*, Prentice Hall, 1968.

[9] O. Brand, G.K. Fedder, C. Hierold, J.G. Korvink, O. Tabata, *Micro energy harvesting*, John Wiley & Sons, 2015.

[10] https://new.siemens.com/global/en/products/energy/power-generation/generators.html, 23th Oct, 2019

[11] D. Zhu, S. Roberts, T. Mouille, M.J. Tudor, S.P. Beeby, General model with experimental validation of electrical resonant frequency tuning of electromagnetic vibration energy harvesters, Smart Materials and Structures, 21 (2012) 105039. https://doi.org/10.1088/0964-1726/21/10/105039

[12] I. Sari, T. Balkan, H. Kulah, An electromagnetic micro power generator for wideband environmental vibrations, Sensors and Actuators A: Physical, 145-146 (2008) 405-413. https://doi.org/10.1016/j.sna.2007.11.021

[13] M.A. Halim, H. Cho, J.Y. Park, Design and experiment of a human-limb driven, frequency up-converted electromagnetic energy harvester, Energy Conversion and Management, 106 (2015) 393-404. https://doi.org/10.1016/j.enconman.2015.09.065

[14] B.J. Bowers, D.P. Arnold, Spherical, rolling magnet generators for passive energy harvesting from human motion, Journal of Micromechanics and Microengineering, 19 (2009) 094008. https://doi.org/10.1088/0960-1317/19/9/094008

[15] H. Liu, Y. Qian, C. Lee, A multi-frequency vibration-based MEMS electromagnetic energy harvesting device, Sensors and Actuators A: Physical, 204 (2013) 37-43. https://doi.org/10.1016/j.sna.2013.09.015

[16] H.C. Liu, J.W. Zhong, C. Lee, S.W. Lee, L.W. Lin, A comprehensive review on piezoelectric energy harvesting technology: Materials, mechanisms, and applications, Applied Physics Reviews, 5 (2018) 041306. https://doi.org/10.1063/1.5074184

[17] G.-T. Hwang, V. Annapureddy, J.H. Han, D.J. Joe, C. Baek, D.Y. Park, D.H. Kim, J.H. Park, C.K. Jeong, K.-I. Park, J.-J. Choi, D.K. Kim, J. Ryu, K.J. Lee, Self-powered wireless sensor node enabled by an aerosol-deposited pzt flexible energy harvester, Advanced Energy Materials, 6 (2016) 1600237. https://doi.org/10.1002/aenm.201600237

[18] M. Geisler, Human mechanical energy harvesting systems for smart clothes, 2017, Ph.D. thesis.

[19] N.S. Shenck, J.A. Paradiso, Energy scavenging with shoe-mounted piezoelectrics, IEEE Micro, 21 (2001) 30-42. https://doi.org/10.1109/40.928763

[20] H. Liu, C. Lee, T. Kobayashi, C.J. Tay, C. Quan, Piezoelectric mems-based wideband energy harvesting systems using a frequency-up-conversion cantilever stopper, Sensors and Actuators A: Physical, 186 (2012) 242-248. https://doi.org/10.1016/j.sna.2012.01.033

[21] Z.L. Wang, J. Song, Piezoelectric nanogenerators based on zinc oxide nanowire arrays, Science, 312 (2006) 242-246. https://doi.org/10.1126/science.1124005

[22] Y. Hu, Y. Zhang, C. Xu, L. Lin, R.L. Snyder, Z.L. Wang, Self-powered system with wireless data transmission, Nano Letters, 11 (2011) 2572-2577. https://doi.org/10.1021/nl201505c

[23] C. Chang, V.H. Tran, J. Wang, Y.-K. Fuh, L. Lin, Direct-write piezoelectric polymeric nanogenerator with high energy conversion efficiency, Nano Letters, 10 (2010) 726-731. https://doi.org/10.1021/nl9040719

[24] X. Wang, J. Song, J. Liu, Z.L. Wang, Direct-current nanogenerator driven by ultrasonic waves, Science, 316 (2007) 102-105. https://doi.org/10.1126/science.1139366

[25] P.D. Mitcheson, T. Sterken, C. He, M. Kiziroglou, E.M. Yeatman, R. Puers, Electrostatic microgenerators, Measurement and Control, 41 (2008) 114-119. https://doi.org/10.1177/002029400804100404

[26] S. Meninger, J.O. Mur-Miranda, R. Amirtharajah, A. Chandrakasan, J.H. Lang, Vibration-to-electric energy conversion, IEEE Transactions on Very Large Scale Integration (VLSI) Systems, 9 (2001) 64-76. https://doi.org/10.1109/92.920820

[27] D. Galayko, A. Dudka, A. Karami, E.O. Riordan, E. Blokhina, O. Feely, P. Basset, Capacitive energy conversion with circuits implementing a rectangular charge-voltage cycle—part 1: Analysis of the electrical domain, IEEE Transactions on Circuits and Systems I: Regular Papers, 62 (2015) 2652-2663. https://doi.org/10.1109/TCSI.2015.2451911

[28] S. Roundy, P. Wright, K. Pister, Micro-electrostatic vibration-to-electricity converters, Proceedings of ASME IMECE (2002), New Orleans, Louisiana, USA, 487-496. https://doi.org/10.1115/IMECE2002-39309

[29] L. Xu, T.Z. Bu, X.D. Yang, C. Zhang, Z.L. Wang, Ultrahigh charge density realized by charge pumping at ambient conditions for triboelectric nanogenerators, Nano Energy, 49 (2018) 625-633. https://doi.org/10.1016/j.nanoen.2018.05.011

[30] A. Karami, D. Galayko, P. Basset, Series-parallel charge pump conditioning circuits for electrostatic kinetic energy harvesting, IEEE Transactions on Circuits and Systems I: Regular Papers, 64 (2017) 227-240. https://doi.org/10.1109/TCSI.2016.2603064

[31] A. Ghaffarinejad, Y. Lu, R. Hinchet, D. Galayko, J.Y. Hasani, P. Basset, Bennet's charge doubler boosting triboelectric kinetic energy harvesters, Journal of Physics: Conference Series, 1052 (2018) 012027. https://doi.org/10.1088/1742-6596/1052/1/012027

[32] M.A.B. Ouanes, Y. Lu, H. Samaali, P. Basset, F. Najar, Design and test of a bennet's doubler device with mechanical switches for vibrational energy harvesting, Journal of Physics: Conference Series, 773 (2016) 012038. 10.1088/1742-6596/773/1/012038

[33] E. Lefeuvre, S. Risquez, J. Wei, M. Woytasik, F. Parrain, Self-biased inductor-less interface circuit for electret-free electrostatic energy harvesters, Journal of Physics: Conference Series, 557 (2014) 012052. https://doi.org/10.1088/1742-6596/557/1/012052

[34] J. Wei, S. Risquez, H. Mathias, E. Lefeuvre, F. Costa, Simple and efficient interface circuit for vibration electrostatic energy harvesters, Proceedings of 2015 IEEE SENSORS (2015), Busan, South Korea, 1-4. https://doi.org/10.1109/ICSENS.2015.7370637

[35] R. Hinchet, A. Ghaffarinejad, Y. Lu, J.Y. Hasani, S.-W. Kim, P. Basset, Understanding and modeling of triboelectric-electret nanogenerator, Nano Energy, 47 (2018) 401-409. https://doi.org/10.1016/j.nanoen.2018.02.030

[36] H. Zhang, S. Feng, D. He, P. Molinié, J. Bai, Amplitude-variable output characteristics of triboelectric-electret nanogenerators during multiple working cycles, Nano Energy, (2019) 103856. https://doi.org/10.1016/j.nanoen.2019.103856

[37] P. Basset, D. Galayko, A.M. Paracha, F. Marty, A. Dudka, T. Bourouina, A batch-fabricated and electret-free silicon electrostatic vibration energy harvester, Journal of Micromechanics and Microengineering, 19 (2009) 115025. https://doi.org/10.1088/0960-1317/19/11/115025

[38] P. Basset, D. Galayko, F. Cottone, R. Guillemet, E. Blokhina, F. Marty, T. Bourouina, Electrostatic vibration energy harvester with combined effect of electrical nonlinearities and mechanical impact, Journal of Micromechanics and Microengineering, 24 (2014) 035001. https://doi.org/10.1088/0960-1317/24/3/035001

[39] V. Bogdan, A. Denis, G. Philippe, R. Xavier Le, P. Fabien, L. Elie, Nonlinear electrostatic energy harvester using compensational springs in gravity field,

Journal of Micromechanics and Microengineering, 28 (2018) 074004. https://doi.org/10.1088/1361-6439/aabc90

[40] S. Chiba, M. Waki, R. Kornbluh, R. Pelrine, Innovative power generators for energy harvesting using electroactive polymer artificial muscles, Proceedings of The 15th International Symposium on: Smart Structures and Materials & Nondestructive Evaluation and Health Monitoring (2008), 692715-692715-692719.

[41] R. Tashiro, N. Kabei, K. Katayama, E. Tsuboi, K. Tsuchiya, Development of an electrostatic generator for a cardiac pacemaker that harnesses the ventricular wall motion, Journal of Artificial Organs, 5 (2002) 0239-0245. https://doi.org/10.1007/s100470200045

[42] T. Vu-Cong, C. Jean-Mistral, A. Sylvestre, Autonomous dielectric elastomer generator using electret, Electroactive Polymer Actuators And Devices (Eapad) 2013, 8687 (2013). https://doi.org/10.1117/12.2008793

[43] R. Pelrine, R.D. Kornbluh, J. Eckerle, P. Jeuck, S. Oh, Q. Pei, S. Stanford, Dielectric elastomers: Generator mode fundamentals and applications, Proceedings of SPIE (2001), 4329, Smart Structures and Materials 2001: Electroactive Polymer Actuators and Devices, Newport Beach, USA, 148-156.

[44] T. Vu-Cong, C. Jean-Mistral, A. Sylvestre, Electrets substituting external bias voltage in dielectric elastomer generators: Application to human motion, Smart Materials and Structures, 22 (2013) 025012. https://doi.org/10.1088/0964-1726/22/2/025012

[45] C. Jean-Mistral, T. Vu-Cong, A. Sylvestre, On the power management and electret hybridization of dielectric elastomer generators, Smart Materials and Structures, 22 (2013) 104017. https://doi.org/10.1088/0964-1726/22/10/104017

[46] G.M. Sessler, *Electrets*, Springer-Verlag Berlin Heidelberg, 1987.

[47] H. Oliver, *Electrical papers, vol. 1*, London, Macmillan and Co and New York, 1892.

[48] M. Eguchi, On dielectric polarisation, Proceedings of the Physico-Mathematical Society of Japan. 3rd Series, 1 (1919) 326-331. https://doi.org/10.11429/ppmsj1919.1.10-11_326

[49] H.S. Nalwa, *Ferroelectric polymers: Chemistry, physics, and applications*, CRC Press, 1995.

[50] K.C. Kao, *5 - electrets*, in: K.C. Kao (Ed.) *Dielectric phenomena in solids*, Academic Press, San Diego, 2004, pp. 283-326.

[51] S.S. Bamji, Superior electrets of polychlorotrifluoroethylene (aclar), Journal of Physics D: Applied Physics, 15 (1982) 911. https://doi.org/10.1088/0022-3727/15/5/019

[52] M.É. Borisova, S.N. Koikov, Electret effect in dielectrics, Soviet Physics Journal, 22 (1979) 58-69. https://doi.org/10.1007/BF00890543

[53] Z.L. Wang, A.C. Wang, On the origin of contact-electrification, Materials Today, 30 (2019). https://doi.org/10.1016/j.mattod.2019.05.016

[54] K.C. Kao, *1 - introduction*, in: K.C. Kao (Ed.) *Dielectric phenomena in solids*, Academic Press, San Diego, 2004, pp. 1-39.

[55] L.S. McCarty, A. Winkleman, G.M. Whitesides, Electrostatic self-assembly of polystyrene microspheres by using chemically directed contact electrification, Angewandte Chemie International Edition, 46 (2007) 206-209. https://doi.org/10.1002/anie.200602914

[56] H. Zou, Y. Zhang, L. Guo, P. Wang, X. He, G. Dai, H. Zheng, C. Chen, A.C. Wang, C. Xu, Z.L. Wang, Quantifying the triboelectric series, Nature Communications, 10 (2019) 1427. https://doi.org/10.1038/s41467-019-09461-x

[57] https://en.wikipedia.org/wiki/Electrostatic_induction, 21st Oct., 2019

[58] G.M. Sessler, J.E. West, Electret transducers: A review, The Journal of the Acoustical Society of America, 53 (1973) 1589-1600. https://doi.org/10.1121/1.1913507

[59] G.M. Sessler, J.E. West, Self‐biased condenser microphone with high capacitance, The Journal of the Acoustical Society of America, 34 (1962) 1787-1788. https://doi.org/10.1121/1.1909130

[60] G.M. Sessler, Electrostatic microphones with electret foil, The Journal of the Acoustical Society of America, 35 (1963) 1354-1357. https://doi.org/10.1121/1.1918697

[61] G.M. Sessler, J.E. West, Electrostatic microphones with foil electret, Proceedings of the 5th International Congresses on Acoustics (1965), Liege. Paper J42

[62] R.B. Basham, Flexible force responsive transducer, United States 3,996,922, Dec. 14, 1976

[63] O.D. Jefimenko, D.K. Walker, Electrostatic current generator having a disk electret as an active element, IEEE Transactions on Industry Applications, IA-14 (1978) 537-540. https://doi.org/10.1109/TIA.1978.4503588

[64] Y. Tada, Experimental characteristics of electret generator, using polymer film electrets, Japanese Journal Of Applied Physics, 31 (1992) 846-851. https://doi.org/10.1143/jjap.31.846

[65] S. Boisseau, G. Despesse, A. Sylvestre, Optimization of an electret-based energy harvester, Smart Materials and Structures, 19 (2010) 075015. https://doi.org/10.1088/0964-1726/19/7/075015

[66] Y. Tada, Theoretical characteristics of generalized electret generator, using polymer film electrets, IEEE Transactions on Electrical Insulation, EI-21 (1986) 457-464. https://doi.org/10.1109/TEI.1986.349093

[67] Y. Arakawa, Y. Suzuki, N. Kasagi, Micro seismic power generator using electret polymer film, Proc. PowerMEMS, (2004) 187-190. https://doi.org/10.1299/jsmepes.2004.9.37

[68] H.-w. Lo, Y.-C. Tai, Parylene-based electret power generators, Journal of Micromechanics and Microengineering, 18 (2008) 104006. https://doi.org/10.1088/0960-1317/18/10/104006

[69] J. Boland, Y.-C. Tai, Electret generator apparatus and method, United States US 2004/0007877 A1, Jan. 15, 2004

[70] F.R. Fan, Z.Q. Tian, Z.L. Wang, Flexible triboelectric generator!, Nano Energy, 1 (2012) 328-334. https://doi.org/10.1016/j.nanoen.2012.01.004

[71] G.M. Sessler, J. Hillenbrand, Electromechanical response of cellular electret films, Applied Physics Letters, 75 (1999) 3405-3407. https://doi.org/10.1063/1.125308

[72] J.S. Boland, J.D.M. Messenger, K.W. Lo, Y.C. Tai, Arrayed liquid rotor electret power generator systems, Proceedings of 18th IEEE International Conference on Micro Electro Mechanical Systems, 2005. MEMS 2005. (2005), 618-621. https://doi.org/10.1109/MEMSYS.2005.1454005

[73] T. Gray, *Projected capacitive touch: A practical guide for engineers*, Springer, 2018.

[74] P. Basset, E. Blokhina, D. Galayko, *Electrostatic kinetic energy harvesting*, John Wiley & Sons, 2016.

[75] S. Bauer, R. Gerhard-Multhaupt, G.M. Sessler, Ferroelectrets: Soft electroactive foams for transducers, Physics Today, 57 (2004) 37-43. https://doi.org/10.1063/1.1688068

[76] R. Gerhard-Multhaupt, Less can be more - holes in polymers lead to a new paradigm of piezoelectric materials for electret transducers, Ieee Transactions on Dielectrics And Electrical Insulation, 9 (2002) 850-859. https://doi.org/10.1109/tdei.2002.1038668

[77] R. Altafim, H. Basso, R. Altafim, L. Lima, C. de Aquino, L.G. Neto, R. Gerhard-Multhaupt, Piezoelectrets from thermo-formed bubble structures of fluoropolymer-electret films, Ieee Transactions on Dielectrics And Electrical Insulation, 13 (2006) 979-985. https://doi.org/10.1109/TDEI.2006.247822

[78] N. Wu, X. Cheng, Q. Zhong, J. Zhong, W. Li, B. Wang, B. Hu, J. Zhou, Cellular polypropylene piezoelectret for human body energy harvesting and health monitoring, Advanced Functional Materials, 25 (2015) 4788-4794. https://doi.org/10.1002/adfm.201501695

[79] A. Kachroudi, S. Basrour, L. Rufer, A. Sylvestre, F. Jomni, Micro-structured pdms piezoelectric enhancement through charging conditions, Smart Materials and Structures, 25 (2016). https://doi.org/10.1088/0964-1726/25/10/105027

[80] J.-J. Wang, H.-Y. Liang, W. Fang, Y.-C. Su, Composite rubber electret with piezoelectric 31 and 33 modes for elastically electromechanical sensors, Proceedings of SENSORS, 2015 IEEE (2015), 1-4.

[81] A. Mohebbi, F. Mighri, A. Ajji, D. Rodrigue, Cellular polymer ferroelectret: A review on their development and their piezoelectric properties, Advances in Polymer Technology, 37 (2018) 468-483. https://doi.org/10.1002/adv.21686

[82] F.-R. Fan, L. Lin, G. Zhu, W. Wu, R. Zhang, Z.L. Wang, Transparent triboelectric nanogenerators and self-powered pressure sensors based on micropatterned plastic films, Nano Letters, 12 (2012) 3109-3114. https://doi.org/10.1021/nl300988z

[83] Z.L. Wang, Triboelectric nanogenerators as new energy technology for self-powered systems and as active mechanical and chemical sensors, ACS Nano, 7 (2013) 9533-9557. https://doi.org/10.1021/nn404614z

[84] T. Cheng, Q. Gao, Z.L. Wang, The current development and future outlook of triboelectric nanogenerators: A survey of literature, Advanced Materials Technologies, 4 (2019) 1800588. https://doi.org/10.1002/admt.201800588

[85] B.D. Chen, W. Tang, C. Zhang, L. Xu, L.P. Zhu, L.J. Yang, C. He, J. Chen, L. Liu, T. Zhou, Z.L. Wang, Au nanocomposite enhanced electret film for triboelectric nanogenerator, Nano Research, (2017). https://doi.org/10.1007/s12274-017-1716-y

[86] Y. Yang, H. Zhang, X. Zhong, F. Yi, R. Yu, Y. Zhang, Z.L. Wang, Electret film-enhanced triboelectric nanogenerator matrix for self-powered instantaneous tactile imaging, ACS Applied Materials & Interfaces, 6 (2014) 3680-3688. https://doi.org/10.1021/am406018h

[87] H. Zhang, S. Feng, D. He, Y. Xu, M. Yang, J. Bai, An electret film-based triboelectric nanogenerator with largely improved performance via a tape-peeling charging method, Nano Energy, 48 (2018) 256-265. https://doi.org/10.1016/j.nanoen.2018.03.051

[88] T. Zhou, L. Zhang, F. Xue, W. Tang, C. Zhang, Z.L. Wang, Multilayered electret films based triboelectric nanogenerator, Nano Research, 9 (2016) 1442-1451. https://doi.org/10.1007/s12274-016-1040-y

[89] L.M. Zhang, C.B. Han, T. Jiang, T. Zhou, X.H. Li, C. Zhang, Z.L. Wang, Multilayer wavy-structured robust triboelectric nanogenerator for harvesting water wave energy, Nano Energy, 22 (2016) 87-94. https://doi.org/10.1016/j.nanoen.2016.01.009

[90] S. Wang, Y. Xie, S. Niu, L. Lin, C. Liu, Y.S. Zhou, Z.L. Wang, Maximum surface charge density for triboelectric nanogenerators achieved by ionized‐air injection: Methodology and theoretical understanding, Advanced Materials, 26 (2014) 6720-6728. https://doi.org/10.1002/adma.201402491

[91] Y. Zi, S. Niu, J. Wang, Z. Wen, W. Tang, Z.L. Wang, Standards and figure-of-merits for quantifying the performance of triboelectric nanogenerators, Nature Communications, 6 (2015) 8376. https://doi.org/10.1038/ncomms9376

[92] Z.L. Wang, Triboelectric nanogenerators as new energy technology and self-powered sensors–principles, problems and perspectives, Faraday Discussions, 176 (2015) 447-458. https://doi.org/10.1039/C4FD00159A

[93] Y. Yang, Y.S. Zhou, H. Zhang, Y. Liu, S. Lee, Z.L. Wang, A single-electrode based triboelectric nanogenerator as self-powered tracking system, Advanced Materials, 25 (2013) 6594-6601. https://doi.org/10.1002/adma.201302453

[94] H. Zhang, Y. Yang, X. Zhong, Y. Su, Y. Zhou, C. Hu, Z.L. Wang, Single-electrode-based rotating triboelectric nanogenerator for harvesting energy from tires, ACS Nano, 8 (2014) 680-689. 10.1021/nn4053292

[95] G. Zhu, J. Chen, T. Zhang, Q. Jing, Z.L. Wang, Radial-arrayed rotary electrification for high performance triboelectric generator, Nature Communications, 5 (2014) 3426. https://doi.org/10.1038/ncomms4426

[96] P. Matthias, B. Sebastien, G. Matthias, D. Ghislain, R. Jean Luc, Triboelectret-based aeroelastic flutter energy harvesters, Journal of Physics: Conference Series, 773 (2016) 012021. https://doi.org/10.1088/1742-6596/773/1/012021

[97] J. Bae, J. Lee, S. Kim, J. Ha, B.-S. Lee, Y. Park, C. Choong, J.-B. Kim, Z.L. Wang, H.-Y. Kim, J.-J. Park, U.I. Chung, Flutter-driven triboelectrification for harvesting wind energy, Nature Communications, 5 (2014). https://doi.org/10.1038/ncomms5929

[98] Y. Yang, G. Zhu, H.L. Zhang, J. Chen, X.D. Zhong, Z.H. Lin, Y.J. Su, P. Bai, X.N. Wen, Z.L. Wang, Triboelectric nanogenerator for harvesting wind energy and as self-powered wind vector sensor system, ACS Nano, 7 (2013) 9461-9468. https://doi.org/10.1021/nn4043157

[99] X.-S. Zhang, M. Han, B. Kim, J.-F. Bao, J. Brugger, H. Zhang, All-in-one self-powered flexible microsystems based on triboelectric nanogenerators, Nano Energy, 47 (2018) 410-426. https://doi.org/10.1016/j.nanoen.2018.02.046

[100] X. Wang, Y. Zhang, X. Zhang, Z. Huo, X. Li, M. Que, Z. Peng, H. Wang, C. Pan, A highly stretchable transparent self-powered triboelectric tactile sensor with metallized nanofibers for wearable electronics, Advanced Materials, 30 (2018) 1706738. https://doi.org/10.1002/adma.201706738

[101] Y. Chen, X. Pu, M. Liu, S. Kuang, P. Zhang, Q. Hua, Z. Cong, W. Guo, W. Hu, Z.L. Wang, Shape-adaptive, self-healable triboelectric nanogenerator with enhanced performances by soft solid–solid contact electrification, ACS Nano, 13 (2019) 8936-8945. https://doi.org/10.1021/acsnano.9b02690

[102] G. Zhu, Y.S. Zhou, P. Bai, X.S. Meng, Q. Jing, J. Chen, Z.L. Wang, A shape-adaptive thin-film-based approach for 50% high-efficiency energy generation through micro-grating sliding electrification, Advanced Materials, 26 (2014) 3788-3796. https://doi.org/10.1002/adma.201400021

[103] J. Zhong, Y. Zhang, Q. Zhong, Q. Hu, B. Hu, Z.L. Wang, J. Zhou, Fiber-based generator for wearable electronics and mobile medication, ACS Nano, 8 (2014) 6273-6280. https://doi.org/10.1021/nn501732z

[104] A. Ahmed, Z. Saadatnia, I. Hassan, Y. Zi, Y. Xi, X. He, J. Zu, Z.L. Wang, Self-powered wireless sensor node enabled by a duck-shaped triboelectric nanogenerator for harvesting water wave energy, Advanced Energy Materials, 7 (2017) 1601705. https://doi.org/10.1002/aenm.201601705

[105] M. Han, X.-S. Zhang, B. Meng, W. Liu, W. Tang, X. Sun, W. Wang, H. Zhang, R-shaped hybrid nanogenerator with enhanced piezoelectricity, ACS Nano, 7 (2013) 8554-8560. https://doi.org/10.1021/nn404023v

[106] S.H. Wang, L. Lin, Z.L. Wang, Nanoscale triboelectric-effect-enabled energy conversion for sustainably powering portable electronics, Nano Letters, 12 (2012) 6339-6346. https://doi.org/10.1021/nl303573d

[107] P. Bai, G. Zhu, Y. Liu, J. Chen, Q. Jing, W. Yang, J. Ma, G. Zhang, Z.L. Wang, Cylindrical rotating triboelectric nanogenerator, ACS Nano, 7 (2013) 6361-6366. https://doi.org/10.1021/nn402491y

[108] D. Choi, S. Lee, S.M. Park, H. Cho, W. Hwang, D.S. Kim, Energy harvesting model of moving water inside a tubular system and its application of a stick-type compact triboelectric nanogenerator, Nano Research, 8 (2015) 2481-2491. https://doi.org/10.1007/s12274-015-0756-4

[109] L. Pan, J. Wang, P. Wang, R. Gao, Y.-C. Wang, X. Zhang, J.-J. Zou, Z.L. Wang, Liquid-fep-based u-tube triboelectric nanogenerator for harvesting

water-wave energy, Nano Research, 11 (2018) 4062-4073. https://doi.org/10.1007/s12274-018-1989-9

[110] Y. Su, G. Zhu, W. Yang, J. Yang, J. Chen, Q. Jing, Z. Wu, Y. Jiang, Z.L. Wang, Triboelectric sensor for self-powered tracking of object motion inside tubing, ACS Nano, 8 (2014) 3843-3850. https://doi.org/10.1021/nn500695q

[111] X. Wang, S. Niu, Y. Yin, F. Yi, Z. You, Z.L. Wang, Triboelectric nanogenerator based on fully enclosed rolling spherical structure for harvesting low-frequency water wave energy, Advanced Energy Materials, 5 (2015) 1501467. https://doi.org/10.1002/aenm.201501467

[112] L. Xu, T. Jiang, P. Lin, J.J. Shao, C. He, W. Zhong, X.Y. Chen, Z.L. Wang, Coupled triboelectric nanogenerator networks for efficient water wave energy harvesting, ACS Nano, 12 (2018) 1849-1858. https://doi.org/10.1021/acsnano.7b08674

[113] J. Chen, J. Yang, Z. Li, X. Fan, Y. Zi, Q. Jing, H. Guo, Z. Wen, K.C. Pradel, S. Niu, Z.L. Wang, Networks of triboelectric nanogenerators for harvesting water wave energy: A potential approach toward blue energy, ACS Nano, 9 (2015) 3324-3331. https://doi.org/10.1021/acsnano.5b00534

[114] Z.L. Wang, T. Jiang, L. Xu, Toward the blue energy dream by triboelectric nanogenerator networks, Nano Energy, 39 (2017) 9-23. https://doi.org/10.1016/j.nanoen.2017.06.035

[115] X. Li, J. Tao, X. Wang, J. Zhu, C. Pan, Z.L. Wang, Networks of high performance triboelectric nanogenerators based on liquid–solid interface contact electrification for harvesting low-frequency blue energy, Advanced Energy Materials, 8 (2018) 1800705. https://doi.org/10.1002/aenm.201800705

[116] Z.L. Wang, Catch wave power in floating nets, Nature, 542 (2017) 159-160. https://doi.org/10.1038/542159a

[117] M.L. Seol, J.H. Woo, S.B. Jeon, D. Kim, S.J. Park, J. Hur, Y.K. Choi, Vertically stacked thin triboelectric nanogenerator for wind energy harvesting, Nano Energy, 14 (2015) 201-208. https://doi.org/10.1016/j.nanoen.2014.11.016

[118] W. Du, X. Han, L. Lin, M. Chen, X. Li, C. Pan, Z.L. Wang, A three dimensional multi-layered sliding triboelectric nanogenerator, Advanced Energy Materials, 4 (2014) 1301592. https://doi.org/10.1002/aenm.201301592

[119] P. Bai, G. Zhu, Z.-H. Lin, Q. Jing, J. Chen, G. Zhang, J. Ma, Z.L. Wang, Integrated multilayered triboelectric nanogenerator for harvesting biomechanical energy from human motions, ACS Nano, 7 (2013) 3713-3719. https://doi.org/10.1021/nn4007708

[120] W. Tang, T. Jiang, F.R. Fan, A.F. Yu, C. Zhang, X. Cao, Z.L. Wang, Liquid-metal electrode for high-performance triboelectric nanogenerator at an instantaneous energy conversion efficiency of 70.6%, Advanced Functional Materials, 25 (2015) 3718-3725. https://doi.org/10.1002/adfm.201501331

[121] J. Chun, J.W. Kim, W.-s. Jung, C.-Y. Kang, S.-W. Kim, Z.L. Wang, J.M. Baik, Mesoporous pores impregnated with au nanoparticles as effective dielectrics for enhancing triboelectric nanogenerator performance in harsh environments, Energy & Environmental Science, 8 (2015) 3006-3012. https://doi.org/10.1039/C5EE01705J

[122] B. Yang, W. Zeng, Z.H. Peng, S.R. Liu, K. Chen, X.M. Tao, A fully verified theoretical analysis of contact - mode triboelectric nanogenerators as a wearable power source, Advanced Energy Materials, 6 (2016) 1600505. https://doi.org/10.1002/aenm.201600505

[123] G. Zhu, C. Pan, W. Guo, C.-Y. Chen, Y. Zhou, R. Yu, Z.L. Wang, Triboelectric-generator-driven pulse electrodeposition for micropatterning, Nano Letters, 12 (2012) 4960-4965. https://doi.org/10.1021/nl302560k

[124] G. Cheng, L. Zheng, Z.-H. Lin, J. Yang, Z. Du, Z.L. Wang, Multilayered-electrode-based triboelectric nanogenerators with managed output voltage and multifold enhanced charge transport, Advanced Energy Materials, 5 (2015). https://doi.org/10.1002/aenm.201401452

[125] G. Zhu, Z.-H. Lin, Q. Jing, P. Bai, C. Pan, Y. Yang, Y. Zhou, Z.L. Wang, Toward large-scale energy harvesting by a nanoparticle-enhanced triboelectric nanogenerator, Nano Letters, 13 (2013) 847-853. https://doi.org/10.1021/nl4001053

[126] C. Park, G. Song, S.M. Cho, J. Chung, Y. Lee, E.H. Kim, M. Kim, S. Lee, J. Huh, C. Park, Supramolecular-assembled nanoporous film with switchable metal salts for a triboelectric nanogenerator, Advanced Functional Materials, 27 (2017) 1701367. https://doi.org/10.1002/adfm.201701367

[127] Z. Saadatnia, S.G. Mosanenzadeh, E. Esmailzadeh, H.E. Naguib, A high performance triboelectric nanogenerator using porous polyimide aerogel film, Scientific Reports, 9 (2019) 1370. https://doi.org/10.1038/s41598-018-38121-1

[128] X. Li, G. Xu, X. Xia, J. Fu, L. Huang, Y. Zi, Standardization of triboelectric nanogenerators: Progress and perspectives, Nano Energy, 56 (2019) 40-55. https://doi.org/10.1016/j.nanoen.2018.11.029

[129] A. Ahmed, I. Hassan, M.F. El-Kady, A. Radhi, C.K. Jeong, P.R. Selvaganapathy, J. Zu, S. Ren, Q. Wang, R.B. Kaner, Integrated triboelectric nanogenerators in the era of the internet of things, Advanced Science, 1802230. https://doi.org/10.1002/advs.201802230

[130] Y.N. Xie, S.H. Wang, L. Lin, Q.S. Jing, Z.H. Lin, S.M. Niu, Z.Y. Wu, Z.L. Wang, Rotary triboelectric nanogenerator based on a hybridized mechanism for harvesting wind energy, ACS Nano, 7 (2013) 7119-7125. https://doi.org/10.1021/nn402477h

[131] T. Sterken, K. Baert, R. Puers, G. Borghs, Power extraction from ambient vibration, Proceedings of SAFE-ProRISC-SeSens (2001), Veldhoven, Netherlands.

[132] Y. Lu, E. O'Riordan, F. Cottone, S. Boisseau, D. Galayko, E. Blokhina, F. Marty, P. Basset, A batch-fabricated electret-biased wideband mems vibration energy harvester with frequency-up conversion behavior powering a uhf wireless sensor node, Journal of Micromechanics and Microengineering, 26 (2016) 124004. https://doi.org/10.1088/0960-1317/26/12/124004

[133] Y. Zi, H. Guo, Z. Wen, M.-H. Yeh, C. Hu, Z.L. Wang, Harvesting low-frequency (<5 Hz) irregular mechanical energy: A possible killer application of triboelectric nanogenerator, ACS Nano, 10 (2016) 4797-4805. https://doi.org/10.1021/acsnano.6b01569

[134] F. Xing, Y. Jie, X. Cao, T. Li, N. Wang, Natural triboelectric nanogenerator based on soles for harvesting low-frequency walking energy, Nano Energy, 42 (2017) 138-142. https://doi.org/10.1016/j.nanoen.2017.10.029

[135] X.-S. Zhang, M.-D. Han, R.-X. Wang, F.-Y. Zhu, Z.-H. Li, W. Wang, H.-X. Zhang, Frequency-multiplication high-output triboelectric nanogenerator for sustainably powering biomedical microsystems, Nano Letters, 13 (2013) 1168-1172. https://doi.org/10.1021/nl3045684

[136] T. Sterken, K. Baert, R. Puers, G. Borghs, R. Mertens, A new power mems component with variable capacitance, Proceedings of Pan Pacific Microelectronics symposium (2003), 27-34.

[137] H. Kloub, D. Hoffmann, B. Folkmer, Y. Manoli, A micro capacitive vibration energy harvester for low power electronics, Proceedings of PowerMEMS 2009 (2009), Washington DC, USA, 165-168. http://cap.ee.ic.ac.uk/~pdm97/powermems/2009/pdfs/papers/044_0058.pdf

[138] S. Niu, Y. Liu, X. Chen, S. Wang, Y.S. Zhou, L. Lin, Y. Xie, Z.L. Wang, Theory of freestanding triboelectric-layer-based nanogenerators, Nano Energy, 12 (2015) 760-774. https://doi.org/10.1016/j.nanoen.2015.01.013

[139] E. Blokhina, A. El Aroudi, E. Alarcon, D. Galayko, *Nonlinearity in energy harvesting systems*, Springer, 2016.

[140] C.B. Williams, R.B. Yates, Analysis of a micro-electric generator for microsystems, Proceedings of the International Solid-State Sensors and Actuators Conference - TRANSDUCERS '95 (1995), 1, 369-372. https://doi.org/10.1109/SENSOR.1995.717207

[141] C.B. Williams, R.B. Yates, Analysis of a micro-electric generator for microsystems, Sensors and Actuators A: Physical, 52 (1996) 8-11. https://doi.org/10.1016/0924-4247(96)80118-X

[142] P.D. Mitcheson, T.C. Green, E.M. Yeatman, A.S. Holmes, Architectures for vibration-driven micropower generators, Journal Of Microelectromechanical Systems, 13 (2004) 429-440. https://doi.org/10.1109/JMEMS.2004.830151

[143] W.J. Li, T.C.H. Ho, G.M.H. Chan, P.H.W. Leong, W. Hiu Yung, Infrared signal transmission by a laser-micromachined, vibration-induced power generator, Proceedings of the 43rd IEEE Midwest Symposium on Circuits and Systems (Cat.No.CH37144) (2000), 1, 236-239. https://doi.org/10.1109/MWSCAS.2000.951628

[144] C.B. Williams, C. Shearwood, M.A. Harradine, P.H. Mellor, T.S. Birch, R.B. Yates, Development of an electromagnetic micro-generator, IEE Proceedings - Circuits, Devices and Systems, 148 (2001) 337-342. https://doi.org/10.1049/ip-cds:20010525

[145] R. Amirtharajah, A.P. Chandrakasan, Self-powered signal processing using vibration-based power generation, IEEE Journal of Solid-State Circuits, 33 (1998) 687-695. https://doi.org/10.1109/4.668982

[146] S. Boisseau, G. Despesse, T. Ricart, E. Defay, A. Sylvestre, Cantilever-based electret energy harvesters, Smart Materials and Structures, 20 (2011) 105013. https://doi.org/10.1088/0964-1726/20/10/105013

[147] J. Boland, C. Yuan-Heng, Y. Suzuki, Y.C. Tai, Micro electret power generator, Proceedings of The Sixteenth Annual International Conference on Micro Electro Mechanical Systems, 2003. MEMS-03 Kyoto. IEEE (2003), 538-541. https://doi.org/10.1109/MEMSYS.2003.1189805

[148] Y. Sakane, Y. Suzuki, N. Kasagi, The development of a high-performance perfluorinated polymer electret and its application to micro power generation, Journal of Micromechanics and Microengineering, 18 (2008) 104011. https://doi.org/10.1088/0960-1317/18/10/104011

[149] G.K. Fedder, Simulation of microelectromechanical systems, 1994, Ph.D. thesis.

[150] H.A.C. Tilmans, Equivalent circuit representation of electromechanical transducers: I. Lumped-parameter systems, Journal of Micromechanics and Microengineering, 6 (1996) 157-176. https://doi.org/10.1088/0960-1317/6/1/036

[151] H.A.C. Tilmans, Erratum: Equivalent circuit representation of electromechanical transducers: I. Lumped-parameter systems, Journal of Micromechanics and Microengineering, 6 (1996) 359-359. https://doi.org/10.1088/0960-1317/6/3/009

[152] D. Galayko, P. Basset, A general analytical tool for the design of vibration energy harvesters (VEHs) based on the mechanical impedance concept, IEEE Transactions on Circuits and Systems I: Fundamental Theory and Applications, 58 (2011) 299--311. https://doi.org/10.1109/tcsi.2010.2072030

[153] S. Niu, Y. Liu, S. Wang, L. Lin, Y.S. Zhou, Y. Hu, Z.L. Wang, Theoretical investigation and structural optimization of single-electrode triboelectric nanogenerators, Advanced Functional Materials, 24 (2014) 3332-3340. https://doi.org/10.1002/adfm.201303799

[154] R.D.I.G. Dharmasena, K.D.G.I. Jayawardena, C.A. Mills, J.H.B. Deane, J.V. Anguita, R.A. Dorey, S.R.P. Silva, Triboelectric nanogenerators: Providing a fundamental framework, Energy & Environmental Science, 10 (2017) 1801-1811. https://doi.org/10.1039/C7EE01139C

[155] S. Niu, S. Wang, L. Lin, Y. Liu, Y.S. Zhou, Y. Hu, Z.L. Wang, Theoretical study of contact-mode triboelectric nanogenerators as an effective power source, Energy & Environmental Science, 6 (2013) 3576-3583. https://doi.org/10.1039/c3ee42571a

[156] S. Niu, Z.L. Wang, Theoretical systems of triboelectric nanogenerators, Nano Energy, 14 (2015) 161-192. https://doi.org/10.1016/j.nanoen.2014.11.034

[157] J. Shao, M. Willatzen, Y. Shi, Z.L. Wang, 3D mathematical model of contact-separation and single-electrode mode triboelectric nanogenerators, Nano Energy, 60 (2019) 630-640. https://doi.org/10.1016/j.nanoen.2019.03.072

[158] D. Galayko, E. Blokhina, P. Basset, F. Cottone, A. Dudka, E.O. Riordan, F. Orla, Tools for analytical and numerical analysis of electrostatic vibration energy harvesters: Application to a continuous mode conditioning circuit, Journal of Physics: Conference Series, 476 (2013) 012076. https://doi.org/10.1088/1742-6596/476/1/012076

[159] S. Ebnesajjad, *Fluoroplastics, volume 2: Melt processible fluoropolymers-the definitive user's guide and data book*, William Andrew, 2015.

[160] J. Wang, C. Wu, Y. Dai, Z. Zhao, A. Wang, T. Zhang, Z.L. Wang, Achieving ultrahigh triboelectric charge density for efficient energy harvesting, Nature Communications, 8 (2017) 88. https://doi.org/10.1038/s41467-017-00131-4

[161] X. Xia, J. Fu, Y. Zi, A universal standardized method for output capability assessment of nanogenerators, Nature Communications, 10 (2019) 4428. https://doi.org/10.1038/s41467-019-12465-2

[162] D. Liu, X. Yin, H. Guo, L. Zhou, X. Li, C. Zhang, J. Wang, Z.L. Wang, A constant current triboelectric nanogenerator arising from electrostatic breakdown, Science Advances, 5 (2019) eaav6437. https://doi.org/10.1126/sciadv.aav6437

[163] https://en.wikipedia.org/wiki/Parasitic_capacitance, 11th Nov., 2019

[164] K. Dai, X. Wang, S. Niu, F. Yi, Y. Yin, L. Chen, Y. Zhang, Z. You, Simulation and structure optimization of triboelectric nanogenerators considering the effects of parasitic capacitance, Nano Research, 10 (2017) 157-171. https://doi.org/10.1007/s12274-016-1275-7

[165] D.M. Fang, F.J. Zheng, B. Chen, Y. Wang, Y.G. Fang, P.F. Yang, X.L. Wen, C.R. Peng, S.H. Xia, Computation of capacitance and electrostatic forces for the electrostatically driving actuators considering fringe effects, Microsystem Technologies-Micro-And Nanosystems-Information Storage And Processing Systems, 21 (2015) 2089-2096. https://doi.org/10.1007/s00542-014-2322-5

[166] K. Shah, J. Singh, A. Zayegh, Modelling and analysis of fringing and metal thickness effects in mems parallel plate capacitors, Proceedings of SPIE (2006), 6035. https://doi.org/10.1117/12.638385

[167] Y. Feng, B.H. Shao, X.S. Tang, Y.H. Han, T.Z. Wu, Y. Suzuki, Improved capacitance model involving fringing effects for electret-based rotational energy harvesting devices, IEEE Transactions on Electron Devices, 65 (2018) 1597-1603. https://doi.org/10.1109/ted.2018.2803145

[168] C. Zhang, W. Tang, C. Han, F. Fan, Z.L. Wang, Theoretical comparison, equivalent transformation, and conjunction operations of electromagnetic induction generator and triboelectric nanogenerator for harvesting mechanical energy, Advanced Materials, 26 (2014) 3580-3591. https://doi.org/10.1002/adma.201400207

[169] H.Y. Li, L. Su, S.Y. Kuang, C.F. Pan, G. Zhu, Z.L. Wang, Significant enhancement of triboelectric charge density by fluorinated surface modification in nanoscale for converting mechanical energy, Advanced Functional Materials, 25 (2015) 5691-5697. https://doi.org/10.1002/adfm.201502318

[170] T. Sterken, P. Fiorini, G. Altena, C. Van Hoof, R. Puers, Ieee, Harvesting energy from vibrations by a micromachined electret generator, Proceedings of 14th International on Solid-State Sensors, Actuators and Microsystems Conference (2007), Lyon, France, 129-132. https://doi.org/10.1109/SENSOR.2007.4300088

[171] M. Suzuki, T. Takahashi, S. Aoyagi, Development of a high-performance fluorpolymer electret mixed with nano-particles and its application to vibration energy harvesting, Journal of Physics: Conference Series, 557 (2014) 012062. https://doi.org/10.1088/1742-6596/557/1/012062

[172] H.M. Xiao, G.J. Chen, X.M. Chen, Z. Chen, A flexible electret membrane with persistent electrostatic effect and resistance to harsh environment for energy harvesting, Scientific Reports, 7 (2017) 8443. https://doi.org/10.1038/s41598-017-07747-y

[173] G.J. Chen, Y.F. Li, H.M. Xiao, X. Zhu, A micro-oscillation-driven energy harvester based on a flexible bipolar electret membrane with high output power, Journal Of Materials Chemistry A, 5 (2017) 4150-4155. https://doi.org/10.1039/c6ta09964e

[174] X. Zhang, G.M. Sessler, Y. Xue, X. Ma, Audio and ultrasonic responses of laminated fluoroethylenepropylene and porous polytetrafluoroethylene films with different charge distributions, Journal of Physics D: Applied Physics, 49 (2016) 205502. https://doi.org/10.1088/0022-3727/49/20/205502

[175] H.T. Baytekin, A.Z. Patashinski, M. Branicki, B. Baytekin, S. Soh, B.A. Grzybowski, The mosaic of surface charge in contact electrification, Science, 333 (2011) 308-312. https://doi.org/10.1126/science.1201512

[176] X. Li, J. Tao, J. Zhu, C. Pan, A nanowire based triboelectric nanogenerator for harvesting water wave energy and its applications, APL Materials, 5 (2017) 074104. https://doi.org/10.1063/1.4977216

[177] R. Budakian, K. Weninger, R.A. Hiller, S.J. Putterman, Picosecond discharges and stick-slip friction at a moving meniscus of mercury on glass, Nature, 391 (1998) 266-268. https://doi.org/10.1038/34617

[178] X.Y. Wei, G. Zhu, Z.L. Wang, Surface-charge engineering for high-performance triboelectric nanogenerator based on identical electrification materials, Nano Energy, 10 (2014) 83-89. https://doi.org/10.1016/j.nanoen.2014.08.007

[179] M.R. Jung, F.D. Horgen, S.V. Orski, V. Rodriguez C, K.L. Beers, G.H. Balazs, T.T. Jones, T.M. Work, K.C. Brignac, S.-J. Royer, K.D. Hyrenbach, B.A. Jensen, J.M. Lynch, Validation of ATR FT-IR to identify polymers of plastic marine debris, including those ingested by marine organisms, Marine Pollution Bulletin, 127 (2018) 704-716. https://doi.org/10.1016/j.marpolbul.2017.12.061

[180] S. Kostromina, N. Kozlova, Y.A. Zubov, S. Chvalun, Y.A. Fedorovich, G. Ryvkin, X-ray study of structural parameters of some tetrafluoroethylene copolymers, Polymer Science USSR, 28 (1986) 992-998. https://doi.org/10.1016/0032-3950(86)90242-X

[181] C.G. Camara, J.V. Escobar, J.R. Hird, S.J. Putterman, Correlation between nanosecond x-ray flashes and stick-slip friction in peeling tape, Nature, 455 (2008) 1089-1092. https://doi.org/10.1038/nature07378

[182] C. Gay, L. Leibler, Theory of tackiness, Physical Review Letters, 82 (1999) 936-939. https://doi.org/10.1103/PhysRevLett.82.936

[183] K.-E. Byun, M.-H. Lee, Y. Cho, S.-G. Nam, H.-J. Shin, S. Park, Potential role of motion for enhancing maximum output energy of triboelectric nanogenerator, APL Materials, 5 (2017) 074107. https://doi.org/10.1063/1.4979955

[184] S. Niu, Y.S. Zhou, S. Wang, Y. Liu, L. Lin, Y. Bando, Z.L. Wang, Simulation method for optimizing the performance of an integrated triboelectric

nanogenerator energy harvesting system, Nano Energy, 8 (2014) 150-156. https://doi.org/10.1016/j.nanoen.2014.05.018

[185] Y. Lu, M. Capo-Chichi, Y. Leprince-Wang, P. Basset, A flexible electrostatic kinetic energy harvester based on electret films of electrospun nanofibers, Smart Materials and Structures, 27 (2018) 9. https://doi.org/10.1088/1361-665X/aa87da

[186] S. Niu, Y. Liu, Y.S. Zhou, S. Wang, L. Lin, Z.L. Wang, Optimization of triboelectric nanogenerator charging systems for efficient energy harvesting and storage, IEEE Transactions on Electron Devices, 62 (2015) 641-647. https://doi.org/10.1109/ted.2014.2377728

[187] S. Niu, X. Wang, F. Yi, Y.S. Zhou, Z.L. Wang, A universal self-charging system driven by random biomechanical energy for sustainable operation of mobile electronics, Nature Communications, 6 (2015) 8975. https://doi.org/10.1038/ncomms9975

[188] L. Jin, W. Deng, Y. Su, Z. Xu, H. Meng, B. Wang, H. Zhang, B. Zhang, L. Zhang, X. Xiao, M. Zhu, W. Yang, Self-powered wireless smart sensor based on maglev porous nanogenerator for train monitoring system, Nano Energy, 38 (2017) 185-192. https://doi.org/10.1016/j.nanoen.2017.05.018

[189] A. Ghaffarinejad, J. Yavand Hasani, D. Galayko, P. Basset, Superior performance of half-wave to full-wave rectifier as a power conditioning circuit for triboelectric nanogenerators: Application to contact-separation and sliding mode teng, Nano Energy, 66 (2019) 104137. https://doi.org/10.1016/j.nanoen.2019.104137

[190] A. Ghaffarinejad, J.Y. Hasani, R. Hinchet, Y. Lu, H. Zhang, A. Karami, D. Galayko, S.-W. Kim, P. Basset, A conditioning circuit with exponential enhancement of output energy for triboelectric nanogenerator, Nano Energy, 51 (2018) 173-184. https://doi.org/10.1016/j.nanoen.2018.06.034

[191] X. Cheng, L. Miao, Y. Song, Z. Su, H. Chen, X. Chen, J. Zhang, H. Zhang, High efficiency power management and charge boosting strategy for a triboelectric nanogenerator, Nano Energy, 38 (2017) 438-446. https://doi.org/10.1016/j.nanoen.2017.05.063

[192] F. Xi, Y. Pang, W. Li, T. Jiang, L. Zhang, T. Guo, G. Liu, C. Zhang, Z.L. Wang, Universal power management strategy for triboelectric nanogenerator, Nano Energy, 37 (2017) 168-176. https://doi.org/10.1016/j.nanoen.2017.05.027

[193] F. Chen, Y. Wu, Z. Ding, X. Xia, S. Li, H. Zheng, C. Diao, G. Yue, Y. Zi, A novel triboelectric nanogenerator based on electrospun polyvinylidene fluoride nanofibers for effective acoustic energy harvesting and self-powered multifunctional sensing, Nano Energy, 56 (2019) 241-251. https://doi.org/10.1016/j.nanoen.2018.11.041

[194] A. Ahmed, I. Hassan, T. Ibn-Mohammed, H. Mostafa, I.M. Reaney, L.S.C. Koh, J. Zu, Z.L. Wang, Environmental life cycle assessment and techno-economic analysis of triboelectric nanogenerators, Energy & Environmental Science, 10 (2017) 653-671. https://doi.org/10.1039/c7ee00158d

Synthèse en français

La récupération d'énergie ambiante représente une solution durable et complémentaire, par rapport aux batteries, en termes d'alimenter certains produits électroniques grand public, des réseaux de capteurs distribués sans fil, des dispositifs portables ou implantables, des systèmes "Internet of Things" avec beaucoup de nœuds, etc.. Les mouvements humains et les vibrations mécaniques sont des sources d'énergie les plus disponibles à cet effet. Les dispositifs collectant de l'énergie cinétique à petite échelle sont appelés récupérateurs d'énergie cinétique (RECs). Les RECs avec électrets (E-RECs) sont RECs électrostatiques qui utilisent des électrets (diélectriques avec charges quasi permanentes) comme source de tension de polarisation, et qui peuvent générer de l'électricité grâce à l'effet d'induction électrostatique lorsque la capacitance des E-RECs varie du fait des mouvements/vibrations. L'objectif de cette thèse est d'étudier les caractéristiques de sortie transitoires des E-RECs à la fois par des simulations théoriques et par des mesures expérimentales, et d'optimiser l'efficacité et la puissance de sortie des E-RECs par charge triboélectrique ainsi que d'autres méthodes adaptées à leurs caractéristiques de sortie, qui sont essentielles pour améliorer la performance des E-RECs.

Dans le premier chapitre de cette thèse, le contexte général, l'état-de-l 'art ainsi qu'une brève comparaison de trois types courants (électromagnétique, piézoélectrique, et électrostatique) de RECs sont présentés. Il a été conclu que certains facteurs tels que la dimension, la fréquence de travail, le circuit de charge doivent être pris en compte lors du choix du type de récupérateur d'énergie pour une application spécifique.

Le deuxième chapitre consiste en tout d'abord une introduction aux fondamentaux physiques et les méthodes de charge des électrets, et puis une introduction plus détaillée sur E-RECs, y compris le principe, la recherche l'histoire, les différents structures et modèles théoriques.

Dans le troisième chapitre, les caractéristiques de sortie à amplitude variable d'un E-REC en mode contact-séparation (CS) dans des cycles transitoires de travail sont examinées via les résultats de la simulation basés sur un modèle de circuit équivalent.

Ces caractéristiques de sortie à amplitude variable sont attribuées au fait du décalage du cycle de transfert de charge par rapport au cycle de mouvement d'excitation. Les influences de la condition initiale et de la résistance de charge sur la variation des pics de tension de sortie d'un tribo-électret REC (TE-REC) en mode CS réalisé avec un film électret en polytétrafluoroéthylène (PTFE) one été étudiées en détail et puis vérifiées à la fois par simulations et expériences.

Dans le quatrième chapitre, une méthode d'optimisation du temps de contact est utilisée pour améliorer la puissance de sortie et l'efficacité du TE-REC en mode CS avec une résistance de charge de 100 MΩ. L'énergie théorique maximale convertie par cycle de travail du TE-REC est ainsi analysée. Les influences de plusieurs facteurs défavorables qui généralement réduiraient la conversion d'énergie par cycle de travail du TE-REC sont étudiées. L'optimisation de l'intervalle maximale d'air et la méthode tribo-charge sont également utilisées pour améliorer la puissance moyenne sortie du TE- REC avec un film polymère de 4 cm × 4 cm, de ~ 150 μW à ~ 503 μW.

Dans le cinquième chapitre, une méthode innovante et facile a été développée pour charger le film polymère électret en éthylène propylène fluoré (FEP) par pelage de ruban adhésif, au lieu d'utiliser de source de haute tension électrique. La distribution du potentiel de la surface du film de FEP est fortement modifiée après plusieurs pelages. Par conséquence, la tension et le courant de sortie des TE-REC fabriqués avec le film FEP traité sont beaucoup améliorés. Pour un TE-REC flexible d'une surface de 64 cm^2 soufflé par du vent, une amélioration évidente d'environ 692% de la puissance de sortie, correspondant 2,5 μW à environ 19,8 μW, a été obtenue par cette méthode.

Enfin, dans le sixième chapitre, les conclusions générales de cette thèse, ainsi quelques remarques sur la simulation et la gestion de puissance des E-RECs, sont présentées. Certaines perspectives s'ouvrant sur les futurs travaux intéressants sont également introduites.